NOVA SCHOOL OF SCIENCE & TECHNOLOGY

DEPARTAMENT OF LIFE SCIECES

SUSANA MATILDE CARVALHO GOMES

BSc in Biochemistry

Antibody functionalized gold nanoparticles for mitochondria targeting and hyperthermia: a proof of concept in colorectal cancer

MASTER IN MOLECULAR GENETICS AND BIOMEDICINE

NOVA University Lisbon

September, 2022

DEPARTAMENT OF LIFE SCIENCE

Antibody functionalized gold nanoparticles for mitochondria targeting and hyperthermia: a proof of concept in colorectal cancer

SUSANA MATILDE CARVALHO GOMES

BSc in Biochemistry

Orientador: Pedro Miguel Ribeiro Viana Baptista
Full Professor, NOVA School of Science and Technology

Co-orientador: Maria Alexandra Núncio de Carvalho Ramos Fernandes
Assistant Professor with habilitation, NOVA School of Science and Technology

Jurí:

Presidente: Doutor Pedro Manuel Brôa Costa, Professor Auxiliar da Faculdade de Ciências e Tecnologia da Universidade NOVA de Lisboa

Orientador: Doutor Pedro Miguel Ribeiro Viana Baptista, Professor Catedrático da Faculdade de Ciências e Tecnologia da Universidade NOVA de Lisboa;

Arguente: Doutora Helena Luísa de Araújo Vieira, Professor Auxiliar da Faculdade de Ciências e Tecnologia da Universidade NOVA de Lisboa.

MASTER IN MOLECULAR GENETICS AND BIOMEDICINE

NOVA University Lisbon
September, 2022

Antibody functionalized gold nanoparticles for mitochondria targeting and hyperthermia: a proof of concept in colorectal cancer

ACKNOWLEDGMENTS

Em primeiro lugar, queria agradecer ao meu orientador, professor Pedro Baptista, por me ter despertado interesse pela área da nanomedicina logo no primeiro ano de mestrado, por me ter acolhido no seu laboratório para a realização deste projeto, por me ter orientado e por me ter mostrado o caminho da investigação, cheio de perguntas por resolver, desafios para ultrapassar, que envolvem crescer, aprender, ganhar espírito crítico... Cada dia no lab é um dia diferente, com novos desafios, novas lições! Igualmente agradeço à professora Alexandra Fernandes, por me ter acompanhado nesta jornada juntamente com o professor Pedro, por estar sempre disponível e mais uma vez, por ter estado presente nesta minha caminhada de início à investigação.

Não poderia também deixar de agradecer aos elementos do grupo do lab 315/319, por me ensinarem a "pôr a mão na massa", por mostrarem a rotina de laboratório, de investigação, os desafios diários que isso implica, pela disponibilidade em ajudar, em tirar dúvidas, em conciliar horários, por tudo! Vocês são o lab e sem vocês nada disto seria possível: Margarida, Daniela, Sandra, Catarina, Beatriz O, Rúben e André Luz, um grande obrigado com votos de sucesso para o vosso futuro na área da ciência!

André Meireis, *lab mate*, do primeiro ao último dia, juntos nesta jornada, unidos pelas nanopartículas de ouro. A nossa interajuda foi sem dúvida essencial, guardamos muitas recordações deste ano, aprendemos muito um com o outro e conseguimos sem dúvida ultrapassar grandes desafios ao longo dos nossos trabalhos, por trabalharmos em conjunto! Bea e Maria, as nanopartículas de ouro não nos uniam, mas o sentimento de amizade e gratidão sem dúvida que sim! Crescemos os quatro neste laboratório, muitas memórias, muitas conversas, muitos momentos fora do ambiente de trabalho que serão para sempre relembrados.

E porque esta tese não se fez só no laboratório, agradeço do fundo do coração às amizades que o mestrado me deu: Ao Miguel, que por coincidências as nossas vidas académicas e pessoais foram-se cruzando, o que permitiu que nos acompanhássemos mutuamente todos os dias deste ano, juntos nesta jornada da tese, do primeiro até ao último dia, ouviste falar de cancro, nanomedicina, eu de *Gobies*, alterações climáticas e ómicas; À Diana, por também estar presente todos os dias deste último ano, pelos encontros na cantina, pelas idas ao supermercado, também pelo acompanhamento mútuo das nossas teses, por tudo! À Marta, Joana F, Margarida, Raúl, Tomás, o grupinho do mestrado, que

mesmo longe uns dos outros, nunca a 25 de Abril se passava tão rápido para estarmos juntos! Obrigado por todos os momentos juntos e por terem dado ainda mais brilho a estes dois anos.

Por fim não poderia deixar de agradecer a quem me viu chegar aqui, a Coimbra, a Bioquímica, à Máfia. E claro aos meus pais e irmã por me apoiarem todos os dias, por me relembrarem de que sou capaz, de todo o percurso que fiz até aqui e por estarem sempre presentes.

Obrigado a todos!

Este trabalho é financiado por fundos nacionais através da FCT – Fundação para a Ciência e a Tecnologia, I.P., no âmbito do projeto 2022.04315.PTDC, projetos UIDP/04378/2020 e UIDB/04378/2020 da Unidade de Ciências Biomoleculares Aplicadas - UCIBIO e projeto LA/P/0140/2020 do Laboratório Associado Instituto para a Saúde e a Bioeconomia - i4HB.

“The scientist is not a person who gives the right answer
he's one who asks the right questions”
Claudé Lévi-Strauss

ABSTRACT

Colorectal cancer (CRC) has a high incidence and mortality rate, and traditional cancer therapies are not enough to treat and improve cancer patients' quality of life. Therefore, new therapeutic approaches are being studied, mainly focusing on improving the targeting specificity, not only to cancer cells but also to certain cellular compartments. Mitochondria are a promising target organelle for cancer therapies since they are involved in both cell health (being the cell's engine) and cell death (e.g., apoptosis). Nanomedicine provides effective multifunctional nanocarriers for a range of innovative cancer therapeutic strategies. Gold nanoparticles (AuNPs), due to their high surface area to volume ratio, have specific features that make them a great bet on cancer treatment. Among them, unique optical characteristics and the high capability in surface modifications. It has been shown that using a green laser that triggers an enhanced photothermal conversion by AuNPs this leads to cancer cells' death. Thus, this work aimed to assess whether targeting mitochondria of cancer cells followed by hyperthermia could improve cancer cell death by destabilizing or disrupting mitochondria. With this purpose, AuNPs were functionalized with a specific antibody against Hexokinase I (anti-Hexokinase I), a protein expressed in the mitochondrial outer membrane (MOM). This new nanoformulation (AuNP@PEG@Anti-Hexokinase I) was successfully synthetized and characterized prior to *in vitro* assays with a CRC cell line- HCT116. Then, internalization and mitochondrial targeting in HCT116 cells were assessed by complementary techniques, and all together seemed to indicate that AuNP@PEG@Anti-Hexokinase I had specificity for targeting mitochondria. Hyperthermia effect of AuNP@PEG@Anti-Hexokinase I did not have prominent outcomes, however, further studies are required. This study provides an initial step towards modulating mitochondria targeting using nanomedicines towards improved cancer therapies.

Keywords: Colorectal Cancer; Nanomedicine, Gold Nanoparticles; Mitochondria; Hyperthermia; Photothermal therapy.

RESUMO

O cancro colorretal (CCR) apresenta alta incidência e taxa de mortalidade e as terapias tradicionais atualmente aplicadas não são suficientes para tratar e melhorar a qualidade de vida dos doentes. Nos últimos anos, novas abordagens terapêuticas têm sido estudadas, principalmente com o foco em melhorar a seletividade da terapia, não apenas para células cancerígenas, mas também para determinados compartimentos celulares. As mitocôndrias são organelos promissores para o direcionamento de terapias anticancerígenas, uma vez que estão envolvidas tanto na sobrevivência como na morte celular. A nanomedicina permite desenvolver formulações à nano-escala, multifuncionais, para uma variedade de estratégias terapêuticas inovadoras anticancerígenas. As nanopartículas de ouro (AuNPs), devido à sua alta razão entre área superficial e volume, possuem características que as tornam promissoras no tratamento do cancro. Entre elas, propriedades óticas e superfícies facilmente modificadas. Estudos prévios demonstraram que irradiar AuNPs com um laser verde desencadeia uma conversão foto-térmica, que pode ser utilizada para promover a morte das células cancerígenas. Assim, este trabalho teve como objetivo avaliar se o direcionamento de AuNPs para as mitocôndrias seguido de hipertermia poderia induzir morte celular induzida por disfunção ou rompimento das mitocôndrias. Com este objetivo, as AuNPs foram funcionalizadas com um anticorpo contra a Hexoquinase I (anti-Hexoquinase I), uma proteína expressa na membrana externa mitocondrial (MOM). O nanoconjugado AuNP@PEG@Anti-Hexokinase I foi sintetizado e caracterizado com sucesso antes de serem realizados ensaios *in vitro* com uma linhagem de células de CRC (HCT116). A internalização e o direcionamento mitocondrial foram avaliados por técnicas complementares que em conjunto pareciam indicar que AuNP@PEG@Anti-Hexokinase I tinha especificidade para reconhecer e se ligar às mitocôndrias. O efeito de hipertermia das AuNP@PEG@Anti-Hexokinase I não teve resultados promissores, no entanto, requerem-se mais estudos. Este trabalho constitui um passo inicial para direcionar nanoformulações para mitocôndrias melhorando as terapias anticancerígenas.

Palavras chave: Cancro Coloretal; Nanomedicina; Nanopartículas de ouro; Mitocôndria; Hipertermia; Terapia Fototérmica.

CONTENTS

LIST OF FIGURES

LIST OF TABLES

ABBREVIATIONS, ACRONYMS AND CHEMICAL SYMBOLS

5-Flu- 5- Fluorouracil
ALA- 5-aminolevulinic
APC- Adenomatous polyposis coli
ATP- Adenosine triphosphate
AuNP@Citrate- Gold nanoparticles stabilized by a citrate layer
AuNP@PEG@Anti-Hexokinase I- Pegylated gold nanoparticles conjugated with Hexokinase I antibody
AuNP@PEG-COOH- Pegylated AuNPs
AuNPs- Gold nanoparticles
BRAF- V-Raf murine sarcoma viral oncogene homolog B
BSA- Bovine serum albumin
CDKs- Cyclin-dependent kinases
CO_2- Carbon dioxide
COX8- Cytochrome c oxidase subunit 8
CRC- Colorectal cancer
DAPI- 4′,6-diamidino-2-phenylindole
DCA- Dichloroacetate
DCC- deleted in colorectal cancer
DCC- Deleted in colorectal cancer gene
DLS- Dynamic light scattering
DMEM- Dulbecco's Modified Eagle Medium
DNA- Deoxyribonucleic acid
DOX- Doxorubicin
DQA- Dequalinium
DTNB- 5,5'-dithio-bis(2-nitrobenzoic)
EDC/NHS- 1-ethyl-3-(3-dimethylaminopropyl)carbodiimide/N-hydroxysuccinimide)
EGFR- Epidermal growth factor receptor**EPR**- Enhanced permeability and retention
FA- Folic acid
$FADH_2$- Flavin adenine dinucleotide
FDA- Food and drug administration
FITC- Fluorescein isothiocyanate
GFP- Green fluorescent protein
GLUT1- Glucose transporter 1
Gly- Glicine
H_2O_2- Hydrogen peroxide
HA- Hyaluronic acid
$HAuCl_4$- Chloroauric acid
HCTP- 10-Hydroxycampothecin
HNO_3- Nitric acid
$HO^{\bullet}$- Hydroxyl radical
HS-PEG(8)-COOH- Alpha-Thio-omega-(propionic acid) octa (ethylene glycol)
ICP-AES- Inductively coupled plasma atomic emission spectroscopy
IFA- Immunofluorescence assay
IGF- Insulin-like growth factor
KCl- Potassium Chloride
KRAS- Kirsten rat sarcoma viral oncogene homolog
KRAS- Kirsten rat sarcoma viral oncogene homolog

LSPR- Localized surface plasmon resonance
MAPK- Mitogen-activated protein kinase
MLH1- MutL homolog 1
MOM- Outer mitochondrial membrane
MOMP- Mitochondrial outer membrane pore
MSH2- MutS homolog 2
MTS- 3-(4,5-dimethylthiazol-2-yl)-5-(3-carboxymethoxyphenyl)-2-(4-sulfophenyl)-2H-tetrazolium
NaCl- Sodium Chloride
NADH- Nicotinamide adenine dinucleotide
NIR- Near-infrared light
NPs- Nanoparticles
O_2-Oxygen
$O_2^{\bullet-}$ - Radical superoxide
PBA- Phenylboronic acid
PCR- Polymerase Chain Reaction
PDI- Polydispersity index
PDT- Photodynamic therapy
PEG- Poly(ethylene) glycol
PET- Positron emission tomography
PLGA- Poly lactic-co-glycolic acid
PMS2- PMS1 homolog 2
PTT- Photothermal therapy
PTX- Paclitaxel
ppm- Part per million
RB- Phosphoprotein Retinoblastoma
RGD- Arginine-glycine-aspartate acid
ROS- Oxygen reactive species
RT- Room temperature
SDS- Sodium dodecyl sulfate
SMAC- Second mitochondria-derived activator of caspase
SPIONs- Superparamagnetic iron oxide nanoparticles
SSPs- Serrated Polyps
TCA- Tricarboxylic acid
TEM- Transmission electron microscopy
TNB- 2-nitro-5-thiobenzoic acid
TNFR- Tumour necrosis factor receptors
TPP- Triphenylphosphonium
TRITC- Tetramethylrhodamine
UV-Vis- Ultraviolet-Visible light
VEGFR-1- Endothelial growth factor receptor 1
VEGFR-3- Endothelial growth factor receptor 3
WHO- World Health Organization

1

INTRODUCTION

1.1 Cancer: An overview

1.1.1 Cancer incidence and mortality

Cancer is a multifactorial disease characterized by abnormal cell growth and loss of tissue cell organization [1]. According to the World Health Organization, in 2020, it was reported globally 19 million new cases of cancer and 10 million deaths related to this condition [2]. In the same year, in Portugal, there were 30 000 new cases, resulting in 9 000 deaths. The four most common cancers worldwide are

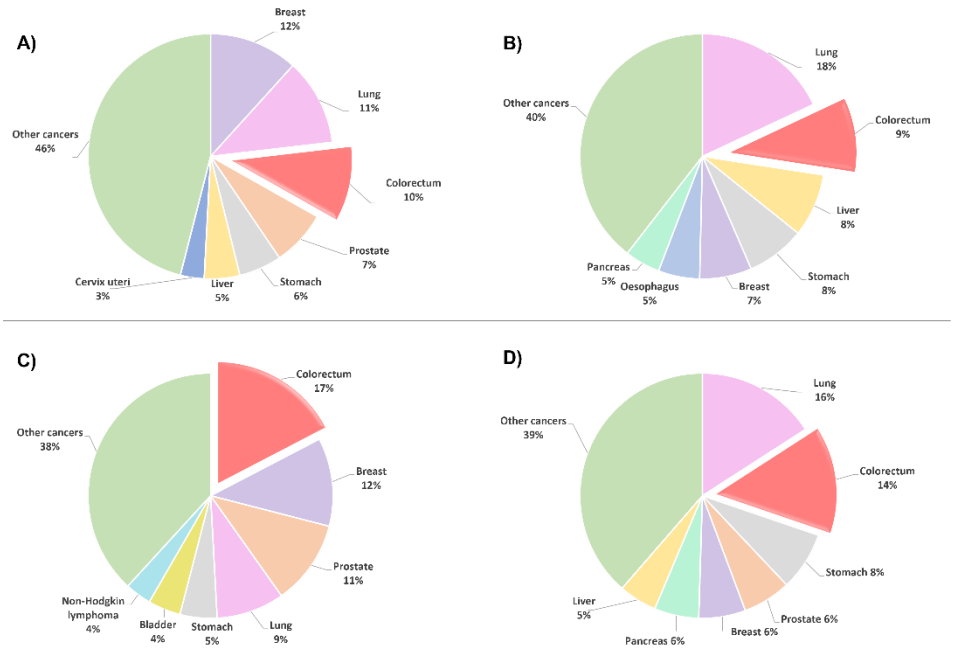

Figure 1.1 Distribution of estimated incidence and mortality by cancer in worldwide and Portugal in 2020, documented in the World Health Organization. A) New cases of cancer in worldwide for both sexes and all ages; B) Deaths by cancer in worldwide for both sexes and all ages; C) New cases of cancer in Portugal for both sexes and all ages; D) Deaths by cancer in Portugal for both sexes and all ages. Adapted from WHO Cancer Today, www.gco.iarc.fr.

breast, lung, colorectum and prostate cancer and the most deadly are lung, colorectum, liver and stomach cancer (**Figure 1.1**) [2]. Considering this incidence and mortality, improved screening for an early diagnosis and novel treatment strategies are needed [3].

1.1.2 Carcinogenesis: How does cancer begin?

Normal cells have a well-regulated cell cycle with four distinct phases, G_1, S, G_2 and mitosis (M) [4] (**Figure 1.2**) to assure an accurate controlled genetic replication and cell division, with several control points, checkpoints, along it (**Figure 1.2**) [4][5]. Cancer development, designated by carcinogenesis, is mainly associated with the successive accumulation of mutations in DNA that assist the cells in evading this tight control of the cell cycle regulation. Mutations in proto-oncogenes (becoming oncogenes) or in tumour suppressor genes can lead cells to acquire their own ability to produce mitogen signals (growth factors, hormones and cytokines), which induces and sustain continuous cell growth and division. Moreover, mutations in these genes can lead to changes in mitogen receptors, increasing their susceptibility to lower concentrations of mitogen signals or making these receptors continuously activated, even in the absence of signals. When cells are exposed to stress stimulus or damage, tumour suppressor proteins are activated, interrupting the cell cycle, thus giving time for cells to repair damages

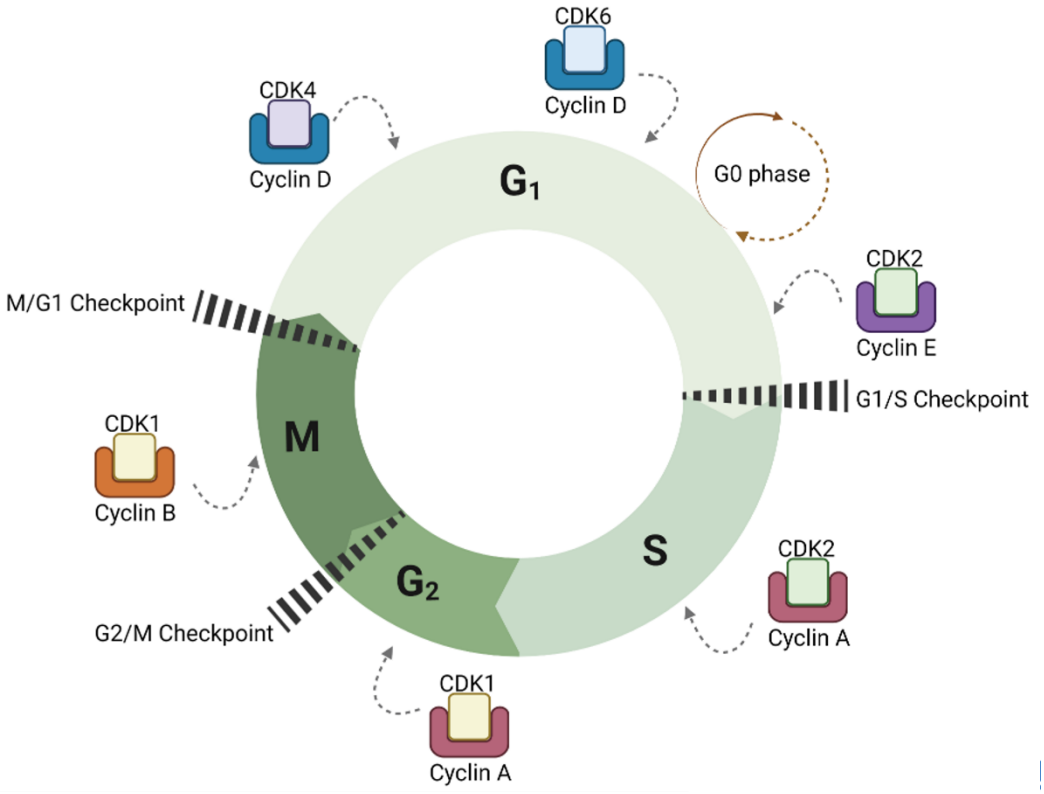

Figure 1.2 Cell cycle and the three main checkpoints. Cells have four distinct phases, G_1, S, G_2 and mitosis (M) by which they must undergo until their division. Cells may also be in a resting phase (G0), characterized by a non-dividing but metabolically active phase. To ensure that cells are able to divide, there are three main checkpoints throughout the cell cycle: G2/M checkpoint; M/G1 checkpoint; G1/S checkpoint. Cyclin dependent kinases (CDKs) bind to specific cyclin protein and give rise to an active complex responsible for activating specific proteins that consequently allow cell cycle progression [5]. Created in Biorender.com and adapted from [134].

or initiate a controller response against the stress [4]. If the damage cannot be repaired, regulated cell death pathways are activated to prevent the proliferation and accumulation of damaged cells. Activating regulated cell death pathways by healthy cells is a powerful way to avoid cancer development. Consequently, cancer cells acquire the ability to bypass apoptotic signals and thus avoid apoptosis (programmed cell death) (see section 1.1.3) [6].

During cancer progression, there is the invasion of the surrounding tissues and blood vessels, which can lead to the onset of metastases – a malignant tumour [7].

1.1.3 Programmed cell death: What goes wrong?

As stated above, in healthy cells, when injury prompted by cellular damages cannot be repaired, programmed cell death (apoptosis) is activated. There are two main pathways to trigger apoptosis: extrinsic and intrinsic/mitochondrial pathways (**Figure 1.3**) [6][8]. Activation of apoptotic pathways leads to activation of cysteine proteases, named by Caspases, the effectors of cell death. The extrinsic pathway is activated due to the recognition of some molecules by specific receptors at the cell membrane, designated by death receptors [9]. Death receptors are part of a superfamily designed by tumour necrosis factor receptors (TNFR), which include TNFR1, Fas and TRAIL receptors. Recognition of respective ligands by these types of receptors leads to the recruitment and activation of caspase-8, which consequently cleaves and activates downstream effectors such as caspase-3 and -7. Furthermore, caspase-8 activation can also promote the permeabilization of the outer mitochondrial membrane (MOM) by cleaving the BID protein. After the BID cleavage, it is translocated to mitochondria and induces Cytochrome C and second mitochondria-derived activator of caspase (SMAC) release [8][9]. Cytochrome C release is an indicator of mitochondrial pathway activation. Such release leads to the activation of caspase-3 via the apoptosome, a complex established between Cytochrome C, Caspase-9 and Apaf-1 [9]. The mitochondrial pathway is regulated by proteins that belong to the BCL-2 family [9][10]. There are three distinct groups of proteins within the BCL-2 family, based on their functions: Anti-apoptotic proteins, such as BCL-2, which prevent the trigger of apoptosis; Pro-apoptotic pore-formers, such as BAX and BAK, which forms the mitochondrial outer membrane pore (MOMP); Pro-apoptotic BH3-only proteins, such as BAD and BID protein, which are apoptotic activators (improving the affinity of membranes for pore-formers proteins), or sensitizers (sequestering and inhibiting the anti-apoptotic proteins), respectively. The formation of MOMPs triggers apoptosis through the oligomerization between BAX and BAK proteins. Once MOMP is formed, Cytochrome C is released from the mitochondrial intermembrane space triggering the caspase cascade and leading to cell death [10]. Loss of control in apoptosis pathways is the first hallmark of cancer development and is widely common in all cancers [6]. The ability of cancer cells to avoid apoptosis under stress signals is due to the loss of recognition of extrinsic apoptotic signals or due to resetting of the balance between intracellular pro- and anti-apoptotic molecules, with an increase in the ratio of anti- to pro-apoptotic BCL 2 proteins or an increase in the expression of inhibitor apoptosis proteins. Decreasing the expression of death receptors is also an adaptative way for cells to avoid apoptosis. This phenomenon allows cancer cells to survive with DNA damage [6][9]. Examples of molecular changes that allow cells to avoid programmed cell death are mutations in Caspase-8 genes, which have been described in colorectal

and head and neck cancer, or changes in the expression of the survival factor insulin-like growth factor (IGF) [9][11].

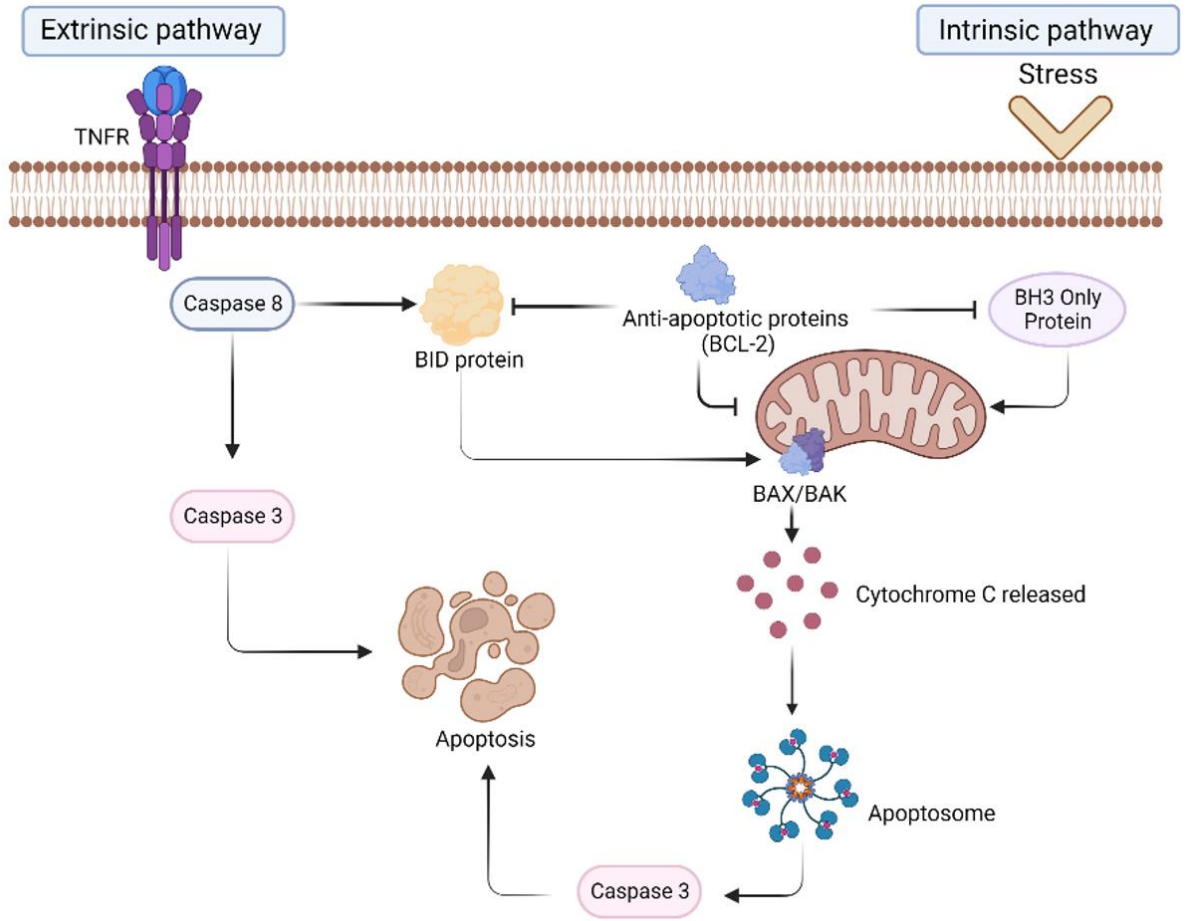

Figure 1.3 Intrinsic and extrinsic apoptosis pathways. The extrinsic pathway is triggered by the recognition of some molecules by death receptors, TNFRs. This triggers the recruitment and activation of Caspase 8 that consequently activates downstream effectors, such as Caspase-3. Caspase 8 also 4links this pathway with the intrinsic pathway, through the cleavage and activation of the BID protein, which are consequently translocated to the mitochondria and allow the release of Cytochrome C. The intrinsic pathway, also known as the mitochondrial pathway, is triggered by a stress factor. This leads to the activation of BH3 only proteins (pro-apoptotic proteins) which induces the oligomerization of BAX and BAK, giving rise to MOMP. Consequently, Cytochrome C are released and apoptosome, a complex established between Cytochrome C, Caspase-9 and Apaf-1 is formed. Apoptosome activates Caspase-3 and apoptosis is triggered. Created in Biorender.com and adapted from [135].

1.1.4 Role of mitochondria in cancer development and maintenance

Mitochondria, cell organelle with a two-layer membrane and with their own genome, have a dual role in cells: (i) they are the cell engine, as they retain the main source of catabolic and anabolic reactions responsible for energy production and cell maintenance; (ii) they are also a regulator of cell death, as they are involved in the intrinsic and also in the extrinsic (via BID) apoptotic pathways, as previously described (section 1.1.3) [12]. Furthermore, mitochondria are also associated with calcium and oxygen reactive species (ROS) homeostasis [13][14].

Carbon flues are used by cells to obtain energy through catabolic reactions and to ensure cell viability through biosynthetic pathways. Glucose, the main source of carbon used by cells, is metabolized into pyruvate by a cytoplasmatic pathway, the glycolysis [15]. Along this important pathway, nicotinamide adenine dinucleotide (NADH), flavin adenine dinucleotide ($FADH_2$) and pyruvate are intermediate molecules that retain the energy potential used by mitochondria to further energy production. 90% of total cell energy is produced by mitochondria [16]. Containing two membranes (an outer and an inner membrane), the space between them is designated the intermembrane space. The outer membrane has pores that allow the interchanging of large and small molecules. The inner membrane is highly selective and permeable, permeating only water, carbon dioxide (CO_2) and oxygen (O_2). The inner membrane is loaded with five protein complexes (I-V), forming the mitochondrial respiratory chain [17]. The space bounded by the inner membrane is named the mitochondrial matrix, where Krebs / tricarboxylic acid (TCA) cycle occurs. Pyruvate obtained by glycolysis is metabolized to CO_2 in the TCA, and energy potential stored in NADH and $FADH_2$ is converted to adenosine triphosphate (ATP) by oxidative phosphorylation. Through an electrochemical gradient, electrons move along the complexes of the electron transport chain until they reach the final acceptor, the oxygen. The movement of electrons is coupled with the pumping of protons from the mitochondrial matrix to intermembrane space through the electronic chain complexes. The accumulation of protons in the intermembrane space activates the last complex of the chain, the ATP Synthase protein complex. Electric potential is restored through the flow of protons back into the mitochondria matrix via ATP Synthase, coupling with ATP synthesis [18][19].

In the absence of oxygen, glucose can be fermented: Pyruvate is metabolized into organic acids (i.e. lactate) or alcohol [15]. In addition to energy production, essential biomolecules to cell growth and proliferation (nucleotides, lipids and amino acids) are also synthesised by metabolites obtained by the TCA cycle [20]. For example, fatty acids synthesis uses citrate, the second product of TCA cycle and amino acid synthesis requires glutamate and aspartate obtained by TCA intermediaries: α-ketoglutarate and oxaloacetate, respectively [21].

Cancer cells undergo metabolic changes in order to sustain their proliferation and maintenance [20][22]. Otto Warburg observed that cancer cells have a higher uptake of glucose and high production of lactate, even in the presence of high levels of oxygen, due to the fermentation of glucose by aerobic glycolysis. This is known as the Warburg effect [23][24]. Indeed mitochondrial oxidation of glucose is more rentable in terms of ATP production than glycolysis (glycolysis produces two ATPs per glucose, whereas complete oxidation produces more than 36 ATPs) [15], however, the lactate production by aerobic glycolysis is 10-100 times faster [23]. Despite the Warburg effect suggesting that cancer cells choose aerobic glycolysis instead of oxidative phosphorylation and that this is due to mitochondrial dysfunction, it is now known that the rate of oxidative phosphorylation is similar between healthy and cancerous cells. In other words, when cancer cells have high rates of oxygen available and no mutation in enzymes associated with mitochondria metabolism, proliferation is supported mainly by oxidative phosphorylation [20][25]. Furthermore, it is known that metabolization of fuels like pyruvate, fatty acids, acetate, and hydroxybutyrate occurs at a higher rate in cancer cells than in normal cells [22]. In hypoxic

environments, such as the tumour core, where the rate of available oxygen is low, cancer cells obtain energy by anaerobic glycolysis [26]. Depending on the environmental conditions of the tumour, it can reprogram its metabolic pathways [20].

Metabolic reprogramming in cancer cells is also controlled by oncogenes and tumour suppressor genes. For example, hypoxia-inducible factor 1α (HIF-1α), a transcription factor which promotes glycolysis and decreases oxidative phosphorylation, is expressed in an oxygen concentration manner: a high level of oxygen decreases HIF-1α. HIF-1α increases Glucose transporter 1 (GLUT1) and hexokinase 2 (HK2) expression, culminating in an over-uptake of glucose and glycolytic activity. In contrast with normal cells, cancer cells have a high HIF-1α level even when oxygen is available. This is a consequence of AKT and mTOR activation induced by oncogenes expression [25].

ROS are molecules resulting from oxygen with extra electrons able to oxidize other molecules. 1% of their production is a consequence of oxidative phosphorylation in mitochondria [27]. Radical superoxide ($O_2^{\bullet -}$), hydrogen peroxide (H_2O_2) and hydroxyl radical ($HO^{\bullet}$) are the main ROS produced by cells, and each one has a different effect on cells [28][29]. Although ROS are mainly related to cell toxicity, in the last decades many outcomes have revealed their relevance in cell signalling.[20] Proteins associated with cell growth and metabolism reprogramming can be positively activated by ROS-induced oxidation [20][28]. It is known that cancer cells have a high rate of ROS production and it is one of the consequences of changes in the expression level of oncogenes and tumour suppressor genes, which increase the proliferative rate of cells and consequently, the activity of metabolic pathways [28]. However, cancer cells need to maintain balanced levels of ROS, to avoid toxic effects and, consequently, activation of apoptotic pathways or damage to proteins, lipids, and DNA. This balance is achieved by cancer cells through the overexpression of ROS scavenging enzymes [30]. As a vicious

cycle, tumorigenesis increases the metabolic activity of cancer cells and consequently ROS production, but in the same way, high ROS levels activate cell growth and maintenance pathways (**Figure 1.4**) [20].

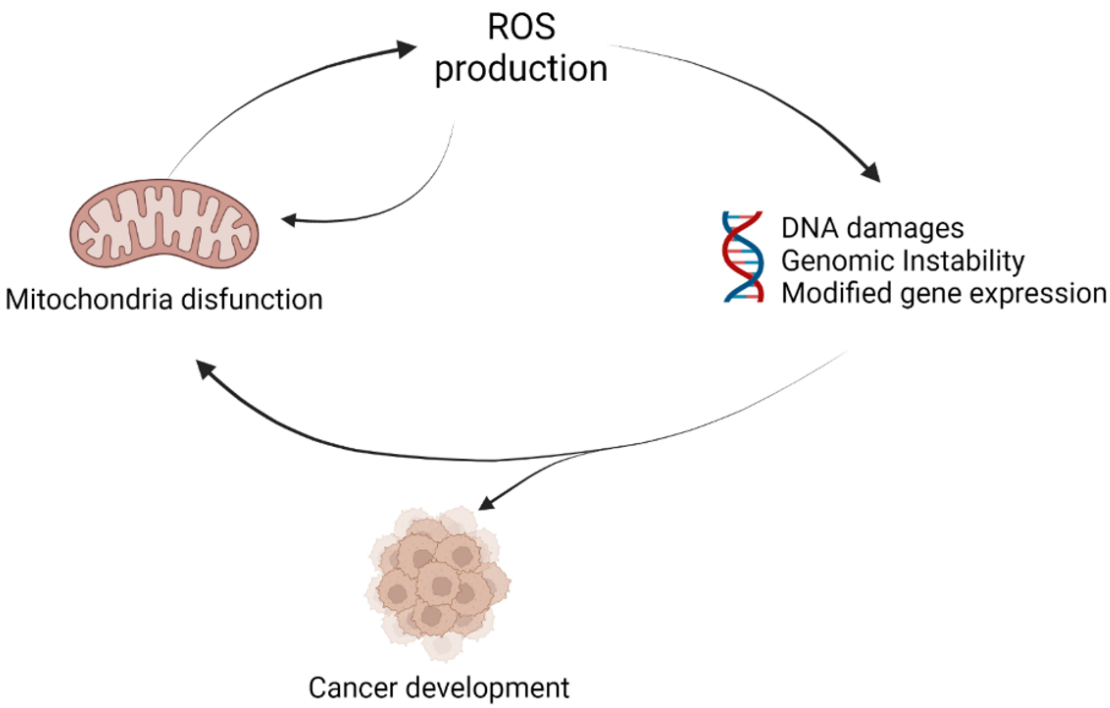

Figure 1.4 Role of mitochondria and ROS in cancer development and maintenance. Production of reactive oxygen species can be a consequence of dysfunctional mitochondria which, in turn, can be caused by DNA damages genomic instability and changes at the genetic expression induced by increased levels of ROS. Cancer is known to be a consequence of this. Created in Biorender.com and adapted from [27].

Since mitochondria play a significant role in cell maintenance, survival and proliferation, they are promising targets for developing new cancer therapies. Some therapeutical approaches can be highlighted, such as i) targeting mitochondrial permeability transition pore complex; ii) disrupting metabolic pathways; iii) triggering apoptotic pathways; and iv) triggering ROS production. Indeed, targeting drugs/therapeutic formulations to mitochondria may be possible using lipophilic compounds e.g,. organic phosphine/sulphur salts (Triphenylphosphonium-TPP), transition-metal complexes, and peptides/antibodies, which are able to penetrate and accumulate in mitochondria [12]. Some of these approaches will be later discussed in section 1.2.

1.1.5 Colorectal Cancer

In 2020, colorectal cancer (CRC) was the third most common cancer and the second cause of cancer death in the world – see **Figure 1.1** [2]. The incidence of CRC is higher in men than in women. Age is one of the main factors impacting incidence, with an average age of 70 years old for diagnosis. Europe, Oceania and North America are the regions with the highest incidence. Food habits, obesity, physical inactivity, tobacco and alcohol consumption are known factors that increase the risk of CRC

development [32][33]. The risk of developing CRC can also be related to the familiar history of colorectal polyps or cancer or co-related with Lynch syndrome or type 2 diabetes [31][32][33].

Colorectal cancer is known as a slow disease with a gradual development as the symptoms are minimal until the tumour reaches a considerable size. At this point, the tumour may block the gut traffic, and primary symptoms appear [32]. Some behaviours can be adopted to minimize the risk of cancer development, such as the inclusion of physical activity in the daily routine, the use of hormone replacement therapy and the inclusion of endoscopy exams as a preventive exam, which can screen and remove precancerous lesions [31].

The outset of CRC development is usually associated with the arising of localized projections of abnormal cells into the intestinal lumen, designated by Polyps. These projections can have two distinct shapes: flat or pedunculated. Although most polyps are benign (non-cancerous), they may be the precursor of colorectal cancer development. When polyps achieve a considerable size, the fast division of the polyp's cells predisposes them to genetic mutations and epigenetic changes that accumulate at each division. Some of these mutations make polyps cells able to invade the bowel wall and eventually allow them to spread to lymph nodes, leading to metastasis. Most mutations associated with CRC are sporadic, however, there are some inherited mutations (≈5%), such as, mutations related to the Lynch Syndrome / *MutL homolog 1* (*MLH1)*, *MutS homolog 2 (MSH2)*, *PMS1 homolog 2* (*PMS2)* and *Adenomatous polyposis coli* (*APC*) genes (**Figure 1.5**) [32].

Among the different types of polyps, Adenomatous (adenoma) and Serrated Polyps (SSPs) are the most likely to become cancerous [32]. Although only 10% of adenoma becomes cancer, about 70% of CRC have adenoma origins, and 35% develop from SSPs. Adenomas are physically characterized by having a mushroom-shape. Their development is associated with the accumulation of mutations over cell division, transforming normal cells into an early adenoma, late adenoma and then cancer [32][34]. This phenotypical transition is caused by genetic mutations in *APC*, *Kirsten rat sarcoma viral oncogene homolog* (*KRAS*), *deleted in colorectal cancer* (*DCC*) and *P53* genes, as stipulated by the Vogelstein model [32][34][35][36]. In contrast, SSPs have a flat shape where normal cells turn into a hyperplastic polyp, sessile serrated adenoma and then cancer [32][34]. This type of polyps is mainly associated with mutations at the *V-Raf murine sarcoma viral oncogene homolog B* (*BRAF)* and *KRAS*, which encodes to kinases of the mitogen-activated protein kinase (MAPK) cascade [36][37]. Mutations at these genes promote changes in growth signalling and loss of apoptosis regulation due to the constitutive activation of the MAPK cascade [37]. Moreover, aberrant hypermethylation of gene promoter regions is also a feature of SSPs [32]. Chronic inflammation is another pathway associated with CRC development [34]. Due to the vast pathways that can be related to the development of colorectal cancer, identifying them in a particular patient is extremely important to adapt the therapy and improve the efficiency of the treatment [31].

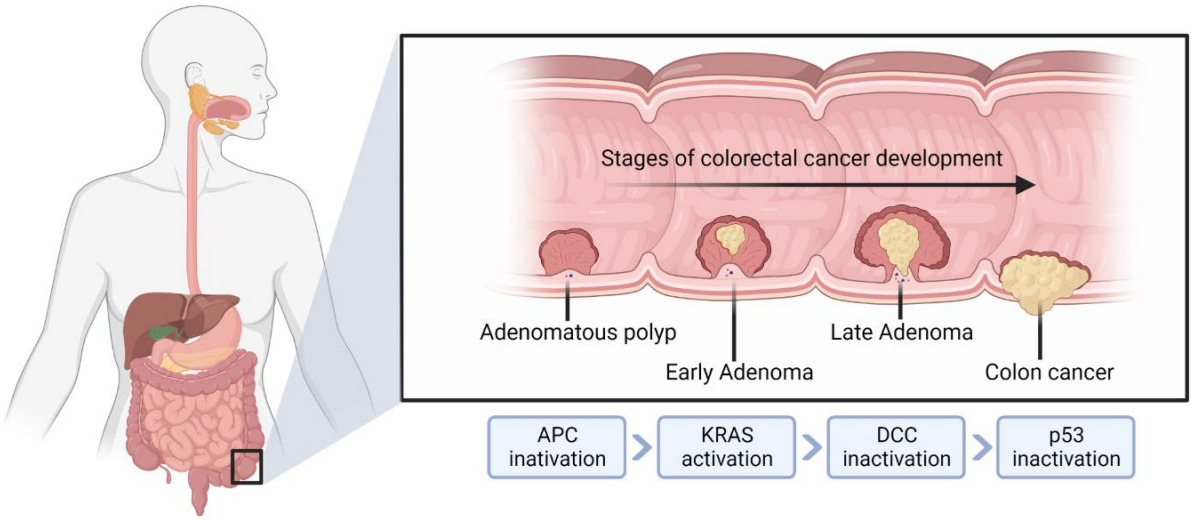

Figure 1.5 Schematic representation of colorectal cancer stages and associated mutations. The emergence of localized projections in the colon is the first hallmark of colorectal cancer development. The five main mutations associated with each stage are in *APC-KRAS-DCC-P53* genes. Created in Biorender.com and adapted from [136].

1.2 Cancer Therapies – a brief overview

1.2.1 Traditional cancer therapies

Traditional cancer treatments include surgery, chemotherapy and radiotherapy [1][38]. However, new emerging cancer therapies with high clinical potential have emerged, such as phototherapy [39].

Surgery, (i.e., the removal of the tumour mass), is the first therapeutic approach chosen in non-metastatic cancers. When performed during the early development of cancer, a better prognosis for cancer patients is expected. However, its effectiveness may be lower due to the precision of removing all cancer cells, associated with the method used, the cancer localization and stage. Unfortunately, cancer reoccurrence is very common and, therefore, conjugating surgery with radiotherapy or chemotherapy, as adjuvant or neoadjuvant therapies, is a recurrent approach [40].

Radiotherapy uses ionizing radiation to induce cell damage and, consequently, cell death. The ionizing radiation can target and damage the DNA directly or indirectly, through the production of free radicals and charged particles, by the ionization of water molecules [38][41][42]. Focusing the radiation on a specific tissue lessens the damage to healthy cells, however, healthy tissues can also be affected. Furthermore, the susceptibility of cells to radiotherapy depends on their ability to repair the damage and to induce the grow new cells to replace the death cells. Therefore, is critical to ensure that normal tissue dose tolerance is not exceeded. Hence, radiotherapy is mainly used in treating primary tumours due to focusing on a small body region [41][42].

Chemotherapy uses chemotherapeutic agents that affect the normal cell cycle of actively proliferating cells [41]. As cancer cells have a high division rate, chemotherapeutic agents have more specificity to these cells, however, healthy cells with a rapidly dividing rate, like immune cells or bone

marrow cells, can also be targeted by these agents [38]. Nonetheless, as a systemic therapy, it can also reach metastases [41].

In CRC, surgery is the standard therapeutic. However, in advanced stages of CRC, due to the metastatic profile, the use of chemotherapy and radiotherapy is essential. Oxaliplatin, 5-Fluorouracil (5-Flu) and Irinotecan, are some chemotherapy drugs currently used in CRC [31][40].

1.2.2 Phototherapy

Phototherapy uses a light source to induce cell death through the conversion of light (photons) into heat energy [43][44]. Light can be applied directly under the tumour tissue, however, this has some disadvantages, such as low specification and the need for a high-power density and long exposure time, which can cause damage to normal tissues [38][44]. Increasing the selectivity and specification of phototherapy and minimizing collateral damage can be achieved by conjugating light with an exogenous photothermal or photosensitizing agent [39][44][45]. Therapies that include these agents can be differentiated into photothermal therapy (PTT) and photodynamic therapy (PDT), respectively [44].

In PTT, an exogenous photothermal agent, when exposed to a light source, absorbs energy from photons and converts it into heat by changes in electronic states (**Figure 1.6**) [44][46]. This electronic energy excitation undergoes vibrational relaxation, which increases kinetic energy and enhances the healing of cells and tissues in a local area of the body (hyperthermia). Increasing temperature around cells and tissues induces some environmental changes [44]. Increasing temperature above 30°C causes changes in lipidic layers, and above 80°C changes in DNA and RNA structures. However, hyperthermia-induced cell death occurs mainly due to protein denaturation. At 41°C cells undergo changes in gene expression, i.e., increasing the expression of heat-shock proteins. When the temperature increases to 42°C irreversible tissue damage occurs, and between 42-46°C cell necrosis is visible [44]. At 46-52°C cell death occurs rapidly, by ischemia and microvascular thrombosis. In PTT, a temperature of 60°C is reached, which leads to DNA and RNA denaturation and immediate cell death by protein denaturation and plasma membrane destruction [1][44].

In PDT, a photosensitizing agent excited by light generates ROS through interaction with biomolecules or directly with molecular oxygen (**Figure 1.6**) [44][47]. With increased ROS levels in the irradiated tumour region, cytotoxic effects can kill cancer cells [44]. Photofrin (Porfimer sodium - excitation wavelength at 630 nm) was the first photosensitizer agent approved for PDT therapy and is used against many cancers such as lung, cervical and bladder cancer. The second generation of PDT agents has been developed, and they are characterized by a higher level of purity, higher wavelength absorption, photosensitivity and tissue specification [48]. Among the second-generation photosensitizer drugs Levulan (Aminolevulinic acid - excitation wavelength at 635 nm), Metvix (Methyl aminolevulinate - excitation wavelength at 570-670 nm), Redapordin (excitation wavelength at 749 nm) are some of those approved by the FDA [47]. Although these approaches are not yet used as CRC's therapies, some studies are being carried out: 5-aminolevulinic (ALA) and Sinoporphytin sodium are examples of photosensitizing agents tested on multiple cell lines of CRC (e.g., SW470 [49][50], SW620 [49][50], Caco-2 [51], and HCT116 [52]) and also in mice inoculated with HT-29 cells [53], where high apoptosis and tumour inhibition rate were observed.

Most PTT and PDT agents absorb light in the visible range, however, the low ability of light to penetrate the interior of the body (<1cm) can be an obstacle to the choice of these therapies against deep tumours [44][54]. Several light sources are used: ultraviolet light (330-400 nm); red-light (600-700 nm), and near-infrared (NIR) light (700-1000 nm) but longer wavelength light (NIR and red light) penetrates deep into the body tissues [43][48]. Using PTT and PDT as approved oncological therapies still have some disadvantages, including the low accuracy of the systemic distribution of the photothermal/photodynamic agent. In this way, research efforts have been made to formulate the third generation of photothermal/photodynamic agents in order to improve their enrichment at the tumour site and, consequently, to induce controlled heating of cancer cells with minimal normal cells damages [46]. The administration of the photothermal agent directly into the tumour tissue by intratumoral injection is one of the approaches, but it has some disadvantages such as i) it does not reach metastasis; ii) the tumour tissue cannot be deep. Another approach is to encapsulate photosensitizers in carries (nanodelivery systems) and/or to conjugate tumour-specific ligands, such as antibodies, to specifically target the tumour site through intravenous administration [46][48]. Photosensitizers can be targeted to a specific tissue, body region or even specific cell organelles (i.e. lysosomes and mitochondria), which increases the specificity of the therapy and reduce off-target toxicity in surrounding tissues [44][39]. For example, due to the role of mitochondria in cell survival (as described in section 1.1.4) and how cancer mitochondria are more susceptible to ROS and temperature rise [55], targeting these organelles is achieved by conjugating photosensitizers with TPP or Dichloroacetate (DCA) [47].

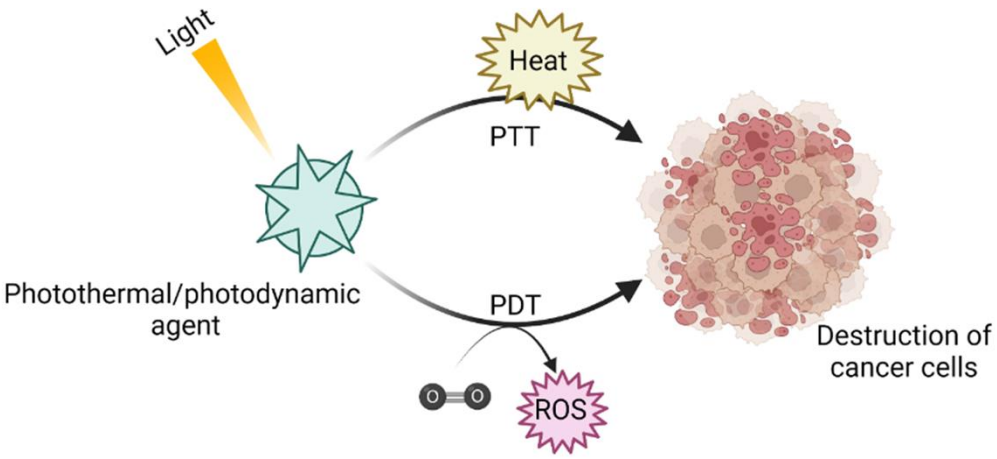

Figure 1.6 Photothermal (PTT) and photodynamic (PDT) cancer therapy. A photothermal agent, when exposed to a light source and when located in the tumour area, could induce cell death by increasing the local temperature around cancer cells. On the other hand, photodynamic agents could induce cancer cell death by generating ROS. Both phototherapies have the disadvantage of being dependent on the ability of light to penetrate body tissues. Created in Biorender.com and adapted from [44].

Despite the existence and application of all these cancer therapies, the low differentiation between cancer and non-cancer cells forces the formulation of new therapeutic approaches to specifically target cancer cells, improve the therapeutic effect, and reduce the damage to normal cells. The use of nanotechnology is one of the most promising approaches, as will be discussed below (section 1.3) [56].

1.3 Nanomedicine

Nanotechnology was uttered for the first time in 1974 by Taniguchi [57]. It is dedicated to the study of nanoscale materials (10^{-9} m), as well as their properties and applications [57] [38][58]. Due to the small size of nanoscale materials, some properties, such as optical, electrical conductivity, chemical reactivity, physical strength, and magnetism, are different from those in the bulk material. The broad types of nanomaterials and their features allow the arising of several nanodevices with a wide range of applications such as medicine, electronics, energy, environment, transportation, and even space exploration [57].

Nanomedicine is one of the fields of nanotechnology that combines nanomaterials, medicine and pharmacology to overcome medical issues [59]. Due to the unique physical and chemical properties of nanoscale materials, they have a high potential to solve medical challenges associated with disease diagnosis, treatment, and imaging. Moreover, nanomaterials and biomolecules are both in the same order of magnitude in size (nanometer), facilitating their interaction and making nanomaterials a good approach to targeting biological pathways and processes [60]. In the last years, the introduction of nanotechnology has achieved many outcomes in cancer therapy, regenerative medicine, drug delivery, neurodegenerative disorders treatment and vaccine formulation [57].

1.3.1 Cancer nanomedicines

In oncology, nanomaterials (carbon nanotubes, dendrimers, nanocrystals, nanoparticles, nanoshells and nanowires) can be used for bioimaging, diagnosis and therapy.

After their administration and when in the bloodstream, nanomaterials can reach a target tissue in two ways: passive or active targeting (**Figure 1.7**). Cancerous tissue has a different vasculature morphology from normal tissues due to the high and fast rate of angiogenesis (growth of new blood vessels from existing ones). In normal tissue, endothelial cells are well organized and packed, whereas, in cancerous tissue, vasculature has leaky pores. These differences lead to a phenomenon known as the Enhanced permeability and retention (EPR) effect: nanomaterials, due to their sizes, accumulate preferentially in cancerous tissues as a consequence of the existence of gaps between adjacent

endothelial cells [44][61]. The EPR effect also depends on features associated with the tumour in terms of size, anatomical localization and type of cancer [58].

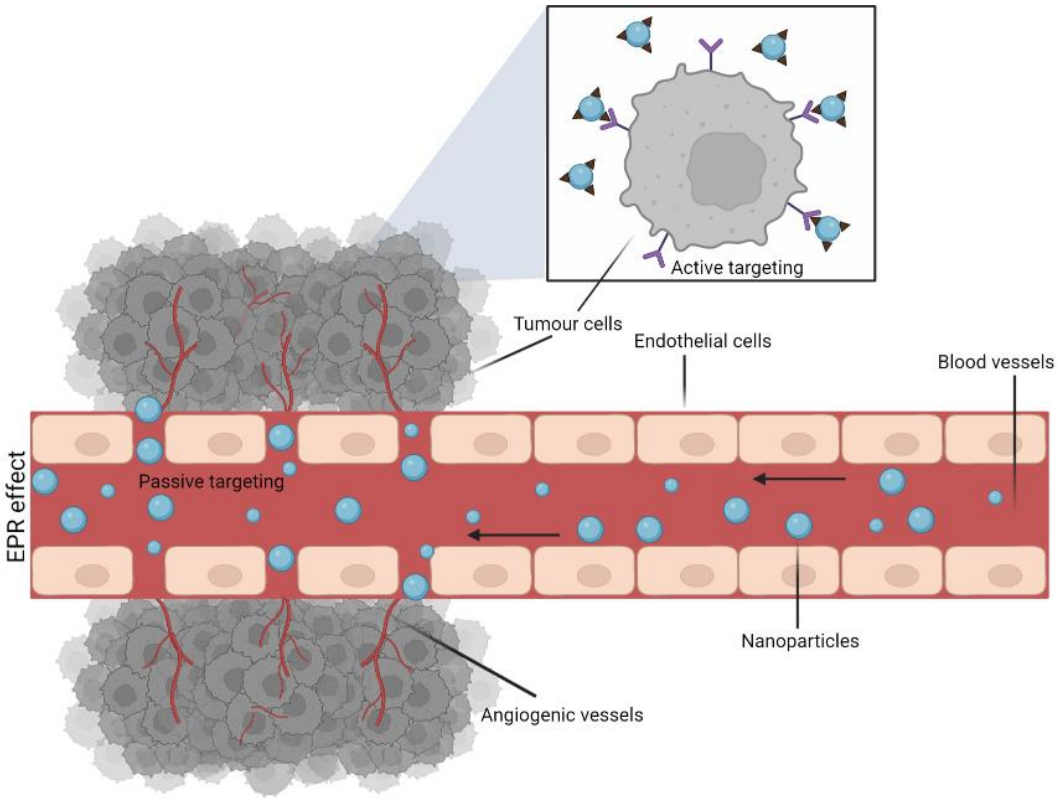

Figure 1.7 Passive and active targeting of nanoparticles to tumour cells. In the tumour area, the endothelial tissue has disorganized cells and consequently, leaky pores between them. Additionally, due to the high proliferative rate of cancer cells and the high necessity of oxygen and nutrients, angiogenesis occurs at a higher speed. Altogether, these allow nanoparticles to preferentially accumulate at the tumour tissue by an effect named the Enhanced permeability and retention effect. To improve the specific targeting of nanoparticles, their surfaces can be modulated, for example by attaching specific antibodies, which bind and recognize the predicted cells. This is named active targeting. Created in Biorender.com and adapted from [62].

Active targeting of nanomaterials is achieved when they interact, retain, and recognize a specific tissue or cell (**Figure 1.7**). This is possible by modifying the surface of nanomaterials with molecules, like antibodies, which recognize and bind to a specific protein/receptor expressed on the surface of cells [44][61]. For example, due to the high angiogenesis rate in tumours, tumour blood vessels have an abnormal expression of receptors or antigens on their surface. Arginine-glycine-aspartate acid (RGD) is one of the ligands that can be functionalized at nanomaterials surface to target a specific protein overexpressed at tumour vessels, the integrin receptor $\alpha_v\beta_3$. Endothelial growth factor receptor 1 and receptor 3 (VEGFR-1) (VEGFR-3) are also proteins with a high expression rate on tumour vascular endothelial cells. Moreover, cancer cells have an aberrant expression of proteins and receptors at the membrane surface, which can be useful to improve the targeting of these nanomaterials. Folic acid (FA), hyaluronic acid (HA), phenylboronic acid (PBA), aptamers and peptides are examples of ligands used to target overexpressed proteins at the cancer cell surface. Namely, FA recognizes the folate receptor, Ha recognizes the CD44 receptor, and PBA binds to the sialic acid receptor. Furthermore, active

targeting can also be used to deliver nanomaterial or chemotherapeutic drugs to specific subcellular organelles. For example, Doxorubicin (DOX) inhibits the activity of topoisomerase II in the cell nucleus, and Paclitaxel (PTX) inhibits the microtubule depolymerization in the cell cytoplasm. Thus, the delivery of these chemotherapeutic agents to the respective organelle of activity improves their therapeutic effect. Mitochondria, nucleus, Golgi apparatus and endoplasmic reticulum are examples of desired targeting organelles chosen due to their involvement in apoptosis mechanisms and cell survival [63]. Together, these two types of targeting can be conjugated to increase the accumulation of nanosystems at the predicted target and thus, improve the application of nanomaterials in oncology [44][61]. **Table 1.1** summarizes formulated nanomedicines to target specific cell receptors or cell organelles.

Table 1.1 Different types of formulated nanomedicines designed for a specific target and a specific therapeutic outcome.

Nanomedicines	Cellular Target	Outcome	Article
RGD-LCL-Liposome functionalized with RGD peptide and Doxorubicin encapsulated	Cancer vessels - receptor $\alpha_v\beta_3$	✓ Increased the accumulation of DOX in tumour tissues by targeting endothelial cells.	[64]
Vincristine-loaded on F56-peptide nanoparticles F56-VCR-NPs	VEGFR-1	✓ Improved the distribution of Vincristine to cancer cells. Increase the antiangiogenic potential of this drug. ✓ Achieved significant apoptosis of tumour vascular endothelial cells.	[65]
Folate-modified poly(2-ethyl-2-oxazoline) as doxorubicin carrier	Folate Receptor	✓ Functionalising micelles with FA improve their recognition by cancer cells and increases the DOX delivery by FR-mediated endocytosis.	[66]
HA-ss-DOCA micelles	CD44 receptor	✓ The targeting mediated by hyaluronic acid via the CD44 receptor improved the accumulation of micelles in the tumour site. ✓ This system has proven to be a good approach for the intracellular release of the Paclitaxel drug.	[67]
Pillar[5]arene-based [2]rotaxane	Mitochondria of cancer cells	✓ Triphenylphosphonium (TPP) was used for mitochondrial targeting. ✓ This system was conjugated with DOX, to improve the enrichment of DOX into mitochondria of cancer cells.	[68]
CTPP-CSOSA – Celastrol-loaded micelles	Mitochondria of cancer cells	✓ The lipophilic cation CTPP was used for mitochondrial targeting. ✓ Release of Celastrol, an acidic drug that acts on mitochondrial respiratory chain complex I.	[69]

PECL/DA-TAT-M	Nucleus of cancer cells	✓ Tat peptide was functionalized at micelle surface to enhance tumour cells targeting, as well as the nucleus of cancer cells; ✓ These micelles were used as a carrier of 10-Hydroxycampothecin (HCTP), an inhibitor of Topoisomerase I.	[70]
Retinoic acid conjugated chondroitin sulfate (CS-RA) nanoparticles	Golgi apparatus	✓ Retinoic acid and Chondroitin sulfate have an affinity for CD44 receptors overexpressed at cancer cells membrane as also for the Golgi apparatus; ✓ Paclitaxel is loaded in nanoparticles to be delivered to the Golgi apparatus of cancer cells.	[71]

1.3.2 Nanoparticles

Nanoparticles (NPs) are nanoscale particles with sizes ranging between 1 and 100 nm [72]. They can be subdivided into organic and inorganic NPs (**Figure 1.8**). Organic NPs include dendrimers, lipid-based nanoparticles and polymeric NPs [73]. Inorganic NPs, which include quantum dots, iron oxide nanoparticles and gold nanoparticles, are the main ones used in biomedical applications [61][73][74]. The small size and large ratio between the surface area to volume of nanoparticles give them different properties compared to the bulk material [1]. As previously mentioned, these properties include shape-dependent electronic and optical properties, surface chemistry and size [56][72][74]. Overall, these properties render them ideal for different applications, i.e. i) drug and gene delivery; ii) vaccine

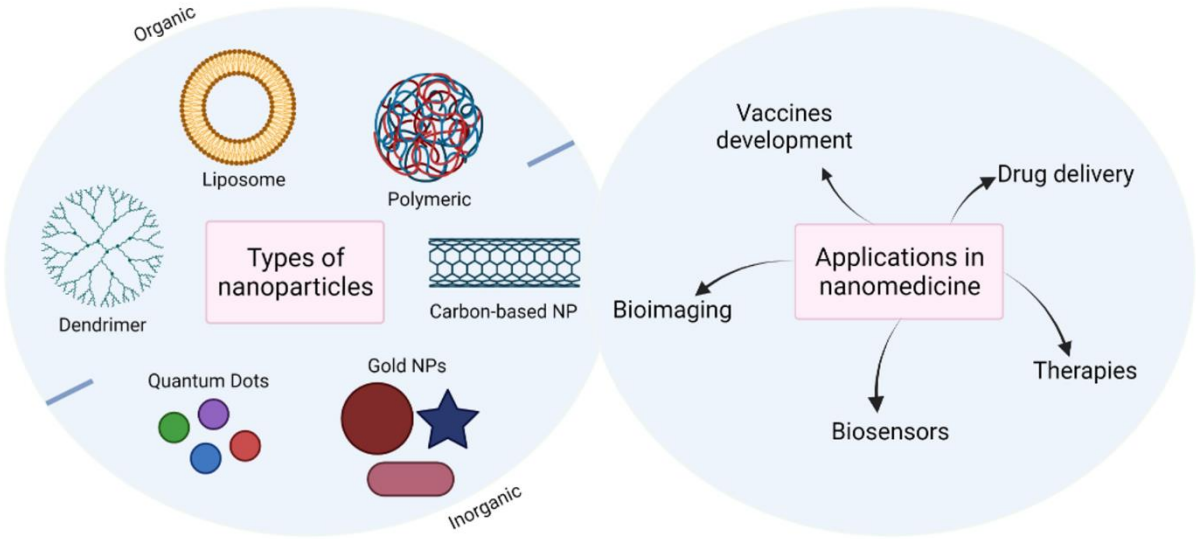

Figure 1.8 Types and applications of nanoparticles in nanomedicine. Nanoparticles can be divided in two major groups according to their composition: I) Organic nanoparticles which include Dendrimers, Liposomes as Polymeric nanoparticles; II) Inorganic nanoparticles which include Quantum Dots, Gold nanoparticles and Carbon-Bases nanoparticles. Furthermore, these types of nanoparticles may have prominent applications in medicine, such as I) Drug delivery; II) Vaccines development; III) Therapies; IV) Bioimaging and V) Biosensor. Created in Biorender.com and adapted from [73].

development; iii) biosensors; iv) bioimaging and v) therapies [72][61][56]. Additionally, NPs can simultaneously be used for diagnostic and therapy as a theragnostic system (**Figure 1.8**) [56].

Bioimaging, the visualization of body tissues or biological processes in real-time, is critical for diagnosing and monitoring disease progression. There are many bioimaging techniques, including i) magnetic resonance imaging (MRI); ii) ultrasounds; iii) fluorescence imaging; iv) positron emission tomography (PET), and v) computed tomography (CT), which use probes or contrast agents [75]. However, these current bioimaging techniques have some disadvantages, such as low spatial resolution and low sensitivity [76]. Nanomaterials with fluorescent features (quantum dots, gold nanoparticles, magnetic nanoparticles, carbon-based nanomaterials, nanocrystals and silica nanoparticles) are prominent in this field, as they have high photostability and quantum yield. Moreover, nanomaterials can simultaneously provide real-time biodistribution imaging and delivery of therapeutic agents. For example, Misra et al. [77] formulated a ZnO-QD-chitosan-folate carrier, a multifunctional nanomaterial with bioimaging properties due to the ZnO quantum dot and therapeutic properties due to the degradable chitosan loaded with doxorubicin. In MRI, Gadolinium (paramagnetic substance) is used as a contrast agent, however, it has some toxicity associated with it [76]. Thus, due to their intrinsic magnetic properties, superparamagnetic iron oxide nanoparticles (SPIONs) are an alternative to be used as negative agent contrast with high biocompatibility and low toxicity [78]. Rahim et al. [79] synthesized the SPION/PVD/$MUC1_{Apt}$/DOX, a nanomaterial able to provide MRI imaging of colon cancer due to the SPION properties, to target colon cancer cells due to the $MUC1_{Apt}$ (an aptamer with selectivity for an overexpressed protein (MUC1) in human colon cancer), and it also has a therapeutic component, the doxorubicin. Gold nanoparticles have a unique optical property (as discussed in section 1.3.3), allowing them to absorb and scatter light stronger than organic dyes. In optical imaging, AuNPs can act as a contrast agent in some techniques such as two-photon or multi-photon luminescence, computed tomography photoacoustic imaging, etc. [80][81][82] Beyond the intrinsic optical properties of AuNPs, they can also be modified with fluorophores providing plasmon-enhanced fluorescence imaging [82]. Shijin et al. [81] synthesized a PPHAuNCs-TNCs nanoparticle complex with theragnostic application, once gold nanoparticles were modified with a microRNA for gene therapy. Their biodistribution and accumulation were monitored by fluorescence (micro-RNAs were labelled with Sulfo-Cyanine5.5 fluorescent dye) and photoacoustic tomography imaging (achieved by the high absorption of gold nanoparticles in the NIR wavelength).

Organic nanoparticles, such as liposomes and micelles, have a great potential in biomedical applications, mainly as carriers of compounds [61][83]. However, the lack of some properties in organic nanoparticles, such as optical or magnetic properties, makes inorganic nanoparticles a better approach in many medical applications [61]. Doxil, a Doxorubicine carrier liposome, was the first nanoparticle-based treatment approved by the Food and drug administration (FDA). This is an organic nanoformulation where Doxorubicin is encapsulated in a polyethylene glycol liposome. Myocet, Depocyt, Abraxane and Nano-Therm are also examples of FDA approved nanoparticles as new cancer therapies [83]. According to Clinical Trials.gov, there are around 29 active clinical trials in cancer investigation with nanoparticle approaches (www.clinicaltrials.gov).

1.3.3 Gold Nanoparticles in cancer therapy

Gold nanoparticles (AuNPs) have great potential in biomedical applications due to several properties, including i) biological non-reactive; ii) high ratio between surface area/volume that facilitates the functionalization of surface; iii) easily to manipulate physical-chemical properties during this synthesis; iv) chemical inert; v) high optical properties [1][38][72]. Furthermore, because of features mentioned above, gold nanoparticles are a great bet in disease diagnostic, treatment, and tracking, with prominence in cancer [38][72].

AuNPs have been reported to have low toxicity although some toxicity exists, and it is mainly correlated with their size. The relation between the particle size and toxicological effect is explained by the facility of smaller nanoparticles suffering uptake by cells, therefore, in general, smaller AuNPs have a higher cytotoxic effect [84]. However, a study performed by Zhang et al. reported that AuNP@PEG with sizes between 10 nm and 60 nm cause some cytotoxic effects while AuNP@PEG with 5 nm to 30 nm does not appear to induce toxicity [85]. Several in vitro assays can be performed to evaluate cytotoxicity by AuNPs, mainly to assess metabolic activity, cell viability or proliferation cell rate. Among them, MTS (3-(4,5-dimethylthiazol-2-yl)-5-(3-carboxymethoxyphenyl)-2-(4-sulfophenyl)-2H-tetrazolium) assay, is one of the colorimetric assays used to evaluate if cells are metabolically active. Damages in cell membranes and oxidative stress can also be consequences of AuNPs and these can be assessed by lactate dehydrogenase assay or adenosine tri-phosphate assay and by DCFDA assay, respectively [84].

Surface modification of AuNPs provides a broad range of advantages, some of them associated with a decrease in cytotoxicity [84]. Furthermore, surface modification is commonly used to improve drug loading, cellular uptake, stability, actively targeting, retention time and decrease immunogenicity [1][72]. These molecules include poly(ethylene) glycol (PEG), antibodies, peptides, nucleic acids, and drugs. The functionalization is planned with a specific purpose, as a specific target or a specific drug delivery. Coating AuNPs would also support cellular and intracellular targeting and their internalization into the target cells [74]. Pegylation (coating nanoparticles with PEG molecules) is one of the main functionalization methods for gold nanoparticles, once it prevents aggregation, avoids immune recognition and improves the retention time in blood, as mentioned above. Gold nanoparticles have a high affinity for Sulfur elements, and thus, Pegylation is promoted by a reaction between the Thiols group at the 5’ position and the surface of the gold particle. Additionally, PEG molecules can also be bifunctional, with an additional group in the 3’ position, such as the carboxyl or amine group, useful for further functionalization with biomolecules, such as proteins [38][74].

Among the several applications of AuNPs, they can be used as vehicles for drug delivery, such as chemotherapeutic agents. The easily surface modification of AuNPs allows the attachment of drugs and proteins, like antibodies, which assign specificity to cancer cells. This approach reduces the chance of damaging healthy cells. Drugs can be conjugated with AuNPs through covalent or non-covalent forms. Usually, covalent linkages are used to conjugate pro-drugs, while non-covalent linkages are used to attach drugs in the active form [38]. An example is the NanoTS265, gold nanoparticles functionalized

with a chemotherapeutic coordination compound and an antibody against the epidermal growth factor receptor (EGFR) (overexpressed in cancer cells) synthetized by Fernandes et.al [85]. This nanoformulation successfully delivered the chemotherapeutic compound to CRC cells, both *in vitro* and *in vivo,* with improved cancer cell death and tumour growth suppression [86].

1.3.4 Phototherapy mediated by Gold Nanoparticles

The optical properties of gold nanoparticles are associated with an optical phenomenon designated by localized surface plasmon resonance (LSPR). LSPR is one of the most important properties of gold nanoparticles and it is dependent on different factors associated with surface properties, such as size, shape, and surface functionalization [43][45]. LSPR occurs when a light source interacts with free electrons at the nanoparticle surface, which causes a dipole oscillation in a conduction band [1][43][45]. The frequency at which the amplitude of oscillation is maximum corresponds to the SPR peak, and it can range from visible to infrared spectrum [45]. Light absorption and scattering are dependent on the physical dimension of nanoparticles and also on the medium of the colloidal solution. Small nanoparticles absorb light with a small wavelength (blue light) and consequently reflect red light. Large nanoparticles absorb red light and reflect blue light [43]. These unique optical properties of AuNPs make them useful to cancer management through the labelling of target tissues and cancer treatment by plasmonic photothermal therapy [38].

AuNPs can be activated by NIR and visible light and act as PTT agents, since the dipole oscillation of electrons at the nanoparticle surface when exposed to radiation increases the local temperature [43]. Therefore, AuNPs can be applied as a source of controlled heating in biological tissues, which is known as hyperthermia [38][44][87]. Roma-Rodrigues et.al [88] combined AuNPs phototherapy and chemotherapy (using DOX) to overcome drug resistance. Here, 3D models of CRC cells (HCT116), resistant or not to DOX, were exposed to AuNP@PEG, followed by green laser irradiation, which culminated in the disintegration of 3D cells model and consequently, DOX was able to penetrate the core of the 3D cell model. Moreover, combining these two therapeutic approaches decreased the DOX concentration needed to achieve the same therapeutic effect, which may allow to decrease possible side effects.

1.3.5 Cellular uptake and intracellular traffic of nanoparticles

In the bloodstream, AuNPs are in contact with many serum proteins, which adsorb onto their surface, a phenom known as opsonization. This increases the recognition of AuNPs by phagocytic cells and thus, decreases the circulation lifetime of nanoparticles. Some approaches can be made to prevent such events, such as coating the surface of nanoparticles with polymers like PEG. Consequently, increasing the circulating time enhances the passive targeting of AuNPs by the EPR effect [89][90][91].

The uptake of nanoparticles by cells is mainly dependent on their size, shape, superficial charge, concentration, receptor-ligand interaction, protein-corona properties, and retention time [92][89]. As cellular membranes are negatively charged, neutral and positive particles interact more efficiently with cell surfaces [89][92]. There are two main pathways by which particles internalize cells: active transport (endocytosis) or passive transport (penetration through the cell membrane) [84][89]. The preferential mechanism of NPs uptake by cells is the receptor-mediated endocytosis, where a ligand binds to the specific receptor and induces its internalization by membrane invagination. This mechanism depends on several points, such as the number of particles and receptors available to recognize the ligands [84]. Small particles at the nanoscale are internalized by a type of endocytosis known as Pinocytosis (**Figure 1.9**). In Pinocytosis, cells' membranes form an intern invagination leading to a vesicle (Pinosome) which fuses with lysosomes [93]. Pinocytosis is subdivided into clathrin-mediated endocytosis, caveolae-mediated endocytosis, clathrin/caveolin independent endocytosis, and macropinocytosis [84][89][93]. Macropinocytosis has the particularity of bypassing the fusion with lysosomes, and due to this characteristic, achieving the uptake of NPs by this pathway can be advantageous since it prevents NPs from being exposed to lysosomal enzymes. The internalization pathway elected by nanoparticles depends on several features, such as their size, shape, superficial charge and modification, etc. Although these parameters can be controlled during nanoparticle synthesis, nanoparticles are subject to further and uncontrolled modification after their administration, making it difficult to predict the

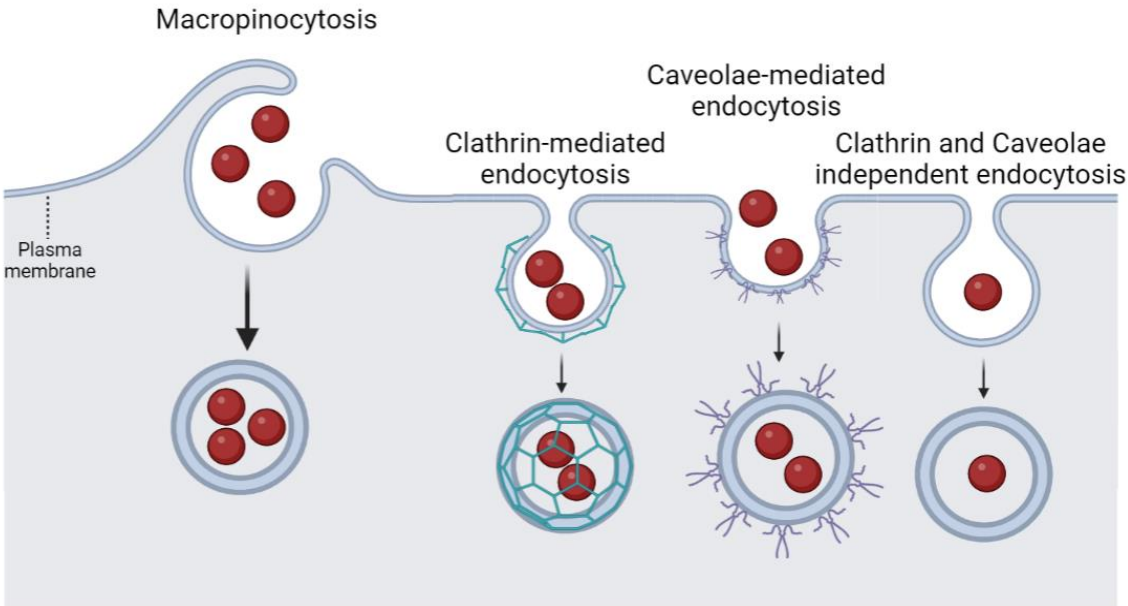

Figure 1.9 Uptake of nanoparticles by the four pinocytosis pathways: Macropinocytosis, Clathrin-mediated endocytosis, Caveolae-mediated endocytosis and Clatherin and Caveolae independent endocytosis. Macropinocytosis is receptor-independent endocytosis which forms large vesicles (≈10μm) called macropinosomes. Caveolae-mediated endocytosis is characterized to Involve nanoparticles in a vesicle named by Caveolae, covered by Cavin proteins. Clathrin and Caveolae independent endocytosis. In Clathrin-mediated endocytosis, when AuNPs interacts with specific membrane receptors, they activate endocytosis machinery and vesicles coated by clathrin are formed. Clathrin/Caveolae independent endocytosis is a set of endocytic pathways where vesicles are not coverage by specific proteins Created in Biorender.com and adapted from [137].

internalization pathway [93]. A study performed by Chithrani et al. demonstrated that i) gold nanoparticles uptake is dependent on their size: the increasing of size increases the uptake rate, and the maximum of internalization is reached when nanoparticles size is 50nm; ii) Uptake kinetics is dependent on the time of incubation: The uptake increased for the first 2 hours and then slowed and reached a plateau; iii) Uptake is also dependent on the shape of nanoparticles: spherical nanoparticles have a higher uptake rate than rod-shaped nanoparticles [92].

When inside cells, nanoparticles can have different fates. Elucidating the intracellular targeting of nanoparticles, as well as the time until their degradation or excretion, is essential to achieve the desired effect. However, knowledge about this intracellular traffic is still low. It is known that after uptake, nanoparticles are confined in endosomes, which undergo several maturation steps where changes at the intravesicular pH are prominent. Endosomes fuse with lysosomes, where the content is exposed to enzymatic digestion. This enzymatic digestion can impair the effectiveness of nanoparticles' intended biological function, and therefore, escape from endosomal degradation needs to be considered when nanosystems are formulated. Some approaches facilitate their endosomal scape, such as functionalizing nanoparticles with membrane destabilizing peptides i.e. surface cell-penetrating peptides (CPPs) [94]. Many surface modifications in nanoparticles, as mentioned earlier, can be performed to guide nanoparticles to a specific intracellular organelle. For example, nanoparticle surface modification with folic acid [95] or nuclear localization sequence (NLS) peptide [96] induces nucleus targeting; with TPP [97], Dequalinium (DQA) [98] or Dmt-D-Arg-Phe-Lys-NH2 peptide [99] induces mitochondria targeting and with L-cysteine moieties, the golgi apparatus targeting is achieved [100] (see **Table 1.1**).

Lee et al. observed that SPIONs coated with poly lactic-co-glycolic acid (PLGA) are fully internalized by mesenchymal stem cells mainly by clathrin-dependent endocytosis 24 hours after treatment. Furthermore, when inside cells, nanoparticles were co-localized with lysosomes up to 60 hours post-treatment. However, they were unable to study the fate of nanoparticles after lysosome encapsulation [101]. In another study, Qian et al. synthesized AuNPs functionalized with RGD peptide and NLS peptide for nuclear delivery (NLS-RGD-PEG-AuNP). They observed that nanoparticles were internalized mainly by receptor-mediated endocytosis (due to the recognition of RGD peptides by the receptors onto the cell surface), escaped from lysosomes and accumulated in the nuclei region [96]. For targeting mitochondria, Mkandawire et al. functionalized a gold nanoparticle with a green fluorescent protein (MitoTGFP) that has an affinity for the inner membrane protein COX8 (Cytochrome c oxidase subunit 8) and therefore, the delivery and tracking of AuNPs are simultaneously possible. The uptake of AuNPs was facilitated by covering the MitoTGFP-AuNP with the cationic PPI-Mal-III G3, a transfection compound. They observed that AuNPs were internalized mainly by caveolin-mediated endocytosis, and then they were localized in early endosomes. However, some endosomes containing AuNPs were ruptured and released their content into the cytoplasm. By active targeting, Mito-AuNPs targeted the inner mitochondrial membrane, crossing the OMM, and partially disrupting it. Disruption of the OMM led to the release of cytochrome c, which consequently triggered apoptosis [102].

1.4 Scope of the thesis

The high incidence and mortality rate from CRC and the low specificity of current cancer therapies for cancer cells, as well as the side effects associated with them, underscore the importance of studying and developing new therapeutic approaches. Furthermore, the important role of mitochondria in cancer development, maintenance and their involvement in cell death pathways allow them to be a potential target for therapeutic approaches. Nanomedicine is a new field of investigation that has been attracting great attention, as new properties and strategies given by nanomaterials can improve targeting to specific cells and organelles, reduce side effects, and increase the therapeutic effect of some current therapies. AuNPs stand out among the wide variety of nanomaterials due to their unique optical properties and the LSPR effect. Thus, the aims of this thesis are to formulate a new gold nanoconjugate to target mitochondria of colorectal carcinoma cancer cells (HCT116 cell line) and kill them by visible laser irradiation inducing AuNPs-mediated localized hyperthermia. Mitochondrial targeting will be achieved by functionalizing AuNPs with an antibody against a protein expressed in the outer membrane of mitochondria (Hexokinase I). Therefore, functionalized AuNPs are expected to be taken up by HCT116 cells and accumulate in mitochondria by active targeting. With this new mitochondrial-targeted nanoformulation, we aim to achieve, increase, and optimize photothermal therapy using a green laser. Concentrating AuNPs in mitochondria at the time of irradiation could be a new approach to improve the therapeutic effect against CRC.

2

MATERIALS AND METHODS

2.1 Materials

2.1.1 Reagents

- 1-ethyl-3-(3-dimethylaminopropyl)carbodiimide hydrochloride (EDC, Sigma-Aldrich, USA)
- 25 cm^3 and 75 cm^3 T-Flask (SPL Life Sciences, South Korea)
- 5,5'-dithio-bis(2-nitrobenzoic) (DTNB, Promega, Madison, USA)
- Albumin Serum Bovine (BSA, Nzytech, Lisbon)
- Alpha-Thio-omega-(propionic acid) octa (ethylene glycol) (HS-PEG(8)-COOH; Cas no. 866889-02-3, IrisBiotech, Germany)
- Anti-Hexokinase I (Cat. No. ab150423, Abcam, Cambridge, UK)
- Anti-rabbit IgG (TRITC) (Cat. No. ab6718, Abcam, UK)
- Anti-Rabbit IgG HPR-Linked (Cat. no. 7074, Cell Signalling Technology, Massachusetts, USA)
- *Cell Fractionation Kit* (Cat. No. ab109719, Abcam, UK)
- CellLight™ Mitochondria-GFP ((Cat. No. C10508, ThermoFisher, USA))
- CellTiter 96® AQ_{ueous} Non-Radioactive Cell Proliferation reagent (Promega Madison, EUA)
- *Coomassie* Reagent (Cat. No:23200, ThermoFisher Scientific, USA)
- *Dulbecco's Modified Eagle Medium* (DMEM; Gibco™ ,Thermofisher Scientific), USA)
- *Fetal Bovine Serum (FBS;* Gibco, ThermoFisher Scientific, USA)
- *HCT116* (ATCC® CCL-247™)
- Hoechst 33258 dye ((Molecular Probes® ThermoFisher, USA)
- N-hydroxysulfosuccinimide (Sulfo-NHS, Sigma-Aldrich, USA)
- Nitrocellulose membranes (Amersham™ Protran™ Premium 0.45 µm NC, Sigma-Aldrich, USA)
- Pierce ™ 660 nm Protein Assay (Cat. No:22662, ThermoFisher, USA)
- Trypan Blue 0.4 % (v/v) (Gibco™, Thermofisher Scientific, USA)
- TrypLE™ Express (Gibco®, New York, EUA)
- WesternBright ECL substrate (Advansta, Menlo Park, California, USA)

2.1.2 Equipment

- CXX41 inverted microscope (Olympus, Japan)
- Hemacytometer (Hirschmann, Eberstadt, Germany)
- Microplate reader Infinite M200 (Tecan, Switzerland)
- Nikon Inverted Ti-U Eclipse microscope (Nikon, Japan)
- Refrigerated SIGMA 3-16K centrifuge (SIGMA,Sartorius, Germany)
- SANYO CO2 Incubator (Electric Biomedical Co., Osaka, Japan)
- Ultrasonic bath (Elma Schimidbauer GmbH, Germany)
- UV-Visible Spectrophotometers (UVmini-1240 Shimadzu, Japan and Evolution 300 UV-Vis Spectrophotometer)
- Zetasizer NanoZS ZEN 3500 (Malvern, UK)

2.2 Gold nanoparticles' synthesis

Gold nanoparticles were synthesized by the citrate reduction method as described by Lee and Maisel/ Turkevich [103][104].

Firstly, all glassware needed for the synthesis were washed with fresh Acqua Regia (3 HCl: 1 HNO_3) and then with MiliQ water until the pH inside the glassware equalled the pH of the water. The washing step with Acqua Regia is crucial to ensure that the synthetized gold nanoparticles are free of contaminants, as it dissolves noble metals [104]. In a round bottom flask with a condenser, 250 mL of 1 mM chloroauric acid ($HAuCl_4$) were boiled. When in reflux, 25 mL of 38.8 mM trisodium citrate were quickly added. In this step, trisodium citrate is responsible for reducing Au^{3+} ions to Au^0 and consequently, gold begins to precipitate forming small clusters. The growth of these clusters progresses until their surfaces are saturated with citrate ions [104]. When AuNPs synthesis occurred, a rapid colour change of the mix from yellow to red was observed (**Figure 2.1**). After the colour changed, the system was kept boiled for 30 minutes with continuous stirring. Then, the system was turned off and cooled to room temperature (RT). The resulting gold nanoparticles stabilized by a citrate layer (AuNP@Citrate) were filtered under sterile conditions using a syringe with a 0.2 µm filter and stored away from light.

Figure 2.1 Gold nanoparticles synthesis setup.

2.3 Gold nanoparticles characterization

2.3.1 UV Visible Spectroscopy

UV-Visible spectroscopy measures the light absorbed by a sample at wavelengths between the ultraviolet and near-infrared light. It allows characterizing nanoparticles in terms of surface modifications, colloidal stability and estimating their size and concentration. The maximum absorbance value for a AuNPs solution measured corresponds to the wavelength where the SPR effect occurs. The diameter (d) of nanoparticles coated with citrate is calculated through the absorbance value at the SPR wavelength ($\mathrm{A_{spr}}$) and at 450 nm ($\mathrm{A_{540}}$), using the equation described by Haiss et.al (**Equation 1**) (see **Figure 4.1** in appendix) [105]. The concentration of AuNPs solutions ($[\mathrm{AuNPs}]$) was calculated by the Lambert-Beer law (**Equation 2**), where l is the optical path length and ε the molar extinction of AuNPs. UV-Visible analysis can also give some additional information, such as the aggregation rate of AuNPs, calculated through the absorption values at 525 nm ($\mathrm{A_{525}}$) and 585 nm ($\mathrm{A_{585}}$) (**Equation 3**) [106][107]. Higher aggregation index corresponds to a high aggregation ratio of nanoparticles in solution [106]. Thus, UV-Visible absorption spectra of AuNPs solutions were obtained using a UV-Visible Spectrophotometer, with 1 cm path quartz Suprasil® cuvettes at RT. Absorbance values of AuNPs were measured in a wavelength range between 400 and 700 nm, in triplicates to each sample, against the correspondent blank.

Equation 1. $$d(nm) = 0.112 \times e^{2.9986 \times \frac{A_{spr}}{A_{450}}}$$

Equation 2. $$[AuNPs] = \frac{A_{spr}}{\varepsilon \times \mathrm{l}}$$

Equation 3. $$Aggregation\ index = \frac{A_{585}}{A_{525}}$$

2.3.2 Dynamic Light Scattering

Dynamic light scattering analysis measures the hydrodynamic diameter (D_H) of suspended nanoparticles, based on Brownian motion: small particles move faster than larger ones. Following this statement, the light scattered by nanoparticles gives information about their size through the Stokes-Einstein equation (**Equation 4**), where k is the Boltzmann's constant, T is temperature (K), η is the solvent viscosity and D is the diffusion coefficient. Indeed, the size distribution of nanoparticles is defined by the Z-average size and the Polydispersity Index (PdI). Z-average is the average of the accumulative sizes in a sample and PdI is an indicator of the polydispersity in nanoparticles sizes.

For DLS analysis, AuNPs solutions were diluted with MiliQ-Water to a final concentration of 4nM. Three measurements of each sample were performed at 25°C with a 90° detection array using the Nanoparticle Analyzer SZ-100, as a service (Nano4 Global, Lda).

Equation 4. $$D_H = \frac{kT}{3\pi\eta D}$$

2.3.3 Zeta Potential

Zeta potential gives information about the surface charge of nanoparticles. When in solution, charged nanoparticles are covered by oppositely charged ions which form a double layer around nanoparticles. Thus, Zeta Potential measures the charge on the outer layer, designated by the slipping plane. Zeta Potential values are influenced by solution conditions, such as pH, salinity, concentration, ionic strength, and temperature. When the value of zeta potential is between -10 and 10 mV, nanoparticles are neutral. When the value is greater than 30 mV or less than -30 mV, nanoparticles are defined as positive or negative charged, respectively. In addition, information about the colloidal stability of nanoparticles can also be obtained by Zeta potential value. That is, when Zeta potential is higher than +25 mV and less than -25 mV, electrostatic repulsion forces between nanoparticles keep them stable in solution and aggregates are unfavourable to form [108].

The Zeta Potential analysis of AuNPs solutions was performed simultaneously with the DLS analysis, as a service (Nano4 Global, Lda).

2.4 Functionalization of AuNPs

2.4.1 Gold nanoparticles pegylation with HS-PEG(8)-COOH

Gold nanoparticles synthesized previously were functionalized with Alpha-Thio-omega-(propionic acid) octa (ethylene glycol) (HS-PEG(8)-COOH, Molecular Weight: 458,57 g/mol), a thiol PEG molecule with a carboxylic group in the 3' position (see **Figure 2.4**). Citrate molecules adsorbed to the surface of AuNP@Citrate are easily replaced by other molecules, mainly if they contain a sulfhydryl group, since it has a high affinity for gold [109]. Hence, Pegylation was performed following the protocol described by A.Fernandes et al. [86]. In order to get 100 % of the nanoparticles' surface covered with HS-PEG(8)-COOH, a reactional mixture containing 10 mM of AuNP were incubated with 0.0115 mg/mL of HS-PEG(8)-COOH and 0.028 % (w/v) SDS solution for 16h, under agitation at RT. The amount of HS-PEG(8)-COOH needed to cover 100 % of the surface of 14 nm nanoparticles was previously established by J.Conde (Supporting information [110]). However, to ensure 100 % of covering, HS-PEG(8)-COOH was added with 15 % excess. After the incubation time, the solution was centrifuged (14 000xg for 30 minutes at 4°C) to remove unbound PEG. The unbound PEG in the supernatant were further quantified by the Ellman's assay (section 2.4.1.1). The pellet containing the pegylated AuNPs (AuNP@PEG-COOH) was resuspended in MiliQ-Water, characterized by UV-Visible, DLS and Zeta-Potential, as described in sections 2.3 and stored at 4°C.

2.4.1.1 Ellman's assay

The amount of unbound HS-PEG(8)-COOH chains was quantified by the Ellman's assay [104]. Ellman's assay is based on a reaction between free thiolate chains in solution and DTNB (5,5'-dithio-bis(2-nitrobenzoic)) (**Figure 2.2**). When this reaction occurs, a coloured compound (TNB- 2-nitro-5-thiobenzoic acid) with a high molar extinction coefficient at a wavelength of 412 nm is formed.

Briefly, 200 µL of stock solution or test samples were mixed with 100 µL of phosphate buffer (0.5 M pH=7) and 7 µL of DNTB 5 mg/mL in phosphate buffer (0.5M pH=7). The reaction occurred for 10 minutes and then the absorbance at 412 nm was measured [111]. The amount of HS-PEG(8)-COOH in samples was calculated using a calibration curve with a range of concentrations between 0.0002-0.035 mg/mL of HS-PEG(8)-COOH (see **Figure 4.2** in appendix). The difference between the amount of PEG chains added to the reaction and the amount of PEG in the supernatant of the reaction allowed the estimation of the pegylation yield. All quantifications were performed in triplicate.

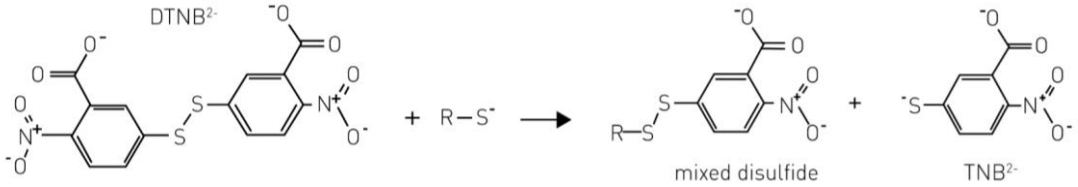

Figure 2.2 Ellman's assay reaction. DTNB, when in solution, reacts with free sulfhydryl groups (R-S). TNB results from this reaction, and as it has a high molar extinction at 412 nm, it can be quantified by UV-Visible spectroscopy, using a proper calibration curve. Thus, free HS-PEG(8)-COOH in solution can be quantified through this assay. Adapted from www.bmglabtech.com

2.4.2 Conjugation of Anti-Hexokinase I at pegylated gold nanoparticles surface

Pegylated gold nanoparticles were conjugated with Hexokinase I antibody (see **Figure 2.4**) via EDC/NHS (1-ethyl-3-(3-dimethylaminopropyl)carbodiimide/*N*-hydroxysuccinimide) reaction (**Figure 2.3**), following the protocol described by A.Fernandes et.al, with slight modifications [86]. EDC (1-ethyl-3-(3-dimethylaminopropyl)carbodiimide hydrochloride) is a carbodiimide, a crosslinking agent for carboxylic acids in aqueous solutions. It reacts with carboxylic acid groups and gives rise to an active intermediate, O-acylisourea. In a reaction mixture containing primary amines, O-acylisourea favours the formation of a peptide bond between the primary amine and the carboxylic group. Sulfo-NHS (N-

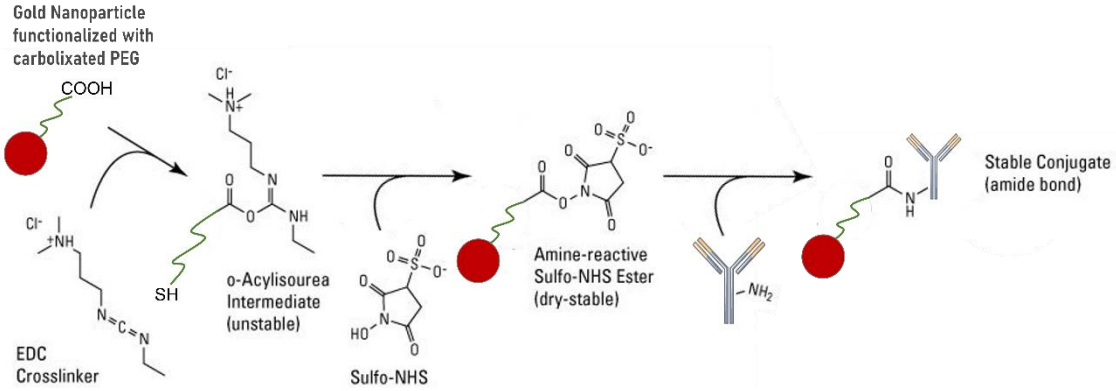

Figure 2.3 Antibody-functionalized gold nanoparticles by the EDC/NHS reaction. The carboxylic group in the HS-PEG(8)-COOH previously functionalized on the gold nanoparticles surface reacts with EDC crosslinker in solution giving rise to an unstable Intermediate (O-Acylisourea). Sulfo-NHS reacts O-Acylisourea and a stable intermediate is formed. Then, the antibody (Anti-Hexokinase I) added to the reaction mixture is conjugated to the HS-PEG(8)-COOH through an amide bond formation. Adapted from www.thermofisher.com.

hydroxysulfosuccinimide) is included in this reaction as it improves the reaction efficiency by reacting with O-acylisourea and forming a more stable intermediary [72].

Briefly, 21 nM of AuNP@PEG-COOH were mixed with 1.25 mg/mL of Sulfo-NHS and 0.312 mg/mL of ECD in MES Buffer 10 mM pH=6.1. The mixture was incubated for 30 minutes, at RT, and then it was centrifuged at 14 000xg for 30 minutes at 4°C. The pellet was resuspended in MES buffer 2.5 mM pH=6.1 and then the Hexokinase I antibody was added in order to get 5 antibodies per AuNP (see section 3.1) and incubated overnight. After incubation, the mix was washed twice with MES buffer 2.5 mM pH=6.1, through centrifugation at 14 000 x g for 30 minutes at 4°C. Supernatants were stored for later quantification of free antibodies by the Bradford assay (section 2.4.2.1). The pellet that contains the AuNP@PEG-COOH@Anti-Hexokinase I was resuspended in MiliQ-Water, characterized by UV-Visible as described in section 2.3.1 and stored at 4°C until utilization.

2.4.2.1 Bradford Assay

Bradford assay is a method used to measure the concentration of total protein in a sample. Under acidic conditions Coomassie Brilliant Blue G-250 is in a red cationic form and its maximum light absorbance occurs at 470 nm. When mixed with protein samples, it reacts with proteins and is converted to a cationic blue form with a maximum absorbance of 595 nm. Therefore, measuring the absorbance at 595 nm allows to quantify the protein concentration in a sample [112][113][114]. In this work, the Coomassie (Bradford) Protein assay in microplate format was used to indirectly estimate the number of functionalized antibodies on the surfaces of gold nanoparticles.

Briefly, 50 µL of bovine serum albumin (BSA) solution or supernatant sample were mixed with 50 µL of Coomassie Reagent in a 96-well plate. The plate was incubated for 10 minutes at RT and the absorbance at 595 nm was measured on the microplate reader. The calibration curve was performed using BSA protein in a range of concentrations between 1-25 µg/mL (see **Figure 4.3** in appendix). All the quantifications were performed in triplicate. The conjugation yield of anti-Hexokinase I with gold nanoparticles was calculated by **Equation 5**, where $[Ab]_0$ is the total concentration of antibody added to the reaction and the $[Ab]_s$ is the concentration determined by this assay which remained in the supernatant [107].

Equation 5. $$(\%\ Yield\ of\ Ab\ conjugation) = \frac{[Ab]_0 - [Ab]_s}{[Ab]_0} \times 100$$

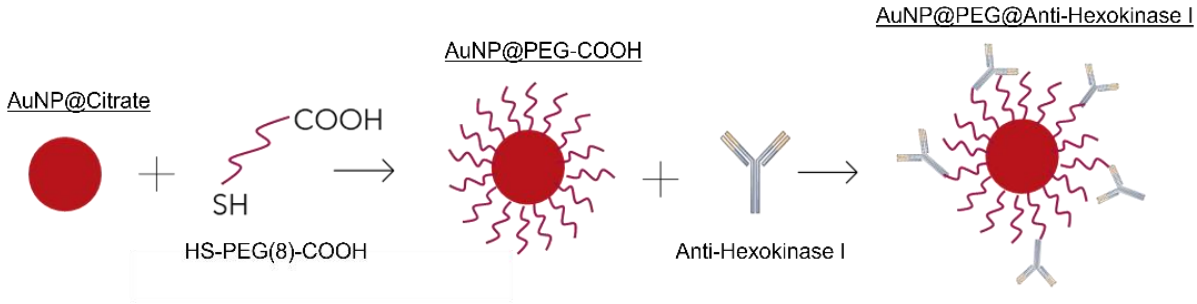

Figure 2.4 Schematic representation of the three main functionalization steps of gold nanoparticles. First, gold nanoparticles coated by citrate molecules were functionalized with HS-PEG(8)-COOH to ensure stability and facilitate the following reaction: Conjugation with Anti-Hexokinase I. As a result, gold nanoparticles functionalized with Anti-Hexokinase I were obtained.

2.5 Maintenance of HCT116 cell culture

Cellular experiments were performed using the colorectal cancer cell line HCT116 (ATCC® CCL-247™). This line originated from cells isolated from a colon of a male adult with cancer, with a mutation in the Ras proto-oncogene (www.ATCC.org).

HCT116 cells were maintained in *Dulbecco's Modified Eagle Medium* (DMEM) supplemented with 10% (v/v) of Fetal Bovine Serum (FBS) and 1% (v/v) Penicillin/Streptomycin solution in an CO_2 incubator at 37°C with a humidified atmosphere of 5% (v/v) CO_2 and 99% of relative humidity. HCT116 cells were seeded in a 25cm^3 T-Flask until 80-90% of cell confluence. Once this percentage of confluence was reached, a subculture was prepared on a new T-Flask to ensure the exponential growth in a monolayer culture. Hence, the culture medium was collected, and cells were washed with 2 mL of PBS 1x to remove trypsin inhibitors. After washing cells, 2 mL of TrypLE™ Express were added to detach the cells. Trypsin acted for 5 minutes and then 2 mL of DMEM medium were added to inhibit its activity. Cells were collected into microtubes and centrifuged at 500xg for 5 minutes. The supernatant was removed, and the cellular pellet was resuspended in 1 mL of DMEM medium. In a hemacytometer and with the bright field inverted microscope, Trypan Blue 0.4 % (v/v) exclusion method was performed to count viable cells per unit volume of the cellular suspension. Based on the number of counted cells calculated by the **Equation 6**, a volume of cells' suspension corresponding to 0.75 x 10^4 cells/mL was added to a new T-Flask.

Equation 6.

$$Cell\ density\ (cell/mL) = \frac{Total\ cells\ counted}{Number\ of\ squares} \times chamber\ volume\ \times dilution\ factor$$

Mycoplasma analyses were performed weekly through Polymerase Chain Reaction (PCR) detection by members of the laboratory (Daniela Ferreira) to ensure there was no cell contaminations.

2.6 Gold nanoparticles incubation in HCT116 cells

All assays performed with HCT116 cells incubated with gold nanoconjugates followed the same initial procedure described in **Figure 2.5**. HCT116 cells were plated in a 96- or 24-well plate with DMEM medium (containing phenol red pH indicator). 24 hours after the seeding, culture mediums were collected and replaced by a 2.5 nM AuNPs solution (AuNP@PEG-COOH and AuNP@PEG@Anti-Hexokinase I) diluted in the DMEM culture medium. HCT116 were exposed to AuNPs for 24 hours.

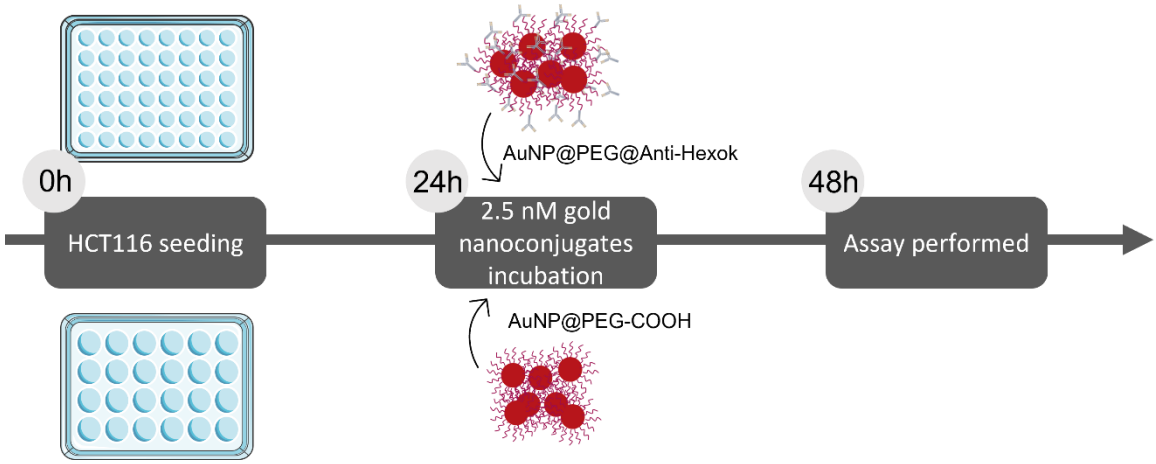

Figure 2.5 Schematic representation of the protocol for incubating gold nanoparticles in HCT116 cells. HCT116 were plated at a desired density and 24h later 2.5 nM of gold nanoconjugates were added. The HCT116 incubation with these nanoconjugates occurred for 24h. After that, the assays were carried out.

2.7 Evaluation of AuNPs internalization by HCT116 cells

2.7.1 Samples Preparation

2.7.1.1 Protein extraction

HCT116 cells were seeded in a 75cm^2 T-flask at a density of 5 x 10^5 cells/mL over 72h. Cells were washed twice with PBS 1x, dislodged from the flask by scraping and centrifuged at 500xg for 5 minutes at 4°C. Pellet was resuspended in PBS 1x for an additional wash and centrifuged again at 700xg for 5 minutes at 4°C. The supernatant was removed, and the pellet was resuspended in ice-cold lysis buffer supplemented with 0.1% DTT, 0.4% Nonidet P-40, 1mM PMSF, 1x phosphatase inhibitors and 1x protease inhibitors. The sample was stored overnight at -80°C. In the following day, the sample was exposed to 6 ultrasound pulses lasting 60 seconds with 30 seconds pause between them in the ultrasonic bath. Then, the solution was centrifuged at 5 000xg for 5 minutes at 4°C. The supernatant was collected, and the pellet was resuspended in MiliQ Water. The supernatant, which corresponds to proteins of the cytosol, and the pellet, which mainly corresponds to organelles and cellular membranes, were stored at -80°C until further utilization.

2.7.1.2 Cell fraction extraction

The *Cell Fractionation Kit* was used to obtain cellular fractions of HCT116 cells, more concretely, cytosolic, mitochondrial, and nuclear fractions. This protocol was performed after HCT116 cells were incubated with AuNPs and with HCT116 cells without any treatment, following the protocol described in section 2.6, with slight modifications: HCT116 cells were seeding in a 96-well plate at a density of 2 x 10^5 cell/mL for 72h, followed by AuNPs incubation. After that, cell mediums were collected, cells were washed with PBS 1x and trypsinized with 100 µL of Trypsin for 5 minutes. 100 µL of DMEM medium was added to each well to inhibit the trypsin activity. Cells were collected by 5 minutes of centrifugation at 5 000xg at RT. Cytosolic, mitochondrial, and nuclear fractions were obtained by sequential centrifugations in specific buffers provided by the kit, following the protocol. The resulting fractions were stored at -80°C until their utilization. Quantification of total protein was performed by Pierce assay (section 2.7.1.3).

2.7.1.3 Protein quantification by Pierce Assay

Protein samples concentrations were quantified by the Pierce ™ 660 nm Protein Assay. In acidic conditions, a reddish-brown dye-metal complex binds to positively charged amino acid groups in proteins and consequently, the dye is deprotonated and changes its colour to green. The deprotonated form has an absorption maximum at 660 nm.

In a 96 well-plate, all samples were diluted 10x with MiliQ water and incubated with 150 µL of the Pierce reagent for 5 minutes in the dark. Absorbances were measured at 660 nm on the microplate reader. A calibration curve was performed with known concentrations of BSA solutions, between 125–1000 µg/mL (see **Figure 4.4** in appendix).

2.7.2 Inductively Coupled Plasma Atomic Emission Spectroscopy (ICP-AES)

Inductively coupled plasma atomic emission spectroscopy (ICP-AES) is a spectrometric method where the emission of light released from excited atoms of an element is measured. It allows to identify and quantify chemical elements through the Beer Lamber's Law using a calibration curve performed with the chemical element for analysis [115].

ICP-AES was performed to quantify the amount of gold internalized by HCT116 cells and their intracellular localization. Since plasma-ionized gold emits radiation at 242 nm and there are not interferences from other elements in cell culture, gold quantification is possible with quite accuracy [115]. This essay was carried out with fractionated cells (cytoplasmatic, mitochondrial and nuclear fractions of HCT116 cells) allowing to simultaneously infer the total of gold in the cellular fraction (all fractions together) and also in each fraction, and then, give some information about the intracellular location of AuNPs.

HCT116 cells seeding and AuNPs incubation were performed as described in section 2.6 (24-well plate, 2 x 10^5 cell/mL). After the AuNPs' incubation time, culture mediums and washing mediums were

collected and stored in a 5 mL falcon tube for the ICP-AES analysis. Cells were washed twice with PBS and then trypsinized. When detached, cells were centrifuged at 300xg for 5 minutes. The supernatant was collected and added to the “culture and washing mediums” tube that was stored at 4°C. After centrifugation, the cell fraction protocol was performed as described in section 2.7.1.2. Cytosolic, mitochondrial, and nuclear fractions were stored at -20°C until the day of Acqua Regia preparation.

Fresh Acqua Regia was prepared, and 1 mL was added to experimental sample tubes. A calibration curve (with known gold concentrations) for each condition and the ICP-AES analysis of samples were performed as a service (*Laboratório de Análises at FCT-NOVA www.laqv.requimte.pt)*.

2.7.3 Darkfield Microscopy

Darkfield Microscopy is a light microscopy where samples are obliquely illuminated due to the presence of a dark-field ring between the white light source and the condenser. Diffracted, scattered, and refracted light are collected by the microscope and a bright image with a dark background is visualized. Indeed, darkfield microscopy allows to visualized gold nanoparticles due to their intrinsically ability to scattering light, due to the LSPR effect [116].

In this work, dark field microscopy was used to track gold nanoparticles in fixed HCT116 cells. HCT116 cells seeding and AuNPs incubation were performed as described in section 2.6 with slight modifications: HCT116 cells were seeded in a 24-well plate over coverslips at a density of 2 x 10^5 cell/mL. After AuNPs incubation, cell mediums were aspirated and cells were washed three times with PBS 1x. Cells were then fixed with 4% paraformaldehyde and washed with PBS 1x (x3). Coverslips were mounted on a slide and visualized by darkfield microscopy, using the inverted Ti-U Eclipse microscope with a Darkfield condenser. Images were collected by 100x objective lens and analysed using the Image J software.

2.8 Mitochondrial targeting and co-localization of AuNPs in HCT116 cells

2.8.1 Dot blot

Dot blot is a non-electrophoresis technique used to identify proteins in a sample, based on the immunodetection principle: antigen-antibody recognition. In this work, dot blot was performed with the purpose of evaluating the recognition of the Hexokinase I protein, expressed in the outer mitochondrial membrane, by the Anti-Hexokinase I functionalized on gold nanoparticles’ surfaces. Therefore, protein samples obtained by the protein extraction protocol described in section 2.7.1.1 (organelle and membranes fraction) and by the cellular fraction protocol (mitochondrial fraction) described in section 2.7.1.2 were tested. This analysis took advantage of the red colour of gold nanoparticles visible to the naked eye [117].

Small nitrocellulose membranes were incubated with 2.5 µg of protein samples and allowed to dry at RT. Then, membranes were incubated with AuNP@PEG-COOH or AuNP@PEG@Anti-Hexokinase I for 1 hour at RT under agitation. Membranes were washed with TBST 1x (50mM Tris, 150mM NaCl and 0.1%(v/v) Tween 20, pH7.5) (**Figure 2.6**). Additionally, membranes incubated only with AuNPs were used as controls to analyse the adsorption behaviour of gold nanoparticles at the membrane without previously protein incubation. The binding between the antibody functionalized on gold nanoparticles to protein adsorbed on the membrane was evaluated by the intensity of the red colour, measured using Image J software tools. To facilitate the analysis, the colour of the images was inverted.

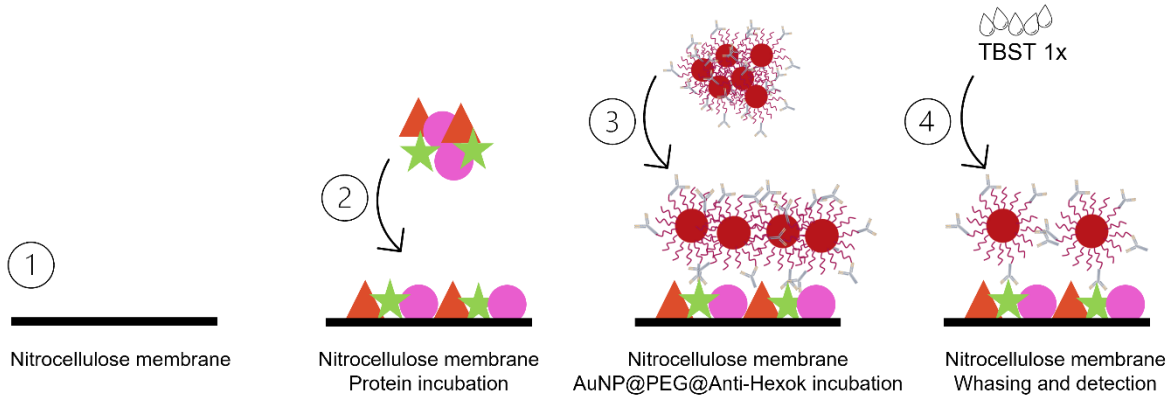

Figure 2.6 Schematic representation of the Dot Blot protocol performed with AuNP@PEG@Anti-Hexokinase I. Nitrocellulose membranes where incubated with 2.5 µg of protein and then with AuNP@PEG@Anti-Hexokinase I solution. This assay aimed to evaluate the recognition between the Anti-Hexokinase I functionalized on gold nanoparticles and its target protein present in solutions.

2.8.2 Western Blot

Western Blot is an analytical technique that allows identifying specific proteins in a sample. The detergent sodium dodecyl sulfate (SDS) binds to proteins in a constant molar ratio, assigning an equal negative charge between proteins in the sample and allowing them to be separated according to their molecular weight. A reducing agent is also used to cleave disulfide bonds, which imparts linearity to the proteins. Specific proteins are detected by the immunodetection principle, through specific antibodies. Hence, Western Blot have five main steps: i) Samples preparation; ii) Running; iii) Transference; iv) Primary and secondary antibodies incubation and v) Protein detection.

In this work, western blot was used as an indirect method to assess the internalization and localization of AuNP@PEG@Anti-Hexokinase I after their incubation in HCT116 cells (under the conditions described in section 2.6). The assay was performed using cellular fractions (cytoplasmatic, mitochondrial and nuclear) obtained after cells incubation with AuNPs, as described in section 2.7.1.2. Cellular fractions obtained by cells without any AuNP incubation were used as controls.

8% of acrylamide-bisacrylamide gels (**Table 2.1**) were prepared and a volume corresponding to 4 µg of protein from fraction samples was loaded and ran at 120 V for approximately 1h30 minutes. Before this, sample preparations were performed according to the protocol of Cell Fraction Kit, with an appropriate SDS Sample Buffer. The transfer was performed with a nitrocellulose membrane in a semi-

dry transfer system and ran at 130 mA for 1 hour. The semi-transfer system was mounted as represented in **Figure 4.5** and **Table 4.1** (in appendix). The transfer efficiency was observed by staining the nitrocellulose membrane with Ponceau S solution and the acrylamide-bisacrylamide gel with Coomassie Blue dye.

Table 2.1 Solutions for preparing the 8% resolving gel and 5% stacking gel.

	Resolving Gel (8%)	Stacking gel (5%)
MiliQ-Water	5.5 mL	3.4 mL
Acrylamide / Bisacrylamide (40x)	2 mL	380 µL
Resolving / Stacking Buffer 4x	2.5 mL	630 µL
SDS 20%	25 µL	25 µL
10% APS (Ammonium persulfate)	100 µL	50 µL
TEMED	10 µL	6 µL

Nitrocellulose membranes were blocked with 5% BSA (w/v) in TBST 1x for 2h at RT, under agitation. Then, firstly, membrane was incubated only with the secondary antibody, Anti-Rabbit IgG HPR-Linked antibody in 5% Milk (w/v) in TBST (1:2000) for 1h, under agitation.

Protein bands were developed using the WesternBright ECL substrate, a chemiluminescent HRP substrate. It was added and incubated under membranes for 5 minutes at RT. In the darkroom, the film was exposed to the membrane and bands were revealed and fixed with appropriate solutions.

After the development of membranes incubated only with the secondary antibody, they were incubated with stripping buffer (Gly 0.1M, Magnesium acetate 20 mM, KCl 50 mM, pH=2) to remove antibodies binding. Membranes were then blocked once more with 5% BSA (w/v) in TBST 1x and subsequently incubated with the primary antibody Anti-Hexokinase I in 5% BSA in TBST 1x (1:1000) overnight at 4°C. After the primary antibody incubation, the membrane was washed three times with TBST 1x, 5 minutes each, and then incubated with the secondary antibody as described above. Membrane development followed the same procedures as previously described.

2.8.3 Immunofluorescence assay

To evaluate the intracellular targeting of AuNP@PEG@Anti-Hexokinase I, an immunofluorescence assay (IFA) was performed. IFA uses specific antibodies with fluorescent dyes to identify specific antigens in a sample. Here, HCT116 cells after AuNP@PEG@Anti-Hexokinase I incubation were fixed and AuNP@PEG@Anti-Hexokinase I, mitochondria, and nucleus were labelled and visualized by fluorescence microscopy.

HCT116 were seeded at a density of 2 x 10^3 cell/mL in a 96-well plate and 24 hours after cells were incubated with the CellLight™ Mitochondria-GFP. It was used to label cell mitochondria through a transfection system that induced the expression of Green Fluorescent Protein (GFP) in the mitochondria membrane. 24 hours after, cell culture mediums were collected, and cells were incubated with AuNPs

as described in section 2.7.1.2. Then, cell media was aspirated, and cells were fixed with 4% (v/v) paraformaldehyde in PBS 1x solution for 20 min at RT. Cells were washed three times with PBS 1x, incubated with 0.1% Triton-X 100 for 10 min at RT to permeabilized and washed again with PBS 1x. Before staining with antibodies, cells were blocked with 1% of BSA prepared with filtrated PBS 1x, to avoid nonspecific binding. A secondary antibody against Anti-hexokinase I was used to identify the AuNP@PEG@Anti-Hexokinase I nanoconjugate. Therefore, cells were incubated with the secondary antibody Goat anti-rabbit IgG (TRITC) (1:1000) for 1 hour at RT. Tetramethylrhodamine (TRITC) emits orange fluorescent, once it has excitation at 547 nm and emission at 572 nm. After secondary antibody incubation, cells were washed again three times with PBS 1x. Cell nuclei were stained with Hoechst 33258 dye, which emits blue fluorescence when bound to the DNA (excitation at 352 nm and emission at 461 nm). After the staining steps, fluorescence images were collected using an inverted Ti-U Eclipse microscope. Images of the nucleus were acquired with the 4′,6-diamidino-2-phenylindole (DAPI) filter (excitation at 360/40 nm in the UV region and emission at 460/50 nm in the blue region), of mitochondria with the Fluorescein isothiocyanate (FITC) filter (excitation at 480/30 nm in the red region and emission at 535/40 nm in the green region) and images of the staining with Anti-Rabbit TRITC were collected with the G2A filter (excitation at 535/50 nm in the green region and emission at > 590 nm). Fluorescence images were treated using the Image J software.

2.9 Therapeutic effect of the nanoconjugates- Hyperthermia

2.9.1 Irradiation of cells

HCT116 were seeding and AuNPs were incubated as described in section 2.6 (96-well plate, 2 x 10^5 cell/mL). After AuNPs' incubation, culture mediums were collected, cells were washed three times with PBS 1x and 100 µL of supplemented DMEM medium without phenol red pH indicator was added. Then, each well was irradiated with a continuous wave 532 nm green diode-pumped solid-state laser coupled to an optical fibre with a intensity of 2.37 $W.cm^{-2}$ for 60s. This laser intensity and duration were chosen for the first laser experiment, as it was previously tested in the lab by Daniela Ferreira (PhD student personal communication) and Pedro Pedrosa [118] and no lethal effects were observed. Therefore, as this work aimed to target mitochondria of cells and then studied the effect of localized intracellular hyperthermia, cellular damages could be expected to be observed using this laser setup. The temperature of culture medium was measured in each well before and immediately after laser irradiation using a thermocouple. Cell viability was evaluated by MTS and Trypan Blue assay.

2.9.2 Cell viability

2.9.2.1 MTS Assay

MTS is a colorimetric assay used to quantify metabolically active cells, once metabolically active cells can reduce the MTS Tetrazolium reagent to Formazan, a soluble coloured compound with a high molar extinction coefficient at a wavelength of 490 nm. The reaction is carried out by NAD(P)H-dependent dehydrogenase and, thus, depends on the levels of NAD(P)H in cells [119]. Therefore, cell viability can be correlated with the quantity of Formazan production. Thus, if a reduction in cell viability

is observed, the absorbance value at 490 nm is expected to decrease. This assay was performed to evaluate the cytotoxicity effect of gold nanoconjugates against HCT116 cells and their PTT effect after irradiation.

To perform the assay, HCT116 were seeding and AuNPs were incubated as described in section 2.6 (96-well plate, 2 x 10^5 cell/mL). After the incubation time with nanoconjugates (and the hyperthermia assay), cell culture mediums were collected and replaced by the MTS reagent (CellTiter 96® AQ_{ueous} Non-Radioactive Cell Proliferation reagent), diluted in DMEM medium (80 µL of DMEM medium + 20 µL of MTS reagent) for 30 minutes, away from light in a 37°C incubator. Then, absorbance at 490 nm was measured on the microplate reader. Cell viability was calculated by subtracting the black from all experiments and dividing it by the control of the experiment (**Equation 7**).

Equation 7. $$Cell\ viability\ (\%) = \frac{A_{490}(HCT116+nanoconjugates) - A_{490}(nanoconjugates)}{A_{490}(HCT116) - A_{490}(culture\ medium)} \times 100$$

2.9.2.2 Trypan Blue counting

Cell viability can also be assessed by the Trypan Blue exclusion assay. Trypan blue is a hydrophilic dye that cannot cross the cellular membrane of cells. If the cell membrane is disrupted, it can enter cells and blue colour in the cell's cytoplasm is observed [120].

To perfume the assay, HCT116 cells were seeded and treated in the same conditions mentioned in the MTS assay (section 2.9.2.1). After the incubation time with nanoconjugates (and the hyperthermia assay), cells were trypsinized adding 70 µL of Trypsin. Then, Trypan Blue dye was added in the proportion of 1:1. Total cells and blue cells were counted with the Hemacytometer as previously described. Cell viability was calculated according to the **Equation 8**.

Equation 8. $$Viable\ cells\ (\%) = \frac{Viable\ cells}{Total\ cells}\ x\ 100$$

2.10 Statistical analysis

Statistical analysis were performed using the GraphPad Prism 8.0.1 (GraphPad Software, Inc). Mann-Whitney tests were used to measure the tendency of two groups derived from the same population. A significant threshold of 0.05 was used for all analysis.

3

RESULTS AND DISCUSSION

3.1 Gold nanoparticles synthesis, functionalization, and characterization

Spheric gold nanoparticles stabilized by citrate molecules have a characteristic red colour due to the SPR effect (see section 1.3.3), therefore the success of their synthesis by the citrate reduction method was visually observed by the colour change of the reactional solution from yellow to red (**Figure 2.1**). Gold nanoparticles stabilized by citrate molecules (AuNP@Citrate), pegylated (AuNP@PEG-COOH) and functionalized with Anti-Hexokinase I (AuNP@PEG@Anti-Hexok I) (**Figure 2.4**) were characterized by UV-Visible spectroscopy, DLS and Zeta Potential. The size of gold nanoparticles synthesised by the citrate reduction method is mainly dependent on the trisodium citrate concentration added to the reaction [109][121][122]. Therefore, as expected, the diameter calculated by UV-Visible spectroscopy for the synthetised AuNP@Citrate was 14 nm. Moreover, since the SPR peak of gold nanoparticles is also dependent on their size, and as expected for 14 nm spheric gold nanoparticles [123], the SPR peak of AuNP@Citrate was at 520 nm (**Figure 3.2** and **Figure 3.1**). DLS revealed an average hydrodynamic size of ≈17 nm (**Figure 3.3**) and Zeta Potential measurement revealed a negative superficial charge of -49.1 $\pm$ 2.4 mV (**Table 3.1**). As expected, hydrodynamic size is higher than the size calculated by UV-Visible spectroscopy, since i) DLS measures not only the diameter of the core but also the hydrated layer around AuNPs in solution and ii) DLS value represents the size distribution of AuNPs in solution. Zeta potential value agrees with the expected due to the capping of AuNPs with negative citrate ions ($C_3H_5O(COO)_3^{3-}$).

The SPR of AuNPs is affected by surface modifications with dielectric materials, such as PEG molecules or antibodies [123][124]. Therefore, the functionalization steps of gold nanoparticles could be followed by observing the SPR peak shifts in the UV-Visible spectra. As **Figure 3.1** and **Figure 3.2** show, a redshift occurred in the UV-Visible spectrum along the consequent functionalization steps: The pegylation of AuNPs (AuNP@PEG-COOH) caused a redshift of 1 nm in the SPR wavelength and the functionalization with Anti-Hexokinase I (AuNP@PEG@Anti-Hexok I) caused a 7 nm redshift.

Assuming that HS-PEG(8)-COOH has a length of 3.25 nm and that it was fully stretched in the AuNP surface, an maximum increase of 6.5 nm in hydrodynamic size was expected for AuNP@PEG-COOH with only one PEG layer. DLS analysis showed that hydrodynamic size of AuNPs after pegylation increased to ≈21 nm (**Figure 3.3** and **Table 3.2**). The Zeta potential of AuNP@PEG-COOH remained negative (-51.7 ± 5.2 mV) due to the negative charge of the carboxylic groups at pH 7 [125].

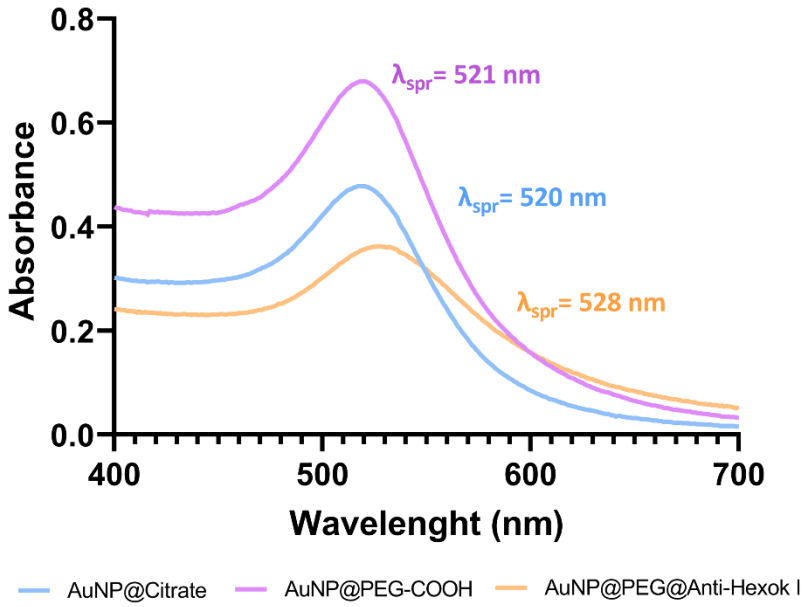

Figure 3.1 UV-Visible spectrum of each gold nanoparticle solution with identification of the surface plasmon resonance peak (λ_{SPR}). A redshift was observed between the different functionalization steps of AuNPs. Each measurement was performed three-times.

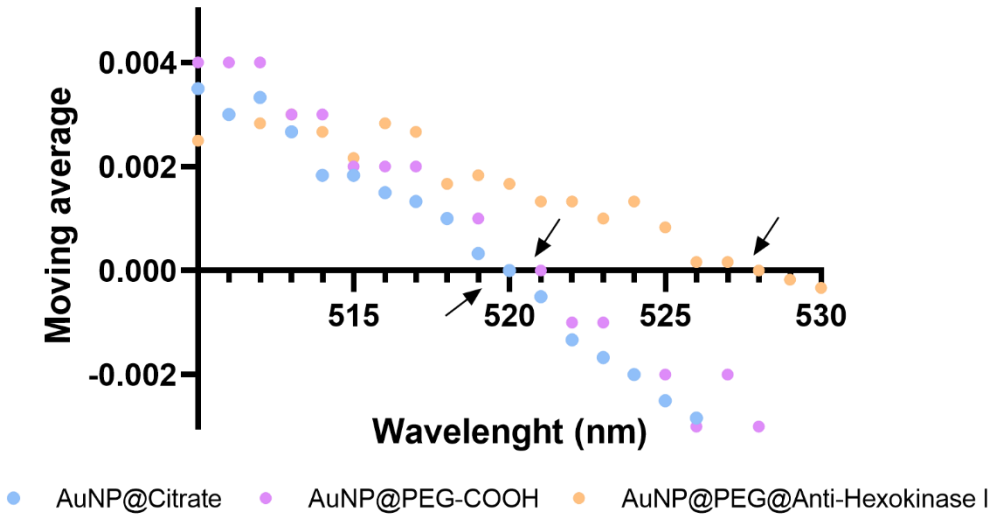

Figure 3.2 Moving average of UV-Visible spectroscopy absorbance values. The x-axis intersection (indicated by the arrows) corresponds to the SPR wavelength of each nanoconjugate

Since, AuNP@PEG-COOH were stored as a stock solution, they were recharacterized before use to ensure stability. Indeed, some DLS analyses of AuNP@PEG-COOH solution showed a higher hydrodynamic size (for example, 36 nm) with a higher polydisperse index (Pdi = 0.4), denoting that some aggregates were formed during the storage time [108]. In these cases, AuNPs were sonicated before utilization during 10-15 minutes at RT, using the ultrasonic bath.

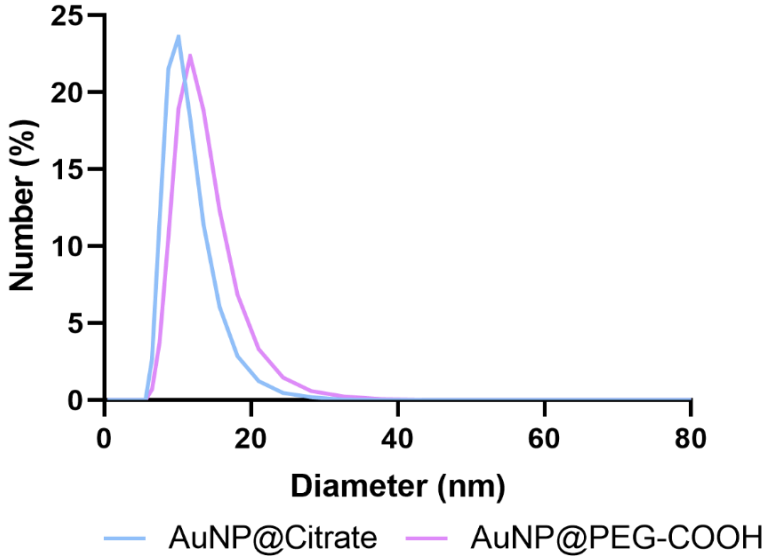

Figure 3.3 DLS analysis of AuNP@Citrate and AuNP@PEG-COOH. An increase in the hydrodynamic radium of AuNPs was observed after pegylation**.**

Table 3.1 Zeta Potential values of AuNP@Citrate and AuNP@PEG-COOH. AuNP@Citrate had a negative zeta value due to the citrate caping, as well as AuNP@PEG-COOH, due to the negative charge of carboxylic group.

	Zeta Potential (mV)	Std. Dev
AuNP@Citrate	-49.2	2.4
AuNP@PEG-COOH	-49.1	1.3

The yield of AuNPs pegylation was evaluated by the Ellman's assay, which revealed that only 3% of HS-PEG(8)-COOH remained at the supernatant of the reaction, suggesting that the remaining PEG molecules stayed in the AuNPs fraction, ideally, functionalized to the surface, which would mean 100% functionalization. As mentioned in section 1.3.3, pegylation of gold nanoparticles is an important step since it prevents immunological recognition, improves their retention time in blood and prevents aggregation. Furthermore, a bi-functional PEG with a carboxylic group was chosen to facilitate the conjugation with anti-Hexokinase I. In this way, AuNPs with 100% surface covered by HS-PEG(8)-COOH was crucial to improve the yield of antibody functionalization, since the number of carboxylic groups able to react was the maximum.

For the antibody functionalization step by the EDC/NHS reaction, some calculations were performed to estimate how many antibodies could be functionalized on the surface of 14 nm gold nanoparticles.

These calculations suggested that in optimal conditions (assuming that antibodies bind to nanoparticles via the C-terminal and not considering repulsive forces between them), a maximum of 11 antibodies could be functionalized on the surface of 14 nm gold nanoparticles (see **Figure 4.6** in appendix). Therefore, based on these calculations and due to some limitations associated with the low concentration of the commercial antibody stock solution, the reaction was performed to achieve 5 antibodies per AuNP. After the EDC/NHS reaction, Bradford assay revealed a functionalization efficiency of 34.5 %, corresponding to approximately 2 antibodies per AuNP. However, some limitations in this assessment might exist as the Anti-Hexokinase I antibody original solution is stored in 40% of glycerol and the final percentage of glycerol that is compatible with Bradford assay is 5%. Due to the high volume of antibody solution added to the reaction mix (to ensure the predicted number of antibody moles), the percentage of glycerol in the final mixture may have been higher than that value. Gold nanoparticles present in the supernatant solution may have also affect the Bradford assay since they absorb light in the same wavelength of Bradford reagent (595 nm) (see **Figure 3.2**), however, to reduce this interference, supernatants were centrifugated before the assay.

Altogether, these analyses show that gold nanoparticle modifications have occurred along the different functionalization steps and thus allowed to infer that three types of gold nanoparticles were obtained and were able to be used: i) 14 nm AuNP@Citrate; ii) AuNP@PEG-COOH (100% covered) and iii) AuNP@PEG@Anti-Hexokinase I with ≈ 2 antibodies per AuNP. Moreover, an increse in the agregation index were observed along the functionalization steps (**Table 3.2**).

DLS and Zeta Potential of AuNP@PEG@Anti-Hexokinase I were not measured due to the low concentration of solutions. Throughout the thesis, different batches of AuNP@PEG-COOH and AuNP@PEG@Anti-Hexokinase I were functionalized, and their characterization was similar. **Table 3.2** summarize the characterization results of the different nanoconjugates. Complementary techniques, such as Transmission electron microscopy (TEM) could also be performed to characterize the distribution size of AuNPs, as well as follow their surface modification [126].

Table 3.2 Compilation of gold nanoconjugates characterization results

	AuNP@Citrate	**AuNP@PEG-COOH**	**AuNP@PEG@Anti-Hexok I**
λ_{SPR} (nm)	520	521	528
Hydrodynamic size (nm)	17	21	ND
Polydispersity Index	0.21	0.15	ND
Zeta potential (mV)	-49.2	-51.7	ND
Agregation index	0.25	0.32	0.54

3.2 Uptake of Gold nanoconjugates (AuNP@PEG-COOH and AuNP@PEG@Anti-Hexokinase I) by HCT116 cells

Gold nanoparticles (AuNP@PEG-COOH and AuNP@PEG@Anti-Hexokinase I) internalized by HCT116 cells were quantified via UV-Visible spectroscopy and ICP-AES, and visualized by Darkfield microscopy.

The quantification of AuNPs in the culture medium collected after the incubation step by UV-Visible spectrophotometry revealed that 43% of AuNP@PEG-COOH and 46% of AuNP@PEG@Anti-Hexokinase I were retained in the cellular fraction (**Figure 3.4**). This means that these percentages of gold nanoparticles may have been internalized by cells, adhered to the cellular membrane or co-precipitated with cells.

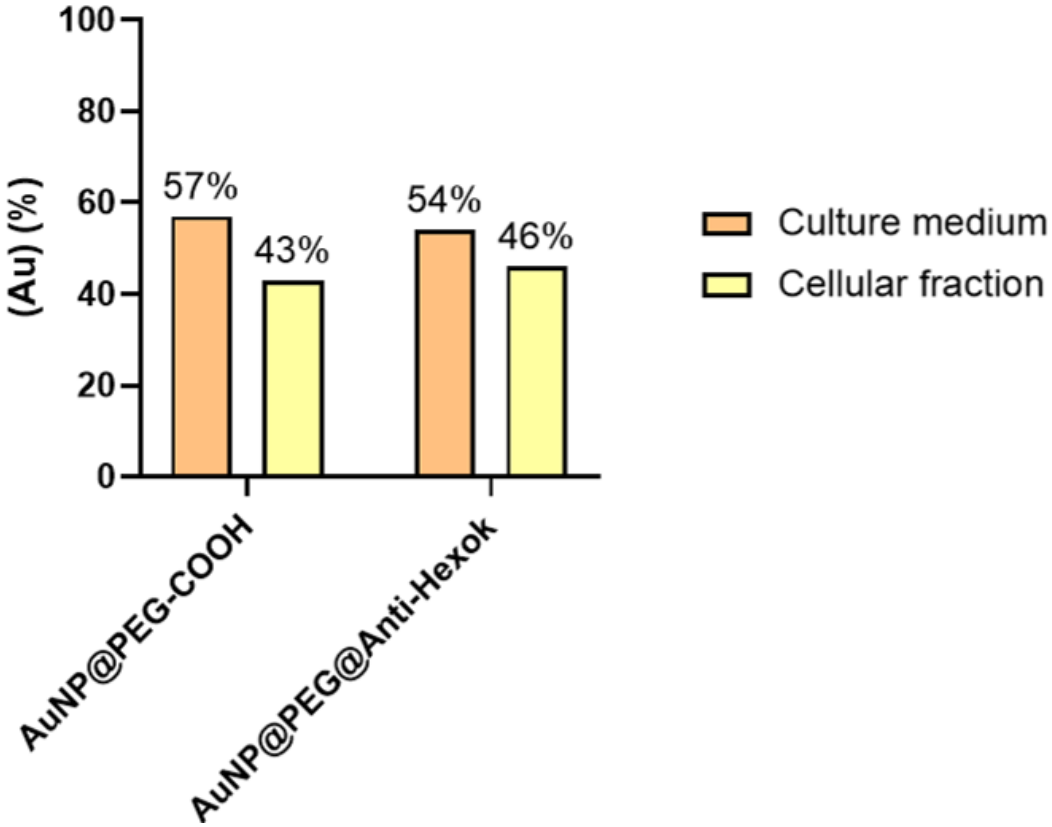

Figure 3.4 Percentage of gold (Au) in the culture medium and cellular fraction after 24h of incubation calculated by UV-Visible spectroscopy. HCT116 were incubated with 2.5nM of AuNP@PEG-COOH and AuNP@PEG@Anti-Hexokinase I for 24h. After incubation time, the total AuNPs In each well were calculated by measuring the absorbance at the SPR peak and using the Beer-Lambert Law. The culture media collected were also quantified. The difference between the total gold concentration in each well and the gold concentration in the cell culture medium corresponds to the NPs concentration in the cell fraction. The assay had four technical replicates and two biological replicates.

On the other hand, when HCT116 mitochondrial, nuclear and cytoplasmatic fractions were differentially isolated, results of ICP-AES to quantify the amount of gold were different. When HCT116 were incubated with AuNP@PEG-COOH no gold was detected in the cellular fractions. However, when HCT116 cells were incubated with AuNP@PEG@Anti-Hexokinase I, 14% of gold was detected in the

nuclear fraction and a residual amount of gold (2%) was detected in the mitochondrial fraction (**Figure 3.5**). Although the percentage of AuNP@PEG@Anti-Hexokinase I detected in the mitochondrial fraction is low, it is higher compared with the cytoplasmatic fraction evidencing some targeting specificity. When it respects to the amount of AuNP@PEG@Anti-Hexokinase I identified in the nuclear fraction (**Figure 3.5**) some explanations might be drawn: i) AuNP@PEG@Anti-Hexokinase I recognized and bound to the Hexokinase I expressed in the mitochondrial outer membrane and consequently, the mitochondrial density increased, which caused them to be collected in the last fraction; ii) AuNP@PEG@Anti-Hexokinase I were adsorbed non-specifically to cellular membranes and thus, since cellular membranes are dense, they are collected in the nuclear fraction; iii) denser aggregates of nanoparticles precipitate in the last fraction collected.

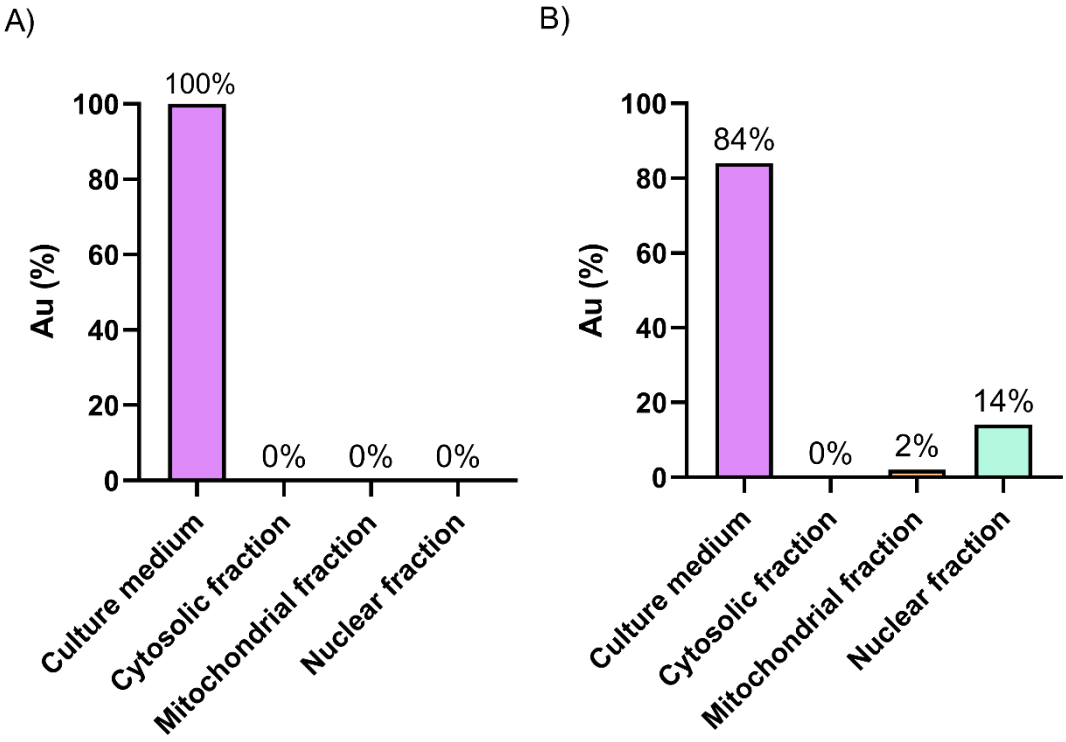

Figure 3.5 Percentage of gold calculated by ICP-AES in HCT116 fractions incubated with AuNP@PEG-COOH (A) and AuNP@PEG@Anti-Hexokinase I (B). HCT116 were incubated with 2.5nM of AuNP@PEG-COOH and AuNP@PEG@Anti-Hexokinase I for 24h. After incubation time, HCT116 cells was fractionated and gold concentration were measured in each resulting fraction (cytosolic, Mitochondrial and Nuclear), as well as culture media, by ICP-AES. This assay was performed once, without technical and biological replicates.

UV-Visible spectrophotometry and ICP-AES provided different results about the uptake rate of gold nanoparticles; hence, advantages and limitations of each technique need to be discussed. Quantification of gold nanoparticles by UV-Visible spectrophotometry uses their extinction coefficient, and as discussed previously, it depends on several factors, including their size [127]. As determined in section 3.1, sizes of gold nanoconjugates (AuNP@PEG-COOH and AuNP@PEG@Anti-Hexokinase I) were different, however, the same extinction coefficient was used for the calculations of gold nanoconjugates concentration (ε=2.33 x 10^8 $M.cm^{-1}$), having an associated miscalculation. On the other

hand, ICP-AES calculations use calibration curves performed with the same samples to be analysed and with known gold concentrations. Although ICP-AES has a considerable sensitivity in the order of ppm (parts per million) [128], the range of calibration curves used to calculate the concentration of gold might not be suitable and, consequently, the amount of gold measured was not accurate. Moreover, the cell fraction extraction protocol (see section 2.7.1.2) includes successive high-speed centrifugations (5 000 and 10 000 x g), which may have lead nanoparticles precipitated in a different fraction than they were prior to cells fractionation. Due to limitations of both techniques and experimental errors that could also be associated, it is difficult to speculate what the real result is. Even so, these results may be the

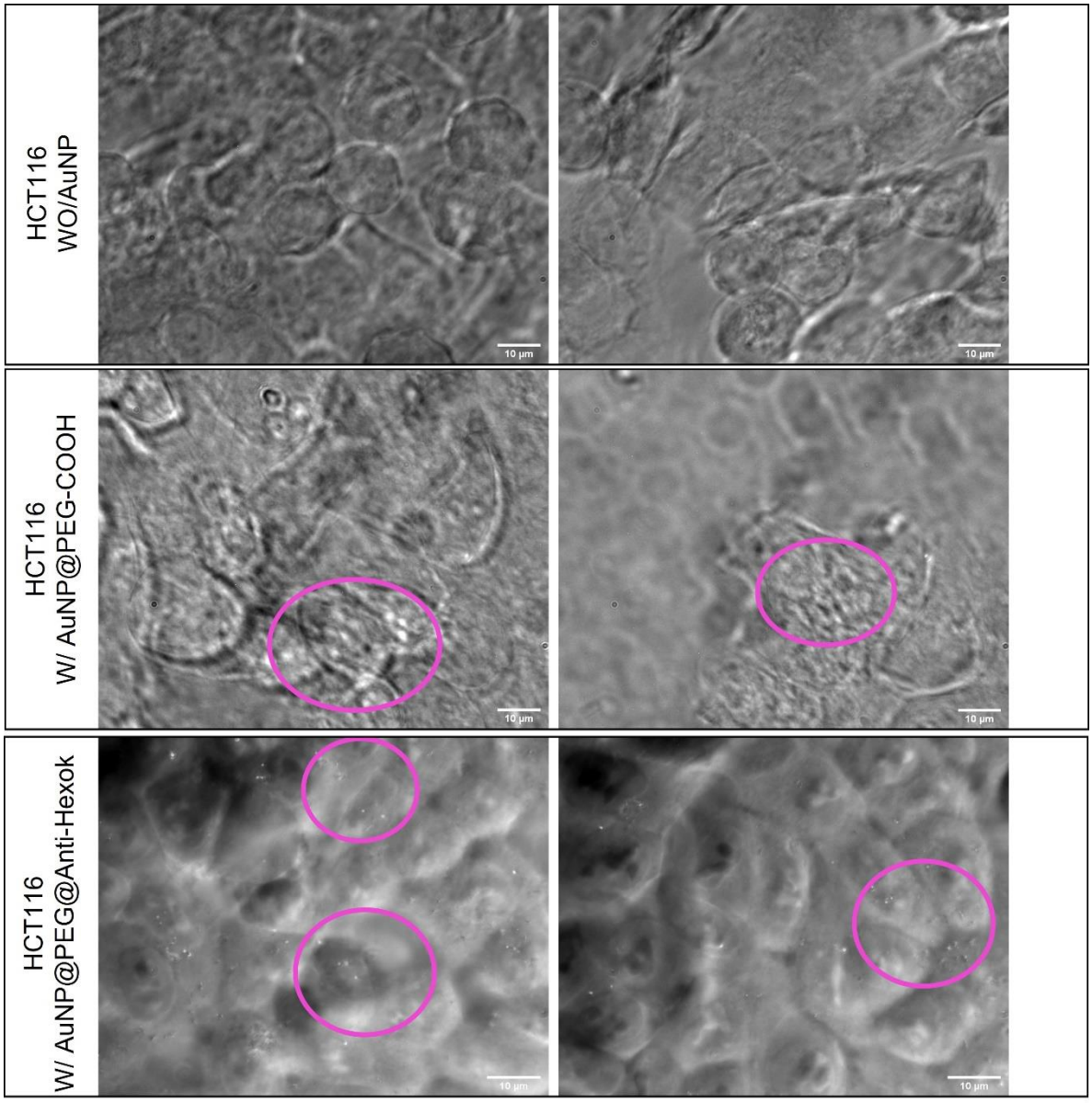

Figure 3.6 Dark Field images of fixed HCT116 cells without any treatment, after 24h of AuNP@PEG-COOH incubation and 24h of AuNP@PEG@Anti-Hexokinase I incubation. AuNPs are visualized as bright dots due to their light scattering ability, highlighted by the purple circles. Scale bars represent 10 µm.

first indication that nanoparticles were internalized by HCT116 cells, and AuNP@PEG@Anti-Hexokinase I may have specificity to the mitochondrial fraction.

Once gold nanoparticles scatter light due to the SPR effect, they are visualized as bright dots by Dark Field microcopy [96]. In **Figure 3.6** is possible to identify these bright dots in the fixed HCT116 cells incubated with gold nanoconjugates (AuNP@PEG-COOH and AuNP@PEG@Anti-Hexokinase I) but not in HCT116 cells without AuNPs incubation. These is another evidence that part of gold nanoconjugates (AuNP@PEG-COOH and AuNP@PEG@Anti-Hexokinase I) were internalized by HCT116 cells after 24 hours of incubation.

Although the precise quantification of the amount of each nanoconjugate internalized by HCT116 was not possible, the results seem to indicate that after 24 hour of incubation some of them are internalized. However, these experiments needed to be confirmed, specially the ICP-AES, since no technical and biological replicates were performed.

3.3 Mitochondrial targeting of AuNP@PEG@Anti-Hexokinase I

Mitochondrial targeting of AuNP@PEG@Anti-Hexokinase I was assess also by Dot blot, Western blot, and immunofluorescence.

The dot blot protocol was adapted to study the recognition of the antigenic protein “Hexokinase I” by Anti-Hexokinase I functionalized on the surface of AuNPs, based on the sandwich reaction mechanism (See **Figure 2.6**) [129]. Since colloidal gold nanoparticles solutions have a characteristic red colour, due to the SPR effect, this assay was designed to be a colourimetric assay. Thus, the specific

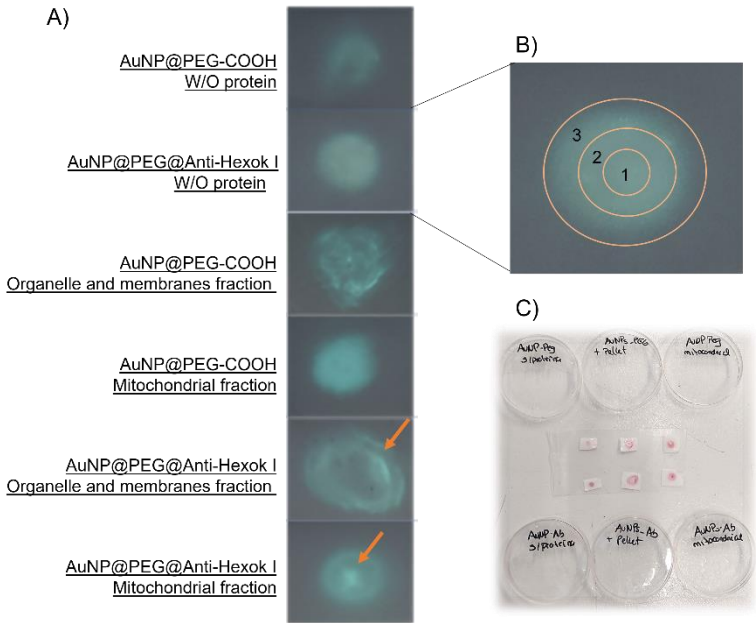

Figure 3.7 Schematic representation of the Dot Blot protocol. A) Images of nitrocellulose membranes after protein and nanoparticles incubation. The colour of images was inverted by the Image J software; B) Representation of the the circular plot divided into three annuli for quantitative analysis; C) Picture of the experimental work.

binding of AuNP@PEG@Anti-Hexokinase I to the predicted antigen would be identified by the intensity of the red colour: if a nonspecific binding occurred, it was expected that gold nanoparticles were washed away and the membrane kept white [129][130][131]. However, in the controls of nitrocellulose membrane without protein incubation, after gold nanoconjugates (AuNP@PEG-COOH and AuNP@PEG@Anti-Hexokinase I) incubation, the red colour remained on membranes after washing with PBS, denoting that gold nanoparticles adsorbed on the membrane and washings did not remove the non-specific linked nanoparticles (**Figure 3.7**). It is important to refer that nitrocellulose membranes were not blocked with BSA solution before proteins and gold nanoparticles incubation, which might have facilitated their nonspecific binding [131]. Furthermore, as nanoparticles used in this assay had a carboxylic group (AuNP@PEG-COOH) or an antibody (AuNP@PEG@Anti-Hexokinase I) on their surface, the affinity of these elements for the nitrocellulose membrane may be the reason why nanoparticles adsorbed nonspecifically. Nevertheless, it was observed that the intensity of red colour has an inconstant scattering pattern over the membranes, probably due to the different local accumulation of gold nanoparticles (**Figure 3.7**).

Dot blot analysis was performed by dividing the circular plot into three annuli **Figure 3.7 B**) and the red colour intensity was analysed and measured in each one. Annulus 1 correspond to the position where samples were dropped and once solutions are colloidal suspensions of proteins and nanoparticles, the circular flow movement of the liquid part drags their suspended content. Moreover, since mitochondria are a dense organelle, we assume that when protein solutions were deposited, they were retained in the central annuli (section 1). **Figure 3.7** and **Figure 3.8 A-C** show that AuNP@PEG-

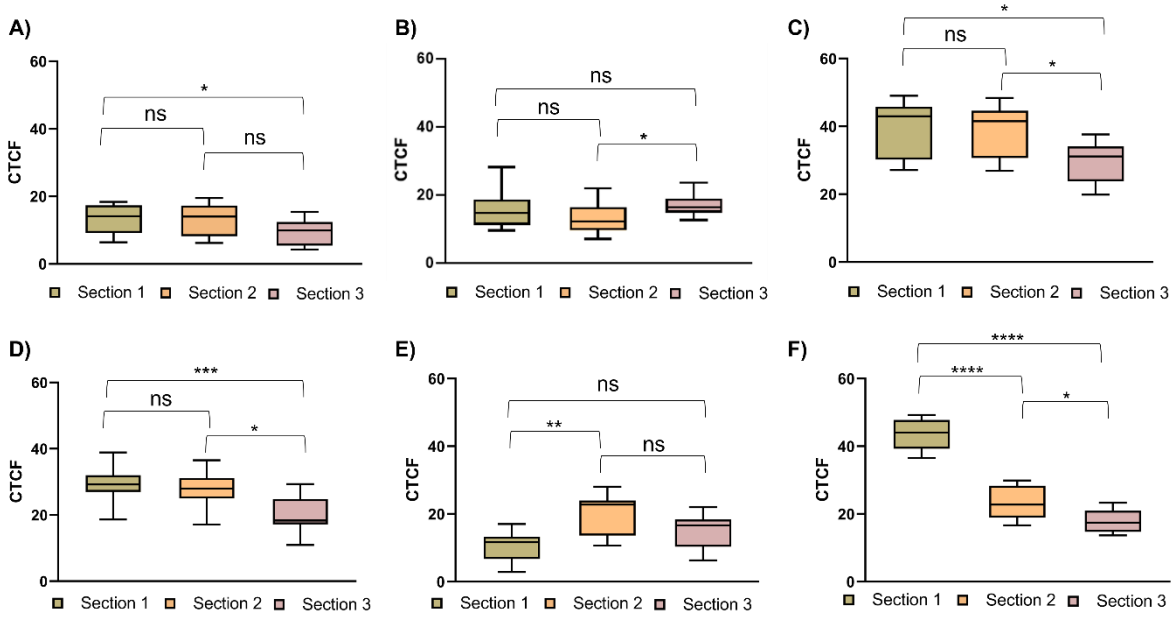

Figure 3.8 Dot blot analysis. Corrected Total Cell Fluorescence (CTCF) measurements for each annuli section. A) Membrane without protein incubated with AuNP@PEG-COOH; B) Membrane with organelle and membrane proteins incubated with AuNP@PEG-COOH; C) Membrane with mitochondrial fraction incubated with AuNP@PEG-COOH; D) Membrane without protein incubated with AuNP@PEG@Anti-Hexokinase I; e) Membrane with organelle and membrane proteins incubated with AuNP@PEG@Anti-Hexokinase I; F) Membrane with mitochondrial fraction incubated with AuNP@PEG@Anti-Hexokinase I. Analysis statistics were performed using the Mann-Whitney test. (ns- no significant differences; *P<0.05 ; ** P<0.01 ; *** P<0.001; **** P<0.0001)

COOH accumulation was uniform over the three annuli of the three test conditions and no significative differences were observed between the colour intensity among section 1 and 2. Otherwise AuNP@PEG@Anti-Hexokinase I had a non-uniform distribution patter over the membrane incubated with the mitochondrial fraction (**Figure 3.7** and **Figure 3.8 F**). Here, a high intensity of nanoparticles accumulation was visible in the section 1 compared to others. These results can be seen as an indication that gold nanoparticles functionalized with Anti-Hexokinase I recognized a protein present in the mitochondrial fraction, another evidence that AuNP@PEG@Anti-Hexokinase I may have specificity to the mitochondrial fraction.

Western Blot protocol was adapted to identify the presence of Anti-Hexokinase I (IgG molecular weight: 150 kDa) in fractionated samples (cytosolic, mitochondrial and nuclear fractions) of HCT116 cells incubated with AuNP@PEG@Anti-Hexokinase I for 24h, as well as the Hexokinase I protein (molecular weight: 102 kDa). At the same time, Western blot was performed to corroborate the results provided by the ICP-AES analysis (see section 3.2).

Firstly, nitrocellulose membranes containing the cytosolic, mitochondrial and nuclear fractions of HCT116 cells (with or without AuNP@PEG@Anti-Hexokinase I) were incubated with the secondary antibody Anti-Rabbit IgG HPR-Linked. As the membranes were previously blocked with 5% BSA solution and no primary antibody was added, the appearance of protein bands would indicate the presence of the antibody Anti-Hexokinase I. As represented in **Figure 3.9 B**, a band with molecular weight close to 100 kDa was identified in all samples resulting from HCT116 incubated with AuNP@PEG@Anti-Hexokinase I. This band is a consequence of the recognition between the secondary and the primary antibody in the surface of functionalized nanoparticles. Although the primary antibody has a molecular weight of 150 kDa, it is assumed that during the desaturation steps of protein samples, the disulfide bond between the heavy and the light chain might be broken. The two heavy chains (50 kDa each) are linked by two disulfide bonds while heavy and light chains are connected only

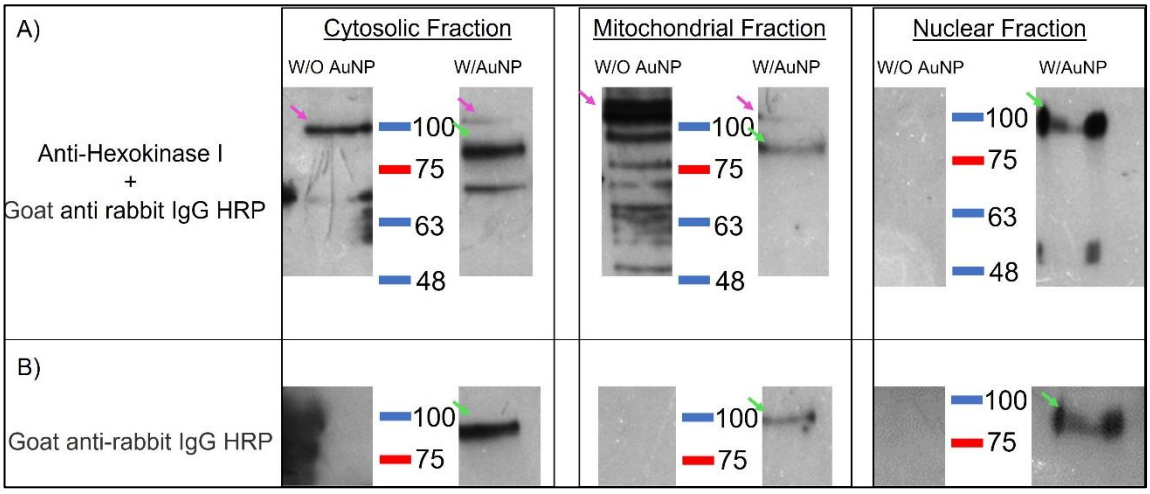

Figure 3.9 Western Blot analysis of HCT116 fractions with and without AuNP@PEG@Anti-Hexokinase I incubation. A) Nitrocellulose membrane incubated with Anti-hexokinase I followed by Goat Anti-Rabbit IgG HPR incubation; B) Nitrocellulose membrane incubated only with the secondary antibody Goat Anti-Rabbit IgG HPR. Pink arrows are indicated the 102 kDa band and green arrows the 100 kDa bands. Protein band sizes were defined using the NZYColour Protein Marker II.

by one. Hence, the band near the 100 kDa could be a dimer of Heavy-Heavy chain of the Anti-Hexokinase I (50 kDa + 50 kDa) which was recognized by the secondary antibody.

When nitrocellulose membranes were firstly incubated with the primary antibody (Anti-Hexokinase I) (followed by the incubation with the secondary antibody) the 100 kDa bands remained in the same samples previously identified. Additionally, a band with molecular wight >100 kDa appeared in the cytosolic and mitochondrial fractions samples (resulting from HCT116 cells with and without nanoparticles incubation) (**Figure 3.9 A**). Once the molecular weight of this band is close to 102 kDa and since it appeared only in cytosolic and mitochondrial fractions (the cellular regions where hexokinase I is expressed), we assume that this band corresponds to the Hexokinase I protein.

The western blot results allowed to identify the presence of Anti-Hexokinase I in fractionation samples of HCT116 previously incubated with AuNP@PEG@Anti-Hexokinase I. Anti-Hexokinase I was probably detached from gold nanoparticles, since AuNPs can not migrate into the acrylamide-bisacrylamide gels due their high molecular weight (≈15 000 kDa). The detachment may have occurred inside cells, for example, by the lysosomal digestion [132] or during samples preparation steps. In a first approach, these results may indicate that AuNP@PEG@Anti-Hexokinase I were internalized by HCT116 cell, which corroborates the results described in the previous section (section 3.2). Moreover, Anti-Hexokinase I were identified in all HCT116 cell fractions incubated with AuNP@PEG@Anti-Hexokinase I, which could indicate that all fractions may have AuNP@PEG@Anti-Hexokinase I. However, these results do not totally agree with ICP-AES previously described in section 3.2. Some explanations could be: i) Anti-Hexokinase I were detached from AuNPs and released to cytoplasm, which explains why anti-hexokinase I were identified in cytoplasmatic fraction by western blot but no AuNP@PEG@Anti-Hexokinase I were identified by ICP-AES; ii) Anti-Hexokinase I in mitochondrial and nuclear fractions can be correlated with ICP-AES results, as evidence that AuNP@PEG@Anti-Hexokinase I were presented in these fractions. Both Western blot and Dot Blot show evidence that AuNP@PEG-COOH seems to have mitochondrial targeting.

The intensity of bands in western blot could not be quantified since the loading controls (e.g β-actin) were not successfully performed. Therefore, it was not possible to perform a quantitative analysis.

To corroborate the intracellular localization of AuNP@PEG@Anti-hexokinase I *in-vitro*, after uptake by HCT116 cells, FITC-conjugated secondary antibody that recognizes the anti-hexokinase I functionalized on the surface of gold nanoparticle was used in an immunofluorescence microscopy assay. Firstly, red fluorescence was observed in HCT116 cells incubated with AuNP@PEG@Anti-Hexokinase I and no red fluorescence were observed in HC116 without AuNP incubation and HCT116 incubated with AuNP@PEG-COOH. This proves that AuNP@PEG@Anti-Hexokinase I can be labeled and visualized through an immunoassay, using the Goat anti-rabbit IgG (TRITC) secondary antibody. Moreover, as figure **Figure 3.10** shows some AuNP@PEG@Anti-Hexokinase I seems to be co-localized in the mitochondria area: red fluorescence is in the same region of green fluorescence. Some limitations in this assay need to be highlighted, such as, the low efficiency of mitochondrial labeling. Even so, overlaps of green and red fluorescence are observed and, with the combination of the previous results, there are evidence that AuNP@PEG@Anti-Hexokinase I has specificity to target mitochondria.

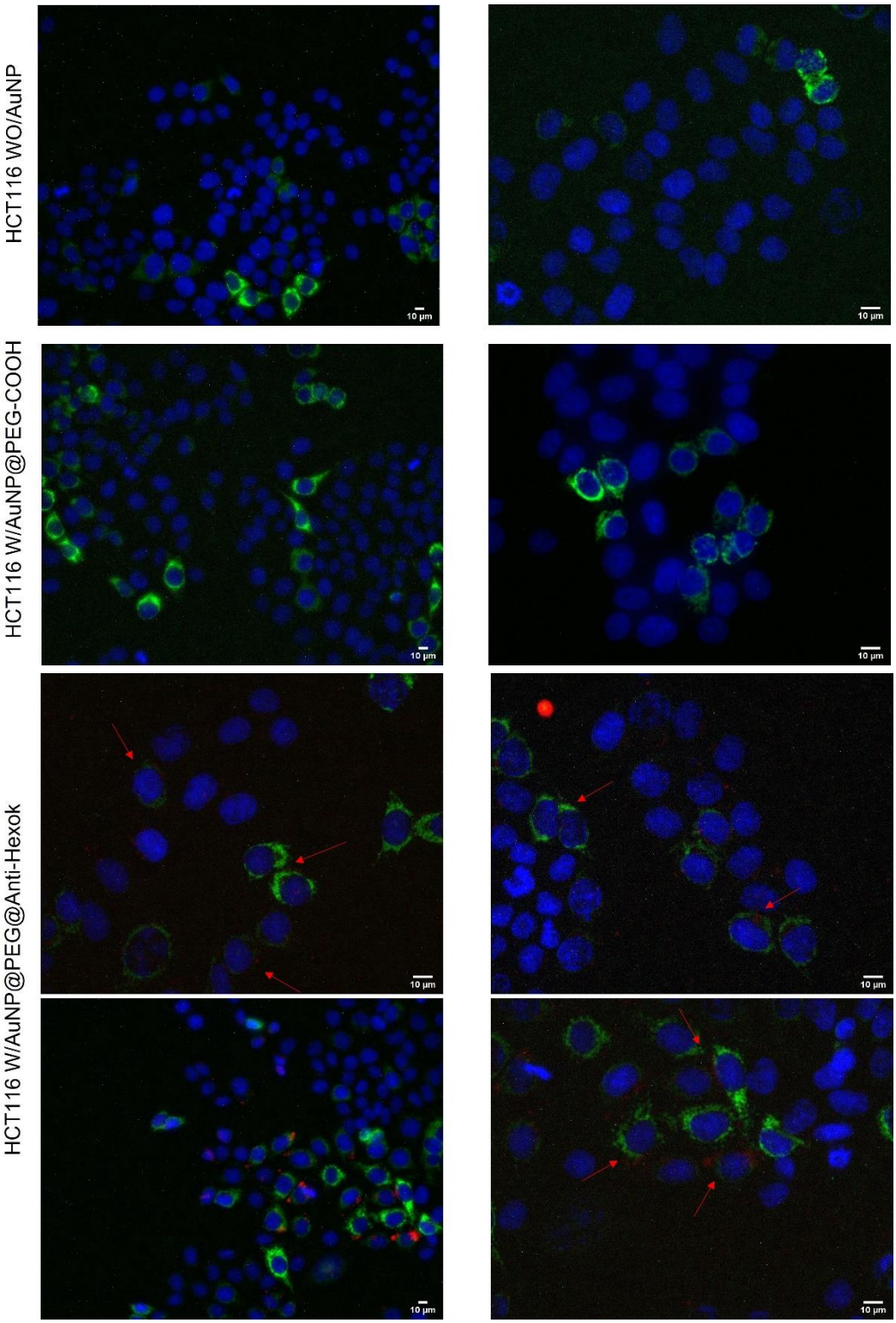

Figure 3.10 Immunofluorescence images of fixed HCT116 cells without any treatment, after 24h of AuNP@PEG-COOH incubation and 24h of AuNP@PEG@Anti-Hexokinase I incubation. HCT116 cells' nucleus were stained with Hoechst 33258 (blue) and mitochondria with CellLight™ Mitochondria-GFP (green). Red fluorescence corresponds to Goat anti-rabbit IgG (TRITC) secondary antibody (indicated by red arrows). Images were taken on inverted microscope The presented fluorescence images were treated using Image J software. Blue Scale bars represent 10 µm.

Indeed, immunofluorescence assay allowed to prove that part of AuNP@PEG@Anti-Hexokinase I was co-located in the mitochondrial area. However, there are still some questions that

might be addressed namely: i) which percentage of AuNP@PEG@Anti-Hexokinase I internalized by HCT116 can reached mitochondria? ii) Where were the AuNP@PEG-COOH internalized by HCT116 co-located? Although these questions could not be answered, due to accumulated evidence of mitochondrial targeting of AuNP@PEG@Anti-Hexokinase I provided by ICP-AES, Dot Blot, Western Blot and Immunofluorescence, their hyperthermia effect were tested and discussed in the next section. TEM and confocal microscopy are two examples of techinques that could be performed to more accurately identify the intracellular localization of AuNPs.

3.4 Hyperthermia effect of nanoconjugates against HCT116 cells

Evaluating the hyperthermia effect of AuNPs co-located in the mitochondria compared to AuNPs without an organelle targeting was the final goal of this thesis. As discussed in section 1.1.4, mitochondria are a promising organelle for targeting cancer therapies due to their involvement in cell survival (the cell's engine) and cell death pathways. Furthermore, for gold nanoparticles co-located in mitochondria of cancer cells, when subjected to a laser energy, OMM permeabilization or even mitochondria destruction was expected, as a consequence of the photo-induced hyperthermia. Thus, HCT116 cells incubated with 2.5 nM AuNP@PEG-COOH and AuNP@PEG@Anti-Heokinase I were irradiated with a green laser (2.37 $W.m^{-2}$ for 1 minute) and cell damage was evaluated by MTS assay and Trypan Blue count. At the same time, temperature increases were measured and analysed.

The MTS assay (**Figure 3.11 A**) and Trypan Blue cell count (**Figure 3.11 B**) performed 24h after incubation of HCT116 with 2.5nM AuNP@PEG-COOH and AuNP@PEG@Anti-Hexokinase I revealed that these nanoconjugates (under the conditions tested) *per se*, did not compromise the viability or

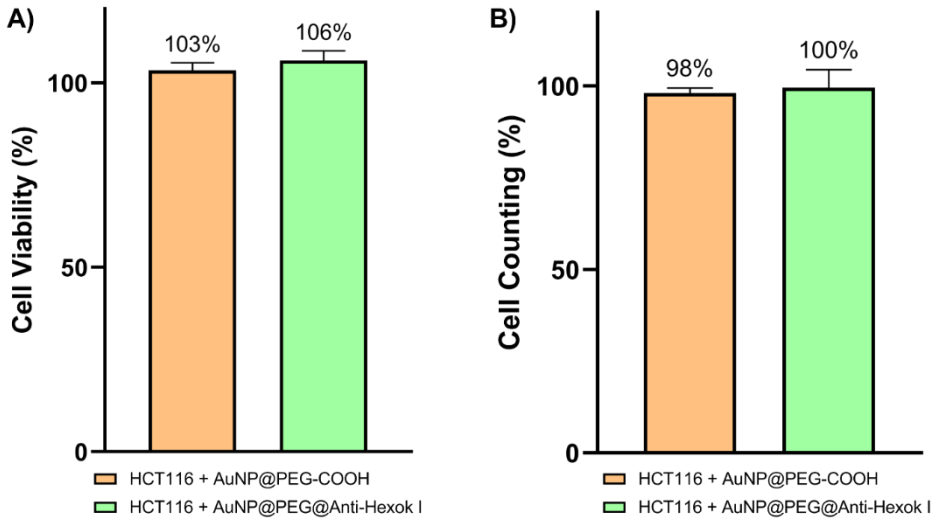

Figure 3.11 Cell viability and membrane integrity of HCT116 after 24h incubation with nanoconjugates (AuNP@PEG-COOH and AuNP@PEG@Anti-Hexokinase I). A) MTS assay; B) Trypan blue assay. Both results were normalized with HCT116 without nanoconjugates incubation. Mann-Whitney tests were performed and no significant differences were observed. The assay had two technical replicates and two biological replicates.

membrane integrity of HCT116 cells. Indeed, the cell viability calculated by the MTS assay overcome 100%. This effect has been observed previously in cells incubated with nanoparticles, and might result from an activation of cells metabolism due to nanoparticles uptake [133].

Additionally, MTS assay and Trypan Blue of HCT116 cells without AuNPs incubation but exposed to laser irradiation (**Figure 3.12 A and B**) revealed that laser irradiation (under the conditions tested), *per se,* also did not affect the cell viability and cells membrane integrity. After HCT116 cells were incubated with nanoconjugates and irradiated with the green laser (2.37 $W.m^{-2}$ for 1 minute), no significant differences were observed in cell viability and membrane integrity, with or without mitochondrial targeting (**Figure 3.12 A and B**). However, significant increases in the cell culture medium temperatures were observed after irradiation (6 °C increase with AuNP@PEG-COOH and 8 °C with AuNP@PEG@Anti-Hexokinase I) (**Table 3.3**). As mentioned in the section 1.2.2, when the temperature increases to 42°C cells undergo changes in gene expression and irreversible tissue damage occurs. However, these temperature does not cause lethal cell damage.

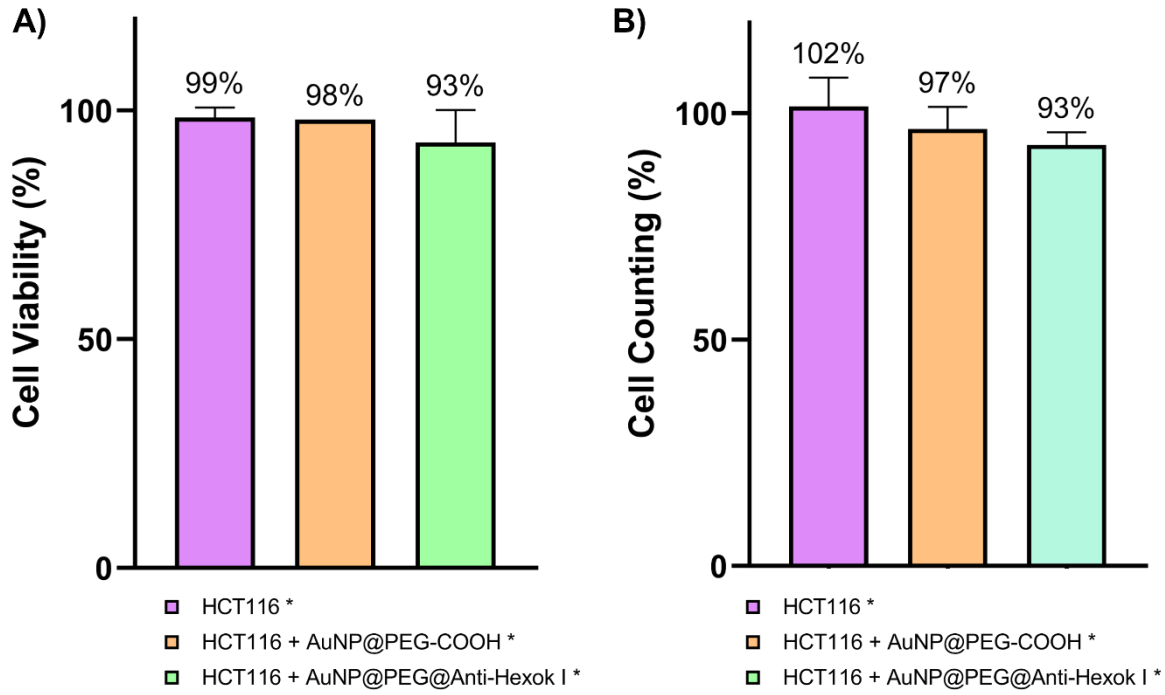

Figure 3.12 Cell viability and cell counting of HCT116 incubated with nanoconjugates (AuNP@PEG-COOH and AuNP@PEG@Anti-Hexokinase I) after irradiation with a power set to 2.37 W/cm² for 1 minute (*), evaluated by MTS Assay (A) and Trypan Blue Assay (B), respectively. The results were normalized with HCT116 Incubated with the same nanoconjugate tested by without having been irradiated. No significant differences were observed among different conditions. Mann-Whitney tests were performed, and no significant differences were observed. The assay had two technical replicates and two biological replicates.

Table 3.3 Temperature measurements of the DMEM cell culture before and after irradiation with the green laser (2.37 W.m^{-2} for 1 minute). It is important to note that hyperthermia assay was carried-out under non-regulated temperature conditions, denoting that temperature measurements could be influenced by increases in room temperature.

	Temperature °C		
	Before laser irradiation	After laser irradiation	ΔT
DMEM	34	36	2
DMEM + AuNP@PEG-COOH	36	38	2
DMEM + AuNP@PEG@Anti-Hexok	35	38	3
HCT116	36	36	0
HCT116 + AuNP@PEG-COOH	35	41	**6**
HCT116 + AuNP@PEG@Anti-Hexok	35	43	**8**

Since AuNP@PEG@Anti-Hexokinase I were shown to have mitochondrial targeting (section 3.3), when cells were exposed to irradiation and therefore temperature increase, a metabolic dysfunction caused by mitochondria destabilization was expected. Consequently, NADH and NADPH (energy carriers) high levels would be expected to decrease and reflected in the MTS assay, as described in section 2.9.2.1. The results (**Figure 3.12**), however, do not reflect this predicted outcome, and some hypotheses can be suggested: i) The low mitochondrial targeting rate: As demonstrated by ICP-AES and UV-Visible and discussed in section 3.3, the mitochondrial targeting rate of AuNP@PEG@Anti-Hexokinase I was not accurately determined, nevertheless, by immunofluorescence assay, it seems to be low. ii) Laser setups and irradiation time: Pedro Pedrosa [118] and Daniela Ferreira had already demonstrated in our laboratory that irradiating HCT116 cells with this laser intensity (2.37 W.m^{-2}) for 1 minute of exposition does not cause lethal effects or membrane rupture, however, the concentration and type of nanoconjugates used were not the same.

Indeed, hyperthermia effect of mitochondria-target gold nanoparticles (AuNP@PEG@Anti-Hexokinase I) was not observed compared to non-targeting gold nanoparticles (AuNP@PEG-COOH). Gold nanoparticles concentration, time of incubation (know the time point at the AuNPs accumulation in mitochondria reached the maximum) and laser setups must be optimized in order to get better outcomes.

4

CONCLUSION AND FUTURE PERSPECTIVES

Colorectal cancer remains the most prevalent cancer and the second leading cause of cancer death in Portugal. Surgery is the first therapeutical approach; however, the cancer recurrence rate is still high. New therapies have emerged, focusing on target drug delivery to the predicted cancer area. Mitochondria are a good target for cancer therapies, since they are responsible for coordinating cell survival, as the main catabolic reactions and biosynthetic pathways occurs there, as well as being associated with apoptotic pathways, being the apoptotic trigger in the intrinsic pathway. Due to the important role of mitochondria in cell maintenance, this work purposed to eradicate cancer cells by targeting AuNPs to their mitochondria and then, due to their optical features, kill cancer cells by hyperthermia.

Gold nanoconjugates (AuNP@Citrate, AuNP@PEG-COOH and AuNP@PEG@Anti-Hexokinase I) were successfully synthetized, functionalized, and characterized by: i) following the SPR peak by UV-Visible spectroscopy; ii) measuring the hydrodynamic size by DLS and iii) measuring the superficial charge by Zeta potential. These techniques allowed to follow that with each functionalization step of gold nanoparticles modification, a surface modification occurred, which are strong evidence of success of these reactional steps. Moreover, a 100% coverage of AuNPs with HS-PEG(8)-COOH may have increased the yield of functionalization with Anti-Hexokinase I, since the maximum of carboxyl groups (-COOH) were available to react with amine groups of antibodies. An average of 2 antibodies per AuNP was quantified, which despite being a low number, we proceeded with the experiments, and this result was taken as a good functionalization result. Although the uptake rate of AuNP@PEG-COOH and AuNP@PEG@Anti-Hexokinase I by HCT116 cells was not accurately quantified, Dot blot, Western Blot and Immunofluorescence results indicate that AuNP@PEG@Anti-Hexokinase I seemed to have mitochondrial targeting. To the final purpose of evaluate whether mitochondrial targeting of AuNPs has a prominent effect in killing cancer cells by hyperthermia, HCT116 cells incubated with 2.5nM of AuNP@PEG-COOH and AuNP@PEG@Anti-Hexokinase I for 24h were irradiated with a non-lethal laser intensity (2.37 $W.cm^{-2}$) for 1 minute. No cytotoxic effects or membrane disruption were observed.

These results do not invalidate the initial hypothesis, since some steps still need to be optimized, such as: i) improve the functionalization yield of AuNPs with the anti-Hexokinase I (> 5 antibodies per AuNPs); ii) accurately quantify the internalization rate of the nanoconjugate, and the time point at which the internalization and mitochondrial targeting reach their maximum; and iii) readjust the laser settings to provide a therapeutic effect. It is also important to account the intracellular route of gold nanoconjugates before reaching the target, which rises some questions: can the AuNP@PEG@Anti-Hexokinase I resist to lysosomal degradation? Or Is Anti-Hexokinase I detached from AuNPs due to the low lysosomal pH? What is the fate of untargeted AuNPs?

Furthermore, as AuNP@PEG@Anti-Hexokinase I do not specifically target cancer cells, surfaces modification which give them this specification is also required (e.g., anti- EGFR). Then, the specific targeting of cancer cells mitochondria could be tested using co-cultures of cancer cells (HCT116 cells) and non-cancer cells (e.g., fibroblast, colon cells). With these questions answered this new nanoformulation could be very promising in the field of cancer therapy. Even if the hyperthermia effects are not observed, AuNP@PEG@Anti-Hexokinase I can be seen as a mitochondrial vehicle for drug delivery: their surface can also be functionalized with other molecules (e.g., antitumor drugs) and due to Anti-Hexokinase I target, it can be effectively delivered to the mitochondria of cancer cells to improve the therapeutic effect.

REFERENCES

[1] T. Ahmad, R. Sarwar, A. Iqbal, U. Bashir, U. Farooq, S.A. Halim, A. Khan, A. Al-Harrasi, Recent advances in combinatorial cancer therapy via multifunctionalized gold nanoparticles, Nanomedicine. 15 (2020) 1221–1237. https://doi.org/10.2217/nnm-2020-0051.

[2] World Health Organization, (n.d.). https://gco.iarc.fr/ (accessed September 5, 2022).

[3] C. Mattiuzzi, G. Lippi, Current Cancer Epidemiology, J. Epidemiol. Glob. Health. 9 (2019) 217. https://doi.org/10.2991/jegh.k.191008.001.

[4] E.N. Kontomanolis, A. Koutras, A. Syllaios, D. Schizas, S. Kalagasidou, A. Pagkalos, D. Alatzidou, P. Kantari, T. Ntounis, Z. Fasoulakis, Basic principles of molecular biology of cancer cell-Molecular cancer indicators, J. B.U.ON. 26 (2021) 1723–1734.

[5] L. Ding, J. Cao, W. Lin, H. Chen, X. Xiong, H. Ao, M. Yu, J. Lin, Q. Cui, The roles of cyclin-dependent kinases in cell-cycle progression and therapeutic strategies in human breast cancer, Int. J. Mol. Sci. 21 (2020) 1–28. https://doi.org/10.3390/ijms21061960.

[6] P. Nenclares, K.J. Harrington, The biology of cancer, Med. (United Kingdom). 48 (2020) 67–72. https://doi.org/10.1016/j.mpmed.2019.11.001.

[7] C.D.B. and E.S.L. T. R. Golub, D. K. Slonim, P. Tamayo, C. Huard, M. Gaasenbeek, J. P. Mesirov, H. Coller, M. L. Loh, J. R. Downing, M. A. Caligiuri, Molecular Classification of Cancer: Class Discovery and Class Prediction by Gene Expression Monitoring, Science (80-.). 286 (1999) 531–537. https://www.jstor.org/stable/2899325.

[8] H. Kalkavan, D.R. Green, MOMP, cell suicide as a BCL-2 family business, Cell Death Differ. 25 (2018) 46–55. https://doi.org/10.1038/cdd.2017.179.

[9] S. Fulda, Evasion of apoptosis as a cellular stress response in cancer, Int. J. Cell Biol. 2010 (2010). https://doi.org/10.1155/2010/370835.

[10] J. Kale, E.J. Osterlund, D.W. Andrews, BCL-2 family proteins: Changing partners in the dance towards death, Cell Death Differ. 25 (2018) 65–80. https://doi.org/10.1038/cdd.2017.186.

[11] G.I. Evan, K.H. Vousden, Proliferation, cell cycle and apoptosis in cancer, Nature. 411 (2001) 342–348. https://doi.org/10.1038/35077213.

[12] S. Fulda, L. Galluzzi, G. Kroemer, Targeting mitochondria for cancer therapy, Nat. Rev. Drug Discov. 9 (2010) 447–464. https://doi.org/10.1038/nrd3137.

[13] T.A. Tabish, M.R. Hamblin, Mitochondria-targeted nanoparticles (mitoNANO): An emerging therapeutic shortcut for cancer, Biomater. Biosyst. 3 (2021) 100023. https://doi.org/10.1016/j.bbiosy.2021.100023.

[14] X.S. Hou, H.S. Wang, B.P. Mugaka, G.J. Yang, Y. Ding, Mitochondria: Promising organelle targets for cancer diagnosis and treatment, Biomater. Sci. 6 (2018) 2786–2797. https://doi.org/10.1039/c8bm00673c.

[15] S.Y. Lunt, M.G. Vander Heiden, Aerobic Glycolysis: Meeting the Metabolic Requirements of Cell Proliferation, Annu. Rev. Cell Dev. Biol. 27 (2011) 441–464. https://doi.org/10.1146/annurev-cellbio-092910-154237.

[16] S.E. Weinberg, N.S. Chandel, Targeting mitochondria metabolism for cancer therapy, Nat. Chem. Biol. 11 (2015) 9–15. https://doi.org/10.1038/nchembio.1712.

[17] R. Zhao, S. Jiang, L. Zhang, Z. Yu, Mitochondrial electron transport chain, ROS generation and uncoupling (Review), Int. J. Mol. Med. (2019). https://doi.org/10.3892/ijmm.2019.4188.
[18] M. Ahmad, A. Wolberg, C.I. Kahwaji, Biochemistry, Electron Transport Chain, 2022. http://www.ncbi.nlm.nih.gov/pubmed/30252361.
[19] W. Kühlbrandt, Structure and function of mitochondrial membrane protein complexes, BMC Biol. 13 (2015) 89. https://doi.org/10.1186/s12915-015-0201-x.
[20] R.J. DeBerardinis, N.S. Chandel, Fundamentals of cancer metabolism, Sci. Adv. 2 (2016). https://doi.org/10.1126/sciadv.1600200.
[21] A. Kicinska, W. Jarmuszkiewicz, Flavonoids and Mitochondria: Activation of Cytoprotective Pathways?, Molecules. 25 (2020) 3060. https://doi.org/10.3390/molecules25133060.
[22] P. Ghosh, C. Vidal, S. Dey, L. Zhang, Mitochondria Targeting as an Effective Strategy for Cancer Therapy, Int. J. Mol. Sci. 21 (2020) 3363. https://doi.org/10.3390/ijms21093363.
[23] M. V. Liberti, J.W. Locasale, The Warburg Effect: How Does it Benefit Cancer Cells?, Trends Biochem. Sci. 41 (2016) 211–218. https://doi.org/10.1016/j.tibs.2015.12.001.
[24] O. Warburg, On the Origin of Cancer Cells, Science (80-.). 123 (1956) 309–314. https://doi.org/10.1126/science.123.3191.309.
[25] S. Bose, A. Le, Glucose Metabolism in Cancer, in: Heterog. Cancer Metab. Adv. Exp. Med. Biol., Springer International Publishing, 2018: pp. 3–12. https://doi.org/10.1007/978-3-319-77736-8_1.
[26] N. Hay, Reprogramming glucose metabolism in cancer: Can it be exploited for cancer therapy?, Nat. Rev. Cancer. 16 (2016) 635–649. https://doi.org/10.1038/nrc.2016.77.
[27] Y. Yang, S. Karakhanova, W. Hartwig, J.G. D'Haese, P.P. Philippov, J. Werner, A. V. Bazhin, Mitochondria and Mitochondrial ROS in Cancer: Novel Targets for Anticancer Therapy, J. Cell. Physiol. 231 (2016) 2570–2581. https://doi.org/10.1002/jcp.25349.
[28] L.B. Sullivan, N.S. Chandel, Mitochondrial reactive oxygen species and cancer, Cancer Metab. 2 (2014) 17. https://doi.org/10.1186/2049-3002-2-17.
[29] M.P. Murphy, How mitochondria produce reactive oxygen species, Biochem. J. 417 (2009) 1–13. https://doi.org/10.1042/BJ20081386.
[30] C. Gorrini, I.S. Harris, T.W. Mak, Modulation of oxidative stress as an anticancer strategy, Nat. Rev. Drug Discov. 12 (2013) 931–947. https://doi.org/10.1038/nrd4002.
[31] H. Brenner, M. Kloor, C.P. Pox, Colorectal cancer, Lancet. 383 (2014) 1490–1502. https://doi.org/10.1016/S0140-6736(13)61649-9.
[32] K. Simon, Colorectal cancer development and advances in screening, Clin. Interv. Aging. 11 (2016) 967–976. https://doi.org/10.2147/CIA.S109285.
[33] American Cancer Society, (n.d.). cancer.org %7C 1.800.227.2345 (accessed May 23, 2022).
[34] N.N. Keum, E. Giovannucci, Global burden of colorectal cancer: emerging trends, risk factors and prevention strategies, Nat. Rev. Gastroenterol. Hepatol. 16 (2019) 713–732. https://doi.org/10.1038/s41575-019-0189-8.
[35] E.R. Fearon, B. Vogelstein, A genetic model for colorectal tumorigenesis, Cell. 61 (1990) 759–767. https://doi.org/10.1016/0092-8674(90)90186-I.
[36] J. Li, X. Ma, D. Chakravarti, S. Shalapour, R.A. DePinho, Genetic and biological hallmarks of colorectal cancer, Genes Dev. 35 (2021) 787–820. https://doi.org/10.1101/gad.348226.120.
[37] L. Yamane, C. Scapulatempo-Neto, R.M. Reis, D.P. Guimarães, Serrated pathway in colorectal carcinogenesis, World J. Gastroenterol. 20 (2014) 2634–2640. https://doi.org/10.3748/wjg.v20.i10.2634.
[38] Z.Z.J. Lim, J.E.J. Li, C.T. Ng, L.Y.L. Yung, B.H. Bay, Gold nanoparticles in cancer therapy, Acta Pharmacol. Sin. 32 (2011) 983–990. https://doi.org/10.1038/aps.2011.82.
[39] X. Guo, N. Yang, W. Ji, H. Zhang, X. Dong, Z. Zhou, L. Li, H. Shen, S.Q. Yao, W. Huang, Mito-Bomb: Targeting Mitochondria for Cancer Therapy, Adv. Mater. 33 (2021) 2007778. https://doi.org/10.1002/adma.202007778.
[40] N.W. Nkune, C.A. Kruger, H. Abrahamse, Possible Enhancement of Photodynamic Therapy (PDT) Colorectal Cancer Treatment when Combined with Cannabidiol, Anticancer. Agents Med. Chem. 21 (2021) 137–148. https://doi.org/10.2174/1871520620666200415102321.
[41] T.A. Greenhalgh, R.P. Symonds, Principles of chemotherapy and radiotherapy, Obstet. Gynaecol. Reprod. Med. 24 (2014) 259–265. https://doi.org/10.1016/j.ogrm.2014.06.004.
[42] J.R. Ashton, K.D. Castle, Y. Qi, D.G. Kirsch, J.L. West, C.T. Badea, Dual-energy CT imaging of tumor liposome delivery after gold nanoparticle-augmented radiation therapy, Theranostics. 8 (2018) 1782–1797. https://doi.org/10.7150/thno.22621.
[43] J.B. Vines, J.H. Yoon, N.E. Ryu, D.J. Lim, H. Park, Gold nanoparticles for photothermal cancer

therapy, Front. Chem. 7 (2019) 1–16. https://doi.org/10.3389/fchem.2019.00167.
[44] X. Li, J.F. Lovell, J. Yoon, X. Chen, Clinical development and potential of photothermal and photodynamic therapies for cancer, Nat. Rev. Clin. Oncol. 17 (2020) 657–674. https://doi.org/10.1038/s41571-020-0410-2.
[45] N.S. Aminabad, M. Farshbaf, A. Akbarzadeh, Recent Advances of Gold Nanoparticles in Biomedical Applications: State of the Art, Cell Biochem. Biophys. 77 (2019) 123–137. https://doi.org/10.1007/s12013-018-0863-4.
[46] L. Zhao, X. Zhang, X. Wang, X. Guan, W. Zhang, J. Ma, Recent advances in selective photothermal therapy of tumor, J. Nanobiotechnology. 19 (2021) 335. https://doi.org/10.1186/s12951-021-01080-3.
[47] H. Shi, P.J. Sadler, How promising is phototherapy for cancer?, Br. J. Cancer. 123 (2020) 871–873. https://doi.org/10.1038/s41416-020-0926-3.
[48] R. Baskaran, J. Lee, S.-G. Yang, Clinical development of photodynamic agents and therapeutic applications, Biomater. Res. 22 (2018) 25. https://doi.org/10.1186/s40824-018-0140-z.
[49] G. Abdulrehman, K. Xv, Y. Li, L. Kang, Effects of meta-tetrahydroxyphenylchlorin photodynamic therapy on isogenic colorectal cancer SW480 and SW620 cells with different metastatic potentials, Lasers Med. Sci. 33 (2018) 1581–1590. https://doi.org/10.1007/s10103-018-2524-7.
[50] A. Kawczyk-Krupka, W. Latos, P. Oleś, Z.P. Czuba, M. Latos, M. Krupka, H. Pengyun, C. Xu, G. Cieślar, A. Sieroń, The influence of 5-aminolevulinic photodynamic therapy on colon cancer cell interleukin secretion in hypoxia-like condition in vitro, Photodiagnosis Photodyn. Ther. 23 (2018) 240–243. https://doi.org/10.1016/j.pdpdt.2018.07.007.
[51] F. Şueki, M.K. Ruhi, M. Gülsoy, The effect of curcumin in antitumor photodynamic therapy: In vitro experiments with Caco-2 and PC-3 cancer lines, Photodiagnosis Photodyn. Ther. 27 (2019) 95–99. https://doi.org/10.1016/j.pdpdt.2019.05.012.
[52] B. Zhu, S. Li, L. Yu, W. Hu, D. Sheng, J. Hou, N. Zhao, X. Hou, Y. Wu, Z. Han, L. Wei, L. Zhang, Inhibition of Autophagy with Chloroquine Enhanced Sinoporphyrin Sodium Mediated Photodynamic Therapy-induced Apoptosis in Human Colorectal Cancer Cells, Int. J. Biol. Sci. 15 (2019) 12–23. https://doi.org/10.7150/ijbs.27156.
[53] T. Hatakeyama, Y. Murayama, S. Komatsu, M. Nakajima, E. Otsuji, Efficacy of 5-aminolevulinic acid-mediated photodynamic therapy using light-emitting diodes in human colon cancer cells, Oncol. Rep. 29 (2013) 911–916. https://doi.org/10.3892/or.2013.2220.
[54] S. Keereweer, P.B.A.A. Van Driel, D.J. Robinson, C.W.G.M. Lowik, Shifting Focus in Optical Image-Guided Cancer Therapy, Mol. Imaging Biol. 16 (2014) 1–9. https://doi.org/10.1007/s11307-013-0688-x.
[55] F. Lin, Y.-W. Bao, F.-G. Wu, Improving the Phototherapeutic Efficiencies of Molecular and Nanoscale Materials by Targeting Mitochondria, Molecules. 23 (2018) 3016. https://doi.org/10.3390/molecules23113016.
[56] J. Conde, G. Doria, P. Baptista, Noble Metal Nanoparticles Applications in Cancer, J. Drug Deliv. 2012 (2012) 1–12. https://doi.org/10.1155/2012/751075.
[57] A.P. Nikalje, Nanotechnology and its Applications in Medicine, Med. Chem. (Los. Angeles). 5 (2015) 81–89. https://doi.org/10.4172/2161-0444.1000247.
[58] C. Roma-rodrigues, L. Rivas-garcía, P. V. Baptista, A.R. Fernandes, Gene therapy in cancer treatment: Why go nano?, Pharmaceutics. 12 (2020). https://doi.org/10.3390/pharmaceutics12030233.
[59] J. Gonzalez-Valdivieso, A. Girotti, J. Schneider, F.J. Arias, Advanced nanomedicine and cancer: Challenges and opportunities in clinical translation, Int. J. Pharm. 599 (2021) 120438. https://doi.org/10.1016/j.ijpharm.2021.120438.
[60] F. Villanueva-Flores, A. Castro-Lugo, O.T. Ramírez, L.A. Palomares, Understanding cellular interactions with nanomaterials: towards a rational design of medical nanodevices, Nanotechnology. 31 (2020) 132002. https://doi.org/10.1088/1361-6528/ab5bc8.
[61] E.C. Cho, C. Glaus, J. Chen, M.J. Welch, Y. Xia, Inorganic nanoparticle-based contrast agents for molecular imaging, Trends Mol. Med. 16 (2010) 561–573. https://doi.org/10.1016/j.molmed.2010.09.004.
[62] A.M. Jhaveri, V.P. Torchilin, Multifunctional polymeric micelles for delivery of drugs and siRNA, Front. Pharmacol. 5 (2014). https://doi.org/10.3389/fphar.2014.00077.
[63] G. Wei, Y. Wang, G. Yang, Y. Wang, R. Ju, Recent progress in nanomedicine for enhanced cancer chemotherapy, Theranostics. 11 (2021) 6370–6392. https://doi.org/10.7150/thno.57828.
[64] R.M. Schiffelers, G.A. Koning, T.L.M. Ten Hagen, M.H.A.M. Fens, A.J. Schraa, A.P.C.A.

Janssen, R.J. Kok, G. Molema, G. Storm, Anti-tumor efficacy of tumor vasculature-targeted liposomal doxorubicin, J. Control. Release. 91 (2003) 115–122. https://doi.org/10.1016/S0168-3659(03)00240-2.
[65] C. Wang, M. Zhao, Y.R. Liu, X. Luan, Y.Y. Guan, Q. Lu, D.H. Yu, F. Bai, H.Z. Chen, C. Fang, Suppression of colorectal cancer subcutaneous xenograft and experimental lung metastasis using nanoparticle-mediated drug delivery to tumor neovasculature, Biomaterials. 35 (2014) 1215–1226. https://doi.org/10.1016/j.biomaterials.2013.08.091.
[66] L.Y. Qiu, L. Yan, L. Zhang, Y.M. Jin, Q.H. Zhao, Folate-modified poly(2-ethyl-2-oxazoline) as hydrophilic corona in polymeric micelles for enhanced intracellular doxorubicin delivery, Int. J. Pharm. 456 (2013) 315–324. https://doi.org/10.1016/j.ijpharm.2013.08.071.
[67] J. Li, M. Huo, J. Wang, J. Zhou, J.M. Mohammad, Y. Zhang, Q. Zhu, A.Y. Waddad, Q. Zhang, Redox-sensitive micelles self-assembled from amphiphilic hyaluronic acid-deoxycholic acid conjugates for targeted intracellular delivery of paclitaxel, Biomaterials. 33 (2012) 2310–2320. https://doi.org/10.1016/j.biomaterials.2011.11.022.
[68] G. Yu, D. Wu, Y. Li, Z. Zhang, L. Shao, J. Zhou, Q. Hu, G. Tang, F. Huang, A pillar[5]arene-based [2]rotaxane lights up mitochondria, Chem. Sci. 7 (2016) 3017–3024. https://doi.org/10.1039/c6sc00036c.
[69] Y. Tan, Y. Zhu, Y. Zhao, L. Wen, T. Meng, X. Liu, X. Yang, S. Dai, H. Yuan, F. Hu, Mitochondrial alkaline pH-responsive drug release mediated by Celastrol loaded glycolipid-like micelles for cancer therapy, Biomaterials. 154 (2018) 169–181. https://doi.org/10.1016/j.biomaterials.2017.07.036.
[70] Y. Jing, X. Xiong, Y. Ming, J. Zhao, X. Guo, G. Yang, S. Zhou, A Multifunctional Micellar Nanoplatform with pH-Triggered Cell Penetration and Nuclear Targeting for Effective Cancer Therapy and Inhibition to Lung Metastasis, Adv. Healthc. Mater. 7 (2018) 1–13. https://doi.org/10.1002/adhm.201700974.
[71] H. Li, P. Zhang, J. Luo, D. Hu, Y. Huang, Z.R. Zhang, Y. Fu, T. Gong, Chondroitin Sulfate-Linked Prodrug Nanoparticles Target the Golgi Apparatus for Cancer Metastasis Treatment, ACS Nano. 13 (2019) 9386–9396. https://doi.org/10.1021/acsnano.9b04166.
[72] M.H. Jazayeri, H. Amani, A.A. Pourfatollah, H. Pazoki-Toroudi, B. Sedighimoghaddam, Various methods of gold nanoparticles (GNPs) conjugation to antibodies, Sens. Bio-Sensing Res. 9 (2016) 17–22. https://doi.org/10.1016/j.sbsr.2016.04.002.
[73] D. Ferreira, D. Fontinha, C. Martins, D. Pires, A.R. Fernandes, P. V. Baptista, Gold nanoparticles for vectorization of nucleic acids for cancer therapeutics, Molecules. 25 (2020). https://doi.org/10.3390/molecules25153489.
[74] P. Tiwari, K. Vig, V. Dennis, S. Singh, Functionalized Gold Nanoparticles and Their Biomedical Applications, Nanomaterials. 1 (2011) 31–63. https://doi.org/10.3390/nano1010031.
[75] T.F. Massoud, S.S. Gambhir, Molecular imaging in living subjects: seeing fundamental biological processes in a new light, Genes Dev. 17 (2003) 545–580. https://doi.org/10.1101/gad.1047403.
[76] J.-W. Lim, S.U. Son, E.-K. Lim, Recent Advances in Bioimaging for Cancer Research, in: State Art Nano-Bioimaging, InTech, 2018. https://doi.org/10.5772/intechopen.72725.
[77] Q. Yuan, S. Hein, R.D.K. Misra, New generation of chitosan-encapsulated ZnO quantum dots loaded with drug: Synthesis, characterization and in vitro drug delivery response, Acta Biomater. 6 (2010) 2732–2739. https://doi.org/10.1016/j.actbio.2010.01.025.
[78] O. Veiseh, J.W. Gunn, M. Zhang, Design and fabrication of magnetic nanoparticles for targeted drug delivery and imaging, Adv. Drug Deliv. Rev. 62 (2010) 284–304. https://doi.org/10.1016/j.addr.2009.11.002.
[79] R. Nosrati, K. Abnous, M. Alibolandi, J. Mosafer, S. Dehghani, S.M. Taghdisi, M. Ramezani, Targeted SPION siderophore conjugate loaded with doxorubicin as a theranostic agent for imaging and treatment of colon carcinoma, Sci. Rep. 11 (2021) 13065. https://doi.org/10.1038/s41598-021-92391-w.
[80] J. Guo, K. Rahme, Y. He, L.-L. Li, J. Holmes, C. O'Driscoll, Gold nanoparticles enlighten the future of cancer theranostics, Int. J. Nanomedicine. Volume 12 (2017) 6131–6152. https://doi.org/10.2147/IJN.S140772.
[81] Y. Yang, L. Wang, B. Wan, Y. Gu, X. Li, Optically Active Nanomaterials for Bioimaging and Targeted Therapy, Front. Bioeng. Biotechnol. 7 (2019). https://doi.org/10.3389/fbioe.2019.00320.
[82] Y. Wu, M.R.K. Ali, K. Chen, N. Fang, M.A. El-Sayed, Gold nanoparticles in biological optical imaging, Nano Today. 24 (2019) 120–140. https://doi.org/10.1016/j.nantod.2018.12.006.

[83] C. Roma-Rodrigues, L.R. Raposo, R. Valente, A.R. Fernandes, P. V. Baptista, Combined cancer therapeutics—Tackling the complexity of the tumor microenvironment, Wiley Interdiscip. Rev. Nanomedicine Nanobiotechnology. 13 (2021) 1–18. https://doi.org/10.1002/wnan.1704.
[84] M. Kus-liśkiewicz, P. Fickers, I. Ben Tahar, Biocompatibility and cytotoxicity of gold nanoparticles: Recent advances in methodologies and regulations, Int. J. Mol. Sci. 22 (2021). https://doi.org/10.3390/ijms222010952.
[85] X.D. Zhang, D. Wu, X. Shen, P.X. Liu, N. Yang, B. Zhao, H. Zhang, Y.M. Sun, L.A. Zhang, F.Y. Fan, Size-dependent in vivo toxicity of PEG-coated gold nanoparticles., Int. J. Nanomedicine. 6 (2011) 2071–2081. https://doi.org/10.2147/ijn.s21657.
[86] A.R. Fernandes, J. Jesus, P. Martins, S. Figueiredo, D. Rosa, L.M.R.D.R.S. Martins, M.L. Corvo, M.C. Carvalheiro, P.M. Costa, P. V. Baptista, Multifunctional gold-nanoparticles: A nanovectorization tool for the targeted delivery of novel chemotherapeutic agents, J. Control. Release. 245 (2017) 52–61. https://doi.org/10.1016/j.jconrel.2016.11.021.
[87] Y. Wang, Z. Gao, Z. Han, Y. Liu, H. Yang, T. Akkin, C.J. Hogan, J.C. Bischof, Aggregation affects optical properties and photothermal heating of gold nanospheres, Sci. Rep. 11 (2021) 1–12. https://doi.org/10.1038/s41598-020-79393-w.
[88] C. Roma-Rodrigues, I. Pombo, A.R. Fernandes, P. V. Baptista, Hyperthermia Induced by Gold Nanoparticles and Visible Light Photothermy Combined with Chemotherapy to Tackle Doxorubicin Sensitive and Resistant Colorectal Tumor 3D Spheroids, Int. J. Mol. Sci. 21 (2020) 8017. https://doi.org/10.3390/ijms21218017.
[89] E. Okoampah, Y. Mao, S. Yang, S. Sun, C. Zhou, Gold nanoparticles–biomembrane interactions: From fundamental to simulation, Colloids Surfaces B Biointerfaces. 196 (2020) 111312. https://doi.org/10.1016/j.colsurfb.2020.111312.
[90] J.P.M. Almeida, A.L. Chen, A. Foster, R. Drezek, In vivo biodistribution of nanoparticles, Nanomedicine. 6 (2011) 815–835. https://doi.org/10.2217/nnm.11.79.
[91] A. Chrastina, K.A. Massey, J.E. Schnitzer, Overcoming in vivo barriers to targeted nanodelivery, Wiley Interdiscip. Rev. Nanomedicine Nanobiotechnology. 3 (2011) 421–437. https://doi.org/10.1002/wnan.143.
[92] B.D. Chithrani, A.A. Ghazani, W.C.W. Chan, Determining the size and shape dependence of gold nanoparticle uptake into mammalian cells, Nano Lett. 6 (2006) 662–668. https://doi.org/10.1021/nl052396o.
[93] P. Foroozandeh, A.A. Aziz, Insight into Cellular Uptake and Intracellular Trafficking of Nanoparticles, Nanoscale Res. Lett. 13 (2018). https://doi.org/10.1186/s11671-018-2728-6.
[94] N.D. Donahue, H. Acar, S. Wilhelm, Concepts of nanoparticle cellular uptake, intracellular trafficking, and kinetics in nanomedicine, Adv. Drug Deliv. Rev. 143 (2019) 68–96. https://doi.org/10.1016/j.addr.2019.04.008.
[95] F. Porta, G.E.M. Lamers, J. Morrhayim, A. Chatzopoulou, M. Schaaf, H. den Dulk, C. Backendorf, J.I. Zink, A. Kros, Folic Acid-Modified Mesoporous Silica Nanoparticles for Cellular and Nuclear Targeted Drug Delivery, Adv. Healthc. Mater. 2 (2013) 281–286. https://doi.org/10.1002/adhm.201200176.
[96] W. Qian, X. Huang, B. Kang, M.A. El-Sayed, Dark-field light scattering imaging of living cancer cell component from birth through division using bioconjugated gold nanoprobes, J. Biomed. Opt. 15 (2010) 046025. https://doi.org/10.1117/1.3477179.
[97] H.J. Kwon, M.-Y. Cha, D. Kim, D.K. Kim, M. Soh, K. Shin, T. Hyeon, I. Mook-Jung, Mitochondria-Targeting Ceria Nanoparticles as Antioxidants for Alzheimer's Disease, ACS Nano. 10 (2016) 2860–2870. https://doi.org/10.1021/acsnano.5b08045.
[98] S. Mallick, S.J. Song, Y. Bae, J.S. Choi, Self-assembled nanoparticles composed of glycol chitosan-dequalinium for mitochondria-targeted drug delivery, Int. J. Biol. Macromol. 132 (2019) 451–460. https://doi.org/10.1016/j.ijbiomac.2019.03.215.
[99] Z. Zhang, L. Zhou, Y. Zhou, J. Liu, X. Xing, J. Zhong, G. Xu, Z. Kang, J. Liu, Mitophagy induced by nanoparticle–peptide conjugates enabling an alternative intracellular trafficking route, Biomaterials. 65 (2015) 56–65. https://doi.org/10.1016/j.biomaterials.2015.06.029.
[100] R.S. Li, P.F. Gao, H.Z. Zhang, L.L. Zheng, C.M. Li, J. Wang, Y.F. Li, F. Liu, N. Li, C.Z. Huang, Chiral nanoprobes for targeting and long-term imaging of the Golgi apparatus, Chem. Sci. 8 (2017) 6829–6835. https://doi.org/10.1039/C7SC01316G.
[101] S.H. Lee, D.J. Park, W.S. Yun, J.-E. Park, J.S. Choi, J. Key, Y.J. Seo, Endocytic trafficking of polymeric clustered superparamagnetic iron oxide nanoparticles in mesenchymal stem cells, J. Control. Release. 326 (2020) 408–418. https://doi.org/10.1016/j.jconrel.2020.07.032.

[102] M.M. Mkandawire, M. Lakatos, A. Springer, A. Clemens, D. Appelhans, U. Krause-Buchholz, W. Pompe, G. Rödel, M. Mkandawire, Induction of apoptosis in human cancer cells by targeting mitochondria with gold nanoparticles, Nanoscale. 7 (2015) 10634–10640. https://doi.org/10.1039/C5NR01483B.
[103] J. Kimling, M. Maier, B. Okenve, V. Kotaidis, H. Ballot, A. Plech, Turkevich Method for Gold Nanoparticle Synthesis Revisited, J. Phys. Chem. B. 110 (2006) 15700–15707. https://doi.org/10.1021/jp061667w.
[104] P. Baptista, J. Conde, J. Rosa, P. Baptista, Gold-Nanobeacons as a theranostic system for the detection and inhibition of specific genes, Protoc. Exch. (2013) 1–46. https://doi.org/10.1038/protex.2013.088.
[105] W. Haiss, N.T.K. Thanh, J. Aveyard, D.G. Fernig, Determination of size and concentration of gold nanoparticles from UV-Vis spectra, Anal. Chem. 79 (2007) 4215–4221. https://doi.org/10.1021/ac0702084.
[106] E.L.L. Yeo, A.J.S. Chua, K. Parthasarathy, H.Y. Yeo, M.L. Ng, J.C.Y. Kah, Understanding aggregation-based assays: nature of protein corona and number of epitopes on antigen matters, RSC Adv. 5 (2015) 14982–14993. https://doi.org/10.1039/C4RA12089B.
[107] R.T. Busch, F. Karim, J. Weis, Y. Sun, C. Zhao, E.S. Vasquez, Optimization and Structural Stability of Gold Nanoparticle-Antibody Bioconjugates, ACS Omega. 4 (2019) 15269–15279. https://doi.org/10.1021/acsomega.9b02276.
[108] T. Mudalige, H. Qu, D. Van Haute, S.M. Ansar, A. Paredes, T. Ingle, Characterization of Nanomaterials: Tools and Challenges, in: Nanomater. Food Appl., Elsevier, 2019: pp. 313–353. https://doi.org/10.1016/B978-0-12-814130-4.00011-7.
[109] A.S. Dileseigres, Y. Prado, O. Pluchery, How to Use Localized Surface Plasmon for Monitoring the Adsorption of Thiol Molecules on Gold Nanoparticles?, Nanomaterials. 12 (2022) 292. https://doi.org/10.3390/nano12020292.
[110] J. Conde, J. Rosa, J.M. de la Fuente, P. V. Baptista, Gold-nanobeacons for simultaneous gene specific silencing and intracellular tracking of the silencing events, Biomaterials. 34 (2013) 2516–2523. https://doi.org/10.1016/j.biomaterials.2012.12.015.
[111] A.R. Fernandes, P. V. Baptista, Gene Silencing Using Multifunctionalized Gold Nanoparticles for Cancer Therapy, in: Cancer Nanotechnol., 2016: pp. 319–336. https://doi.org/10.1007/978-1-4939-6646-2.
[112] J.M. Becker, G.A. Caldwell, E.A. Zachgo, Protein Assays, in: Biotechnology, Elsevier, 1996: pp. 119–124. https://doi.org/10.1016/B978-012084562-0/50069-2.
[113] N.J. Kruger, The Bradford Method For Protein Quantitation, in: 2009: pp. 17–24. https://doi.org/10.1007/978-1-59745-198-7_4.
[114] J.J. Sedmak, S.E. Grossberg, A rapid, sensitive, and versatile assay for protein using Coomassie brilliant blue G250, Anal. Biochem. 79 (1977) 544–552. https://doi.org/10.1016/0003-2697(77)90428-6.
[115] L.-A. McCarthy, A. Dye, E. Ferrari, Absolute Quantification of Gold Nanoparticles with Femtomolar Accuracy Using Inductively Coupled Plasma Atomic Emission Spectroscopy, in: 2020: pp. 283–288. https://doi.org/10.1007/978-1-0716-0319-2_21.
[116] H. Wang, T. Zhang, X. Zhou, Dark-field spectroscopy: development, applications and perspectives in single nanoparticle catalysis, J. Phys. Condens. Matter. 31 (2019) 473001. https://doi.org/10.1088/1361-648X/ab330a.
[117] Y. Wang, D. Li, W. Ren, Z. Liu, S. Dong, E. Wang, Ultrasensitive colorimetric detection of protein by aptamer–Au nanoparticles conjugates based on a dot-blot assay, Chem. Commun. (2008) 2520. https://doi.org/10.1039/b801055b.
[118] Pedro Miguel Pinto Gonçalves Gouveia Pedrosa, Gold Nanoparticles to Tackle Drug Resistance in Cancer, Universidade Nova de Lisboa, 2019. http://hdl.handle.net/10362/91106.
[119] T.L. Riss, R.A. Moravec, A.L. Niles, S. Duellman, H.A. Benink, T.J. Worzella, L. Minor, Cell Viability Assays, Eli Lilly & Company and the National Center for Advancing Translational Sciences, 2004. https://www.ncbi.nlm.nih.gov/books/NBK144065/.
[120] W. Strober, Trypan Blue Exclusion Test of Cell Viability, Curr. Protoc. Immunol. 111 (2015). https://doi.org/10.1002/0471142735.ima03bs111.
[121] J.-W. Park, J.S. Shumaker-Parry, Structural Study of Citrate Layers on Gold Nanoparticles: Role of Intermolecular Interactions in Stabilizing Nanoparticles, J. Am. Chem. Soc. 136 (2014) 1907–1921. https://doi.org/10.1021/ja4097384.
[122] J. Turkevich, P.C. Stevenson, J. Hillier, A study of the nucleation and growth processes in the

synthesis of colloidal gold, Discuss. Faraday Soc. 11 (1951) 55. https://doi.org/10.1039/df9511100055.
[123] R.H.A. Pereira, W.J. Keijok, A.R. Prado, J.P. de Oliveira, M.C.C. Guimarães, Rapid and sensitive detection of ochratoxin A using antibody-conjugated gold nanoparticles based on Localized Surface Plasmon Resonance, Toxicon. 199 (2021) 139–144. https://doi.org/10.1016/j.toxicon.2021.06.012.
[124] J.N. ANKER, W.P. HALL, O. LYANDRES, N.C. SHAH, J. ZHAO, R.P. VAN DUYNE, Biosensing with plasmonic nanosensors, in: Nanosci. Technol., Co-Published with Macmillan Publishers Ltd, UK, 2009: pp. 308–319. https://doi.org/10.1142/9789814287005_0032.
[125] P. Jara-Guajardo, P. Cabrera, F. Celis, M. Soler, I. Berlanga, N. Parra-Muñoz, G. Acosta, F. Albericio, F. Guzman, M. Campos, A. Alvarez, F. Morales-Zavala, M.J. Kogan, Gold Nanoparticles Mediate Improved Detection of β-amyloid Aggregates by Fluorescence, Nanomaterials. 10 (2020) 690. https://doi.org/10.3390/nano10040690.
[126] P. Sciau, Transmission Electron Microscopy, in: 2016: pp. 43–67. https://doi.org/10.1016/bs.aiep.2016.09.002.
[127] A.I. Dolinnyi, Extinction coefficients of gold nanoparticles and their dimers. Dependence of optical factor on particle size, Colloid J. 79 (2017) 611–620. https://doi.org/10.1134/S1061933X17050052.
[128] E. Dmitrienko, O. Naumova, B. Fomin, M. Kupryushkin, A. Volkova, N. Amirkhanov, D. Semenov, I. Pyshnaya, D. Pyshnyi, Surface modification of SOI-FET sensors for label-free and specific detection of short RNA analyte, Nanomedicine. 11 (2016) 2073–2082. https://doi.org/10.2217/nnm-2016-0071.
[129] V.D. Pham, H. Hoang, T.H. Phan, U. Conrad, H.H. Chu, Production of antibody labeled gold nanoparticles for influenza virus H5N1 diagnosis kit development, Adv. Nat. Sci. Nanosci. Nanotechnol. 3 (2012) 045017. https://doi.org/10.1088/2043-6262/3/4/045017.
[130] H. Safarpour, H. Majdi, A. Masjedi, A.S. Pagheh, M. de L. Pereira, S.M. Rodrigues Oliveira, E. Ahmadpour, Development of Optical Biosensor Using Protein A-Conjugated Chitosan–Gold Nanoparticles for Diagnosis of Cystic Echinococcosis, Biosensors. 11 (2021) 134. https://doi.org/10.3390/bios11050134.
[131] H. Safarpour, M. Pourhassan-Moghaddam, A. Spotin, H. Majdi, A. Barac, M. Yousefi, E. Ahmadpour, A novel enhanced dot blot immunoassay using colorimetric biosensor for detection of Toxoplasma gondii infection, Comp. Immunol. Microbiol. Infect. Dis. 79 (2021) 101708. https://doi.org/10.1016/j.cimid.2021.101708.
[132] D. Lee, J.H. Hong, Nanoparticle-Mediated Therapeutic Application for Modulation of Lysosomal Ion Channels and Functions, Pharmaceutics. 12 (2020) 217. https://doi.org/10.3390/pharmaceutics12030217.
[133] B. Kepsutlu, V. Wycisk, K. Achazi, S. Kapishnikov, A.J. Pérez-Berná, P. Guttmann, A. Cossmer, E. Pereiro, H. Ewers, M. Ballauff, G. Schneider, J.G. McNally, Cells Undergo Major Changes in the Quantity of Cytoplasmic Organelles after Uptake of Gold Nanoparticles with Biologically Relevant Surface Coatings, ACS Nano. 14 (2020) 2248–2264. https://doi.org/10.1021/acsnano.9b09264.
[134] K. Vermeulen, D.R. Van Bockstaele, Z.N. Berneman, The cell cycle: A review of regulation, deregulation and therapeutic targets in cancer, Cell Prolif. 36 (2003) 131–149. https://doi.org/10.1046/j.1365-2184.2003.00266.x.
[135] R. Bansal, S. Rakshit, W. Han, S. Kumar, Modulation of Apoptosis Pathways in the Biology and Treatment of Multiple Myeloma, Oncol. Haematol. 17 (2021) 48. https://doi.org/10.17925/OHR.2021.17.1.48.
[136] M.S. Hossain, H. Karuniawati, A.A. Jairoun, Z. Urbi, D.J. Ooi, A. John, Y.C. Lim, K.M.K. Kibria, A.K.M. Mohiuddin, L.C. Ming, K.W. Goh, M.A. Hadi, Colorectal Cancer: A Review of Carcinogenesis, Global Epidemiology, Current Challenges, Risk Factors, Preventive and Treatment Strategies, Cancers (Basel). 14 (2022) 1732. https://doi.org/10.3390/cancers14071732.
[137] R. Augustine, A. Hasan, R. Primavera, R.J. Wilson, A.S. Thakor, B.D. Kevadiya, Cellular uptake and retention of nanoparticles: Insights on particle properties and interaction with cellular components, Mater. Today Commun. 25 (2020) 101692. https://doi.org/10.1016/j.mtcomm.2020.101692.

A

APPENDIX

A.1 Figures and tables

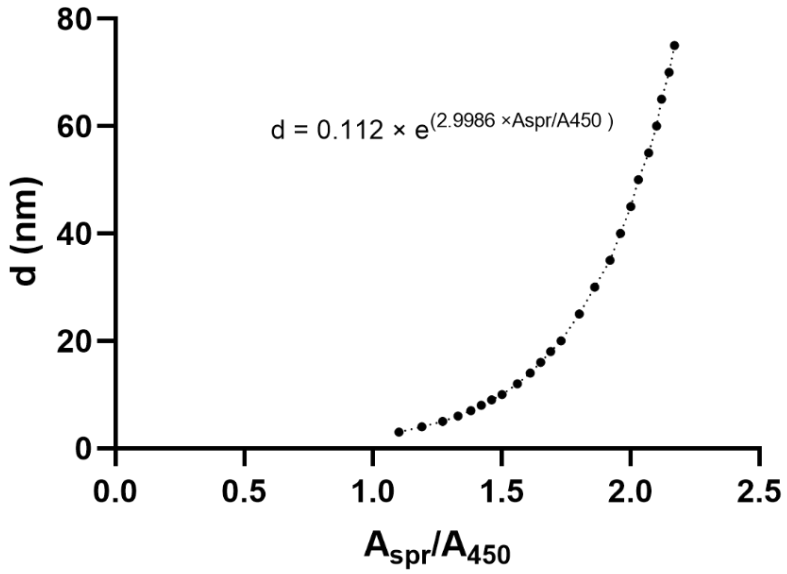

Figure 4.1 Dependence of the spheric gold nanoparticle diameter (d) by the ratio between their absorbance at the SPR peak (A_{SPR}) and the absorbance at 450 nm (A_{450}) determined by Wolfgang Haiss et al.

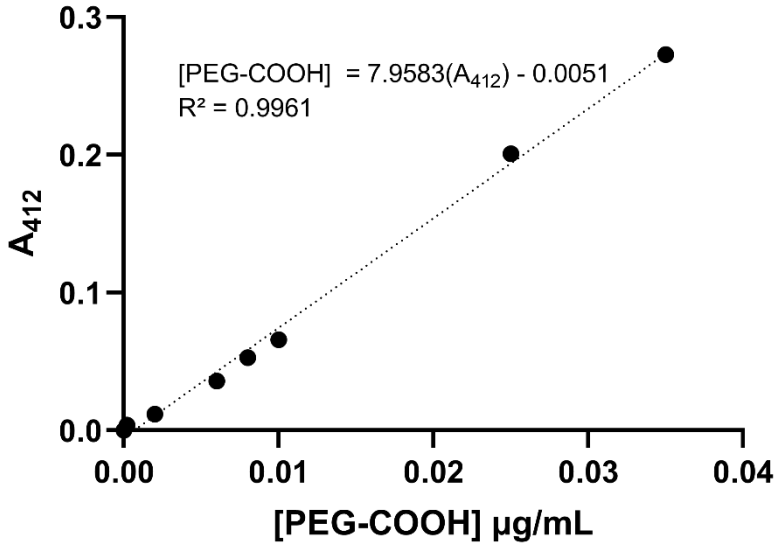

Figure 4.2 Ellman's assay calibration curve. The calibration curve was performed by measuring the absorbance at 412 nm (A_{412}) of HS-PEG(8)-COOH solutions with known concentrations (0.00 – 0.035 µg/mL).

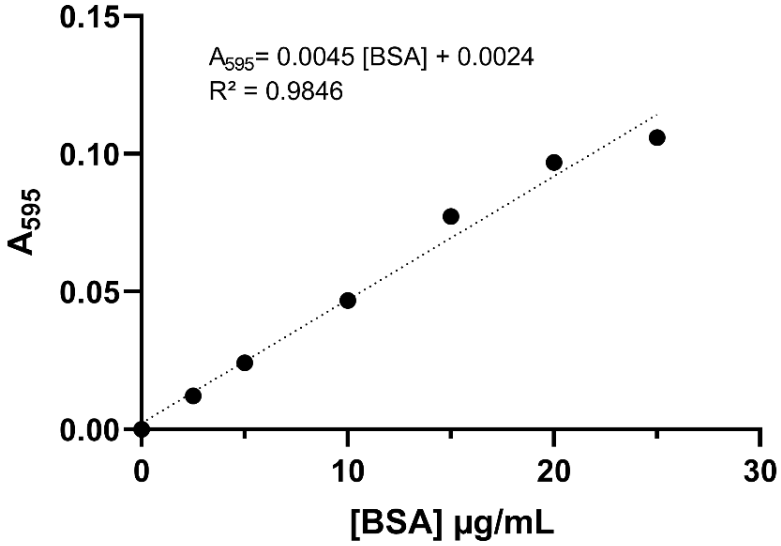

Figure 4.3 Bradford assay calibration curve. The calibration curve was performed by measuring the absorbance at 495 nm (A_{495}) of BSA solutions with known concentrations (0.0 – 25.0 µg/mL).

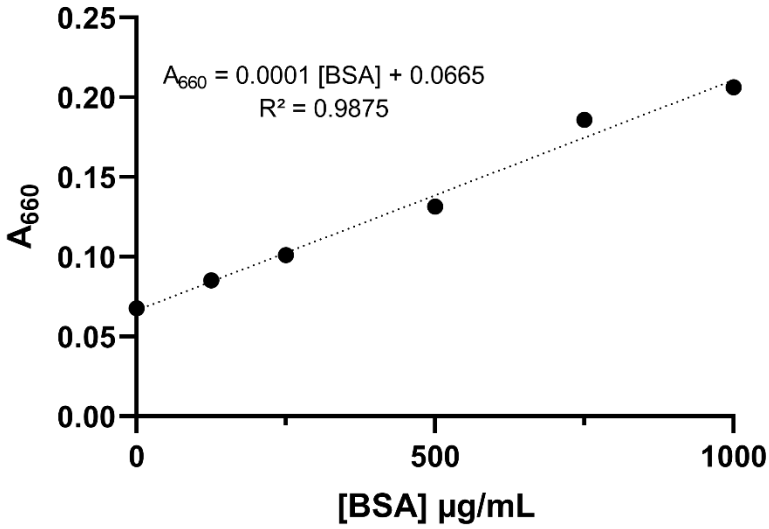

Figure 4.4 Pierce assay calibration curve. The calibration curve was performed by measuring the absorbance at 660 nm (A_{660}) of BSA solutions with known concentrations (0.0 – 100.0 µg/mL).

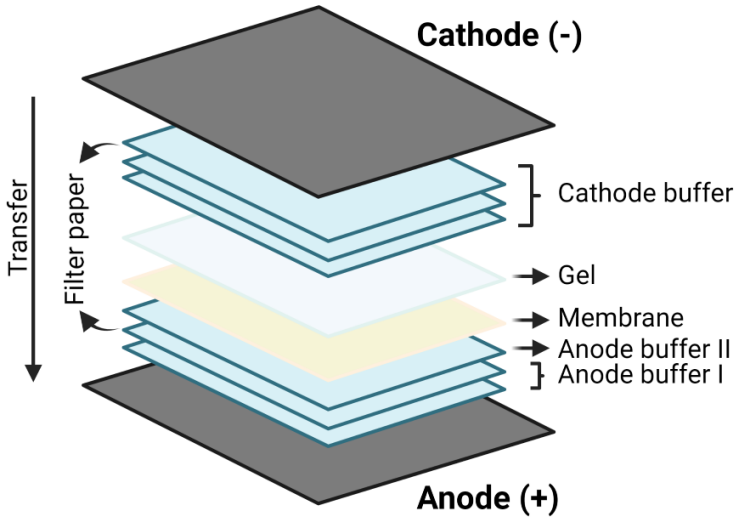

Figure 4.5 Schematic representation of the semi-dry transfer system.

Table 4.1 Buffers composition used to wet the filter papers used in the semi-dry transfer system.

Buffer	Composition
Cathode	25 mM Tris, 40 mM 6-amino-n-caproic-acid, pH 9.4
Anode I	0.3 M Tris, pH 10.4
Anode II	25 mM Tris pH 10.4

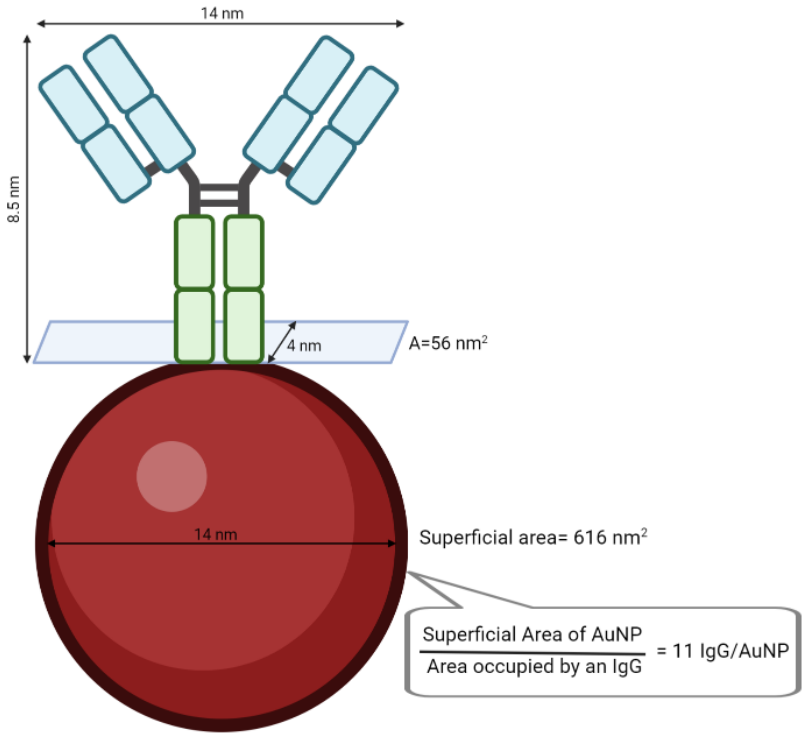

Figure 4.6 Schematic representations of the calculations performed to estimate how many antibodies (IgG) could be functionalized on the surface of a 14 nm spheric gold nanoparticle. Assuming the antibody orientation showed in this figure, the area occupied by an IgG were represented by the blue rectangle (4 x 14 nm). The number of antibodies were calculated dividing the superficial area of a 14 nm spheric gold nanoparticle by the area occupied by an IgG.